2018

Design and Development of Noble Metal Based Porous Materials as Electrocatalysts

Kyubin Shim
University of Wollongong

UNIVERSITY
OF WOLLONGONG
AUSTRALIA

Design and Development of Noble Metal Based Porous Materials as Electrocatalysts

A thesis submitted for fulfilment of the requirements for the award of the degree of

DOCTOR of PHILOSOPHY

From

The

UNIVERSITY OF WOLLONGONG

By

Kyubin Shim

Institute for Superconducting and Electronic Materials

University of Wollongong, NSW, Australia

8th Octorber, 2018

Certificate of Originality

I, Kyubin Shim, declare that this thesis is submitted in fulfilment of the requirements for the award of Doctor of Philosophy, in the Institute for Superconducting and Electronic Materials, University of Wollongong, NSW, Australia. This thesis is entirely my own work unless otherwise referenced or acknowledged. All experimental data in this paper are original. This thesis has not been submitted to other academic institutions.

Kyubin Shim

8th Octorber 2018

Dedication

To my family and friends

Acknowledgements

It is a pleasure to express my sincere thanks to my supervisors, Dr. Md Shahriar Hossain, Prof. Jung Ho Kim, and Prof. Yusuke Yamauchi, who provided me with the opportunity to work with them. In particular, I would like to thank Prof. Jung Ho Kim. His professional supervision and guidance, continuous support, great encouragement, and correction of my manuscripts, have helped me to complete this thesis.

I would like to thank Prof. Yoon-Uk Heo (Pohang University of Science and Technology), Prof. Mohammed Shahabuddin (King Saud University), Prof. Min-Sik Park (Kyung Hee University), and Prof. Kevin C.-W. Wu (National Health Research Institutes), who have been helpful with various types of advice and support.

I am grateful to my co-workers, Dr. Jeonghun Kim (The University of Queensland), Mr. Won-Chul Lee (Pusan National University), Dr. Sanga Han (University of Wollongong), Mr. Jaewoo Lee (University of Wollongong), Dr. Zhong-Li Wang (National Institute for Materials Science), and Dr. Bo Jiang (National Institute for Materials Science), who have been very helpful, sharing their experience, knowledge, and suggestions during my PhD study.

Technical assistance and instruction from the staff at UOW, particularly those at the Australian Institute of Innovative Materials (AIIM), such as Dr. Germanas Peleckis, Xun Xu (XRD), Dr. Dongqi Shi (XPS), Dr. Tony Romeo (FESEM), Mr. Tony Romeo and Dr Mitchell Nancarrow (FESEM), Dr. Kosta Konstantinov (TGA, BET), and Dr. David Mitchell and Dr. Gilberto Casillas Garcia (TEM) are greatly appreciated. Other staff members, including Mrs. Joanne George, Mrs. Crystal Mahfouz, Mrs. Narelle Badger, Dr. Tania Silver (English editing) and Mrs. Candace

Gabelish, are very much appreciated for their administrative and safety education assistance.

I also would like to thank my colleagues and friends, including Dr. Jong Won Chung, Prof. Hyun Kyoung Yang, Dr. Joo Hyun Lee, Mr. Jong-Min Moon, Dr. Dong-Min Kim, Mr. Ju Hyun Oh, Mr. Ji Seung Ryu, Mr. Jung Sik Ju, Dr. Jin Young Park, Dr. Dong Yoo Kim, who have been very helpful, sharing their experience, knowledge and suggestions. I am also grateful to Dr. Jang-Hee Yoon, Prof. Sung Kyun Park, Prof. Byung-Chun Choi, and Prof. Seyong Choi. They have also provided practical help for my life in Australia.

Finally, I would like to thank my parents and my sister for their love and support.

Abstract

Electrocatalysts are in the spotlight due to their various applications, including energy storage and sensors. Among them, electrocatalysts used as sensor electrodes are very important because they are relevant to human health. Many studies have been made to increase the efficiency of the electrocatalysts *via* the development of new catalytic materials. Among the various materials, noble metal-based materials are considered important because of their good catalytic properties, although they have the disadvantage that they are expensive compared to common materials. Therefore, various methods, such as changing their morphology, increasing their surface area, and size control, have been employed to overcome this drawback. This thesis introduces the synthesis of noble-metal-based electrode materials and their applications.

Dendritic platinum nanoparticles (DPNs) have been synthesized using an amphiphilic non-ionic surfactant (Brij 58®) via a sonochemical method. The particle size of the DPNs can be tuned by changing the reduction temperature, which resulted in a uniform DPN with a size of 23 nm or 60 nm. The facets of DPNs were observed by high-resolution transmission electron microscopy (TEM). In addition, the cytotoxicity of DPNs was investigated for biosensor applications using human embryonic kidney cells (HEK-293).

A sensor was prepared for bisphenol A (BPA) detection. As-prepared DPNs with a high surface area were coated on gold nanoparticles deposited on a screen-printed carbon electrode. In addition, a polyethyleneimine-phosphatidylcholine (PEI-PC) layer was deposited on the DPN modified electrode to improve its sensitivity and selectivity. The sensor performance in BPA detection was demonstrated using amperometry to reveal two wide dynamic ranges of 0.01-1.0 μM and 1.0 μM-300 μM, respectively. The detection

limit (DL) for BPA was determined to be 6.63 ± 0.77 nM. To investigate the reliability of this sensor, we evaluated the sensor for BPA detection in tap water through recovery studies for practical applications.

Porous Au@Pt nanoparticles (NPs) were synthesized *via* the sonochemical method with different molar ratios (Pt/Au: 3:7, 5:5, and 7:3). A TEM study showed that the Au was located in the core, while Pt was located on the core (as a shell). The Pt/Au sample with a molar ratio of 3:7 (Pt/Au) had a higher electrochemically active surface area than the other samples (5:5 and 7:3). The Au@Pt (7:3) modified electrodes revealed best performance towards glucose oxidation compared to the other modified electrodes. The Au@Pt (7:3) modified electrodes possessed two dynamic ranges for glucose oxidation, 0.5 – 50 μM and 0.05 – 10.0 mM, with the detection limit of 319.8 nM in 0.1 M phosphate buffer solution (PBS).

To enhance glucose detection, Au decorated Au@Pt NPs were prepared by sonochemical and electrodeposition methods. The electrochemically active surface area (ECSA) of Au@Pt/Au was increased compared to the NPs before Au deposition. Nafion layers were employed to avoid interference effects. Using the final electrodes, the extent of glucose oxidation was determined in 0.1 M phosphate buffered saline (PBS_{sal}) (pH 7.4). The electrode featured two dynamic ranges for glucose (0.5 – 10.0 μM and 0.01 – 10.0 mM) with the detection limit of 445.7 nM. To investigate the reliability of the sensor probe, it was applied to detect glucose levels in human whole blood samples.

Porous bimetallic Pd@Pt NPs prepared using two different surfactants (Brij® 58 (Brij 58) and Pluronic® F-127 (F-127)) were synthesized to compare the effects of different surfactants. To compare Pd@Pt NPs prepared using F-127 and Brij 58, TEM and ECSA were have employed. The TEM study indicated that Brij 58 resulted in a denser material

than F-127. In addition, the ECSA of the Pd@Pt NPs with F-127 was higher than with Brij 58. It was revealed that F-127 produced more electrochemically active sites, which resulted in better sensitivity towards bisphenol A detection.

A Pd/N-doped carbon nanofiber (Pd/N-C) hybrid was synthesized *via* electropolymerization and reduction methods. 1.5 wt % of small sized Pd nanoparticles was loaded on the carbon nanofibers. The Pd/N-C hybrid showed similar sensitivity compared to commercial Pd/C (10 wt %), even though the Pd loading amount was only 1.5 wt % for bisphenol A detection. The material featured two dynamic ranges from 0.1 to 10 µM and 10 to 200 µM with the detection limit of 29.44 nM.

Table of Contents

Title Page

Certificate of Originality 2

Dedication 3

Acknowledgements 4

Abstract 6

Table of Contents 9

List of Figures 12

List of Tables 19

List of Schemes 20

List of Abbreviations 21

1. Introduction 23

1.1 General background 23

1.2 Motivation of the research 25

1.3 Thesis results 26

1.4 References 29

2. Literature review 30

2.1 Porous catalytic materials 30

2.2 Synthesis method for porous noble metal based materials 32

2.2.1 Hard templates 33

2.2.2 Soft templates 35

2.3 Noble metal based porous materials 39

2.3.1 Porous noble metal materials 40

2.3.2 Porous noble bimetallic materials and carbon composites decorated with metal nanoparticles 42

2.4 Electrocatalytic reactions 45

2.4.1 Glucose 46

2.4.2 Phenolic compounds 49

2.4.3 Biologically important organics (Dopamine, uric acid, and ascorbic acid) 52

2.5 References 54

3. Experimental 64

3.1 Overview 64

3.2 Materials and chemicals 64
3.3 Materials preparation 66
3.4 Physical and morphological characterization techniques 66
3.4.1 X-ray powder diffraction (XRD) 66
3.4.2 Brunauer-Emmett-Teller (BET) Analysis 67
3.4.3 X-Ray Photoelectron Spectroscopy (XPS) 67
3.4.4 Scanning electron microscopy (SEM) 67
3.4.5 Transmission electron microscopy (TEM) 68
3.5 Electrochemical characterizations techniques 68
3.5.1 Cyclic voltammetry 68
3.5.2 Amperometry 68
4. Synthesis and cytotoxicity of dendritic platinum nanoparticles with HEK-293 cells 70
4.1 Introduction 70
4.2 Experimentals 72
4.3 Results and discussions 73
4.4 Conclusions 81
4.5 References 83
5. Efficient electrochemical bisphenol-A oxidation by self-supported dendritic platinum nanoparticles on screen-printed carbon electrode 87
5.1 Introduction 87
5.2 Experimental 89
5.3 Results and discussion 92
5.4 Conclusions 105
5.5 References 106
6. Rationally designed bimetallic Au@Pt nanoparticles for glucose oxidation 110
6.1 Introduction 110
6.2 Experimental 112
6.3 Results and discussions 113
6.4 Conclusions 121
6.5 References 123
7. Au decorated core-shell structured Au@Pt for the glucose oxidation reaction 126

7.1 Introduction 126
7.2 Experimental 129
7.3 Results and discussion 131
7.4 Conclusions 149
7.5 References 150
8. Tunable porosity in bimetallic core-shell structured Palladium-Platinum nanoparticles for electrocatalysts 154
8.1 Introduction 154
8.2 Experimental 155
8.3 Results and discussion 157
8.4 Conclusions 163
8.5 References 165
9. Facile synthesis of palladium-nanoparticle-embedded N-doped carbon fibers for electrochemical sensing 168
9.1 Introduction 168
9.2 Experimental 170
9.3 Results and discussions 172
9.4 Conclusions 180
9.5 References 181
10. Conclusions and outlook 185
10.1 Conclusions 185
10.2 Outlooks 187
Appendix A: List of Publications 189
Appendix B: Conferences 191

List of Figures

Figure 2.1. Classification of porous materials depending on their pore size [4].
*Nanoporous materials: Pore diameter is nanosized materials.

Figure 2.2. The general processes for the hard- and soft- template synthesis methods.

Figure 2.3. (a) Schematic illustration of a synthetic procedure for mesoporous Pt nanoparticles (MPNs). (b, c) SEM images of mesoporous platinum nanoparticlesobtained by using SBA-15 templates [24].

Figure 2.4. Self-organization structures of amphiphilic molecules [28].

Figure 2.5. (a) Systematic illustration of synthesis of mesoporous bi- (PdPt) and tri- (Au@PdPt and PdPtCu) metallic nanoparticles using F-127 [33], (b) Systematic illustration of the synthesis of NMCS using PS-b-PEO [34].

Figure 2.6. (a) Illustration of the macroscopic enantiomeric helical morphologies and corresponding opposite DNA chiral packing of impeller-like helical DNA-silica complexes (IHDSCs) (b) SEM images of the DSCs [38]. (c) Structural characterization of a carbon nanotube (CNT)-butterfly wing composite [40].

Figure 2.7. TEM images of (a) Pt [27] and (b) Pd [53] porous architectures. SEM images of (c) Ag [52] and (d) Au [50] porous architectures.

Figure 2.8. Structures of bimetallic nanoparticles: (a) mixed alloys; (b) random alloys; (c) subclusters with two interfaces (d) subclusters with three interfaces; (e) subclusters with small number of A–B bonds; (f) core–shell nanoparticles; (g) multishell core–shell nanoparticles; (h) multiple small core material coated in a single shell material, (i) movable core within hollow shell material [53].

Figure 2.9. TEM images of various Pt-based bimetallic porous materials: (a) nanoporous PtCo alloy nanowires [54], (b) PdPt nanodendrites [55], (c) TEM and EDS mapping images of PtPd alloy nanotubes, (d) TEM and EDS mapping images of PtAg alloy nanotubes, and (e) TEM and EDS mapping images of PtPdAg alloy nanotubes [56].

Figure 2.10. (a) TEM image of Pt@NHPCP (b-e) Elemental mapping results for Pt@NHPCP: (b) Carbon, (c) Nitrogen, (d) Oxygen, (e) Platinum [61]. (f) TEM image of PtCo/Co@NHPCC (g-j) Elemental mapping results for PtCo/Co@NHPCC: (g) Carbon, (h) Nitrogen, (i) Platinum, (j) Cobalt [62].

Figure 2.11. Sensing principles of the enzymatic glucose sensor (a) Schematic illustrations showing the GOx-based glucose sensors. (b) Schematic illustrations showing the sensing mechanism of FAD/PQQ-GDH (left) and NAD(P)-GDH (right) glucose sensor [78]. (c) sensing principles of the non-enzymatic glucose sensors [75].

Figure 2.12. SEM image of mesoporous Au film (MpGF): (a) high- and (b) low-magnification, and (c) cross-section, (d) Plot of the amperometric current response to the concentration of glucose. [79]. TEM images of AuPt nanodendrites: (e) low- and (f) high-magnification; SEM images of mesoporous AuPt nanodendrites: (g) low- and (h) high-magnification; (i) the calibration plot for glucose detection using Au/Pt nanodendrite modified electrode [80].

Figure 2.13. (a) SEM image of AuNPs/MoS_2. (b) Relationship between the peak current and the concentration of BPA (Inset: Cyclic voltammograms of BPA AuNPs/MoS_2/GCE in 0.1 M PBS (pH 7.0)) [96]. (c) SEM image of RGO/CNT/AuNPs. (d) DPV peak currents for BPA detection in two linear ranges of 1.45 to 20 nM and 20 to 1,490 nM (Inset: expanded view of measurements of 1.45 to 20 nM of BPA) [97]. GCE: glassy carbon electrode; DPV: differential pulsed voltammetry.

Figure 2.14. (a) TEM images of AgPt/pCNFs and the corresponding elemental mapping. (b) DPV curves of different concentrations of DA (10, 30, 50, 100, 250, 500 μM) on AgPt/pCNFs/GCE [107]. (c) TEM image of Pd@Au/RGO nanocomposite with corresponding elemental mapping (d) DPV curves of Pd@Au/RGO/GCE containing different concentrations of AA from 50 to 2856.63 μM, DA from 1 to 400.56 μM, and UA from 5 to 680.76 μM [108].

Figure 4.1. (a) Schematic illustration of the synthesis of DPNs. (b) Photographs of the color change during synthesis (room temperature (20 ℃), 60 ℃). (c) UV/Vis spectra before reaction (red), after reaction (blue) and after centrifuge (upper solution). Inset: the Tyndall effect on DPN suspension in solution.

Figure 4.2. TEM images of DPNs obtained at 20 ℃ (a–c) and 60 ℃ (e–g): Corresponding SAED (inset of (a)) and FFT pattern (inset of (c)). (d, h) The particle and arm size distributions of DPNs obtained at different temperatures (20 ℃ (d) and 60 ℃ (h))

Figure 4.3. Characterization of DPNs: (a) wide-angle XRD, (b) low-angle XRD, and (c) N2 adsorption-desorption isotherm; inset: pore size distribution by the Barrett-Joyner-Halenda (BJH) method.

Figure 4.4. TEM images of DPNs obtained at room temperature (20℃).

Figure 4.5. (a, b) TEM images of DPNs obtained at room temperature (20℃) with stirring. (c) The particle size distribution. (d) The arm size distribution.

Figure 4.6. (a, b) TEM images of DPNs obtained at 60 ℃ with stirring. (c) The particle size distribution. (d) The arm size distribution.

Figure 4.7. HAADF-STEM study of DPNs: (a) high magnification image in [110] beam direction, (b) low magnification image under off-axis conditions, (c) FFT pattern of (a). (d, e) FFT patterns at positions 1 and 2 of (b). (f) Structure of single crystal Pt nanoparticle.

{111} and {100} facets were still observed under off axis conditions, which implied that both planes were facet planes.

Figure 4.8. (a) Images of cells in culture at different concentrations of DPNs. (b) Images of cells in culture at 0 h and 48 h without Pt nanoparticles. Blank culture with no nanoparticles added subjected to trypan blue staining method showed 95.55% viability. (c) Cell viability test of DPNs from HEK-293 cells according to different concentrations.

Figure 5.1. Photograph and schematic illustration of PEI-PC/DPNs/AuNPs electrode. (b) Chemical structures of polyethyleneimine (PEI) and phosphatidylcholine (PC). (c) Bisphenol A oxidation.

Figure 5.2. TEM image of prepared DPNs (inset: SAED pattern). (b) Wide-angle XRD pattern of DPN. (c) HAADF-STEM image of DPNs (inset: FFT pattern). (d) SEM image of DPNs/AuNPs on electrode (schematically illustrated in inset).

Figure 5.3. Cyclic voltammograms (CVs) for characterization of DPNs and Pt Black on the AuNPs modified electrodes. (a) Determination of electrochemical active surface area (ECSA) of DPNs and Pt Black. (b) Detection of various concentrations (10, 25, 50, and 100 μM) of bisphenol A using Pt Black electrode. (c) Detection of various concentrations (10, 25, 50, and 100 μM) of bisphenol A using DPNs electrode. (d) Bisphenol A detection calibration curves (DPNs and Pt black), with insets showing DPN and Pt Black particles.

Figure 5.4. XPS analysis of surface of DPNs electrode: (a) before BPA oxidation, (b) after BPA oxidation.

Figure 5.5. Redox currents of electrodes in (a) 4 mM $Ru(NH_3)_6Cl_3$ and (b) 4 mM $K_3[Fe(CN)_6]$ from cyclic voltammetry.

Figure 5.6. (a) SEM image of DPNs/AuNPs/SPCE. (b) XPS survey spectrum of DPNs/AuNPs/SPCE. (c) SEM image of PEI-PC/DPNs/AuNPs/SPCE. (d) XPS survey spectrum of PEI-PC/DPNs/AuNPs/SPCE.

Figure 5.7. (a) The chemical structure of interaction of between BPA and PC at minimized energy. (b) Photographs of water contact angles of various layers (DPNs, PEI/DPNs, and PEI-PC/DPNs). (c) Contact angles of various layers (DPNs, PEI/DPNs, and PEI-PC/DPNs).

Figure 5.8. Optimization of experimental parameters in terms of (a) deposited amount (DPNs), (b) PEI concentration, and (c) PC concentration.

Figure 5.9. Amperograms of the addition of 50 μM BPA and 100 μM of other interfering species in various electrodes (i: ascorbic acid, ii: acetaminophen, iii: uric acid, and iv: dopamine).

Figure 5.10. (a) Amperometric response of PEI-PC/DPNs/AuNPs modified SPCE according to different concentrations of BPA. (b) Calibration curves from the

amperometric responses at two ranges of BPA concentration: of (i) 0.01–1 μM and (ii) 1–300 μM.

Figure 6.1. Illustrations of synthesis of Au@Pt nanoparticles with three different Au:Pt ratios (a) 3:7, (b) 5:5, and (c) 7:3 (left), and photographs of the Tyndall effect on Au@Pt suspensions in solution (right).

Figure 6.2. (a-c) TEM images of Au@Pt NPs with three different Au:Pt ratios (a) 3:7, (b) 5:5, and (c) 7:3, with the insets showing the corresponding SAED patterns. (d) Wide-angle XRD patterns of Au@Pt NPs with three different ratios (3:7, 5:5, 7:3).

Figure 6.3. TEM images of different ration of Au@Pt NPs (a) 3:7, (b) 5:5, and (c) 7:3.

Figure 6.4. Particles size distribution analysis of Au@Pt NPs with three different Au:Pt Ratios (3:7 (blue, dash-dot-dot), 5:5 (red, dash), and 7:3 (green, solid)) by dynamic light scattering (DLS).

Figure 6.5. SEM images of Au@Pt NPs with three different Au:Pt ratios (a) 3:7, (b) 5:5, and (c) 7:3.

Figure 6.6. High-angle annular dark-field scanning transmission electron microscope (HAADF-STEM) images, corresponding elemental mappings, and line scans of Au@Pt NPs with different molar ratios: (a) 3:7, (b) 5:5, and (c) 7:3.

Figure 6.7. CVs and ECSAs for the three different ratios (3:7, 5:5, 7:3) of Au@Pt NPs. (a) CVs in 0.5 M H_2SO_4 (scan rate:100 mV s^{-1}), (b) ECSA from adsorption of H atoms, (c) ECSA from anodic peaks of Au.

Figure 6.8. LSVs recorded for the electrodes: AuNPs/SPCE (dash line), PtNPs/AuNPs/SPCE (short dotted line), and Au@Pt/AuNPs/SPCE (solid line) in (a) 0.1 M KOH (pH 13) and (b) 0.1 M PBS (pH 7.4) containing 10 mM glucose, respectively.

Figure 6.9. Optimization of Au@Pt NPs: (a) loading amount and (b) applied potential.

Figure 6.10. CVs of Au@Pt NPs with three different Au:Pt ratios (3:7, 5:5, 7:3): (a) adsorption of H atoms and (b) anodic peaks of Au.

Figure 6.11. (a) CVs for Au@Pt NPs with three different Au:Pt ratios (3:7, 5:5, 7:3) recorded in 0.1 M PBS (pH 7.4) containing 10 mM glucose at a scan rate of 100 mV s^{-1}.(b) Calibration plots of modified electrodes: Au@Pt (3:7) (black line), Au@Pt (5:5) (red line), and Au@Pt (7:3) (blue line). (c) Amperometric response of Au@Pt (7:3) modified electrode to a wide range of glucose concentrations in 0.1 M PBS (pH 7.4), and (d) calibration plot of Au@Pt (7:3) modified electrode (applied potential: + 0.10 V (Ag/AgCl)).

Figure 7.1. CVs recorded for Au@Pt/Au NPs modified AuNPs/SPCE in 0.5 M H_2SO_4 solution.

Figure 7.2. CVs recorded for bimetallic Au@Pt nanoparticle modified electrode in 0.1 M PBS (pH 7.4) solution containing 10 mM glucose, with Au:Pt ratios of (i) 3:7, (ii) 5:5, and (iii) 7:3.

Figure 7.3. Morphologies of Au@Pt and Au@Pt/Au NPs: (a),(b) TEM images of Au@Pt (inset in (a): corresponding SAED pattern); (c) schematic illustration of Au@Pt NPs; (d),(e) TEM images of Au@Pt/Au (inset in (d): corresponding SAED pattern); (f) schematic illustration of Au@Pt/Au NPs.

Figure 7.4. (a) High-angle annular dark-field scanning transmission electron microscope (HAADF-STEM) image, corresponding elemental mapping, and line scans of Au@Pt NPs, (b) HAADF-STEM image, elemental mapping, and line scans of Au@Pt/Au NPs.

Figure 7.5. High-angle annular dark-field scanning transmission electron microscope (HAADF-STEM) image with corresponding elemental mapping of Au@Pt/Au NPs.

Figure 7.6. Wide-angle XRD spectra of the (i) Pt, (ii) Au@Pt, and (iii) Au@Pt/Au NPs.

Figure 7.7. (A) CVs of the Pt (dotted line), Au@Pt (dashed line), and Au@Pt/Au NPs (solid line), and (B) ECSAs of Au@Pt and Au@Pt/Au in 0.5 M H_2SO_4 (scan rate:100 mV s^{-1}).

Figure 7.8. Frequency changes during the electrodeposition of Au solution on an Au@Pt modified electrode.

Figure 7.9. CVs obtained in solutions containing (a) 4.0 mM $[Fe(CN)_6]^{3-}$ and (b) 4.0 mM $[Ru(NH_3)_6]Cl_3$ using bare SPCE (black dashed line), Au@Pt/AuNPs/ SPCE (red dotted line), Au@Pt/Au/AuNPs/SPCE (blue dash-dotted line), and Nafion/Au@Pt/Au/AuNPs/SPCE (green solid line).

Figure 7.10. CVs recoded for (a) Au@Pt/Au/AuNPs/SPCE (dash dotted dotted line) (blank), (b) AuNPs/SPCE (dash line), (c) Pt/AuNPs/SPCE (dotted line), (d) Au@Pt/AuNPs/SPCE (dash-dotted line), and (e) Au@Pt/Au/AuNPs/SPCE (solid line), where (a) without and (b-e) with 10 mM glucose in 0.1 M PBS (pH 7.4) at a scan rate of 100 mV s-1. Linear sweep voltammograms (LSVs) recorded for Au@Pt/Au/AuNP/SPCE in 0.1 M PBS (pH 7.4) containing 0.1 - 10.0 mM glucose.

Figure 7.11. (a) Amperometric responses to successive additions of glucose in 0.1 M PBS (pH 7.4) and (b) calibration plots of different kinds of modified electrodes: Pt (black line), Au@Pt (red line), and Au@Pt/Au (blue line). (c) Amperometric response to a wide range of glucose concentrations in 0.1 M PBS (pH 7.4), and (d) corresponding calibration plot of Au@Pt/Au modified electrode (applied potential: + 0.10 V (Ag/AgCl)).

Figure 7.12. Comparative calibration plots showing the effect of chloride ions on the Nafion/Au@Pt/Au/AuNPs/SPCE sensor, while the inset shows the amperometric response.

Figure 7.13. Surface of Au@Pt/Au modified electrodes: (a),(b) before Nafion coating and (c),(d) after Nafion coating.

Figure 7.14. Optimization of the experimental parameters: the effects of (a) amount of drop-coated Au@Pt solution, (b) applied potential, (c) temperature, and (d) pH, using a 0.1 M PBSsal (pH 7.4) solution containing 0.1 mM glucose to test the effects on the response peak current of Nafion/Au@Pt/Au/AuNPs/SPCE from the chronoamperometric experiments.

Figure 7.15. (a) Amperometric response to a wide range of glucose concentrations in 0.1 M PBS_{sal} (pH 7.4) and (b) corresponding calibration plot of Nafion/Au@Pt/Au modified electrode (applied potential: + 0.35 V (Ag/AgCl)). (c) Amperometric response for the interference effects of other bio-compounds on the sensor probe. (d) 27-day stability test, where the electrode was stored at room temperature in the dry state when not in use; test conditions: 0.1 M PBS_{sal} (pH 7.4) containing 1.0 mM glucose.

Figure 8.1. Illustrations of the synthesis of porous bimetallic Pd@Pt nanoparticles using two different surfactants: (a) Brij 58 (polyethylene glycol hexadecyl ether) and (b) F-127 (poly(ethyleneoxide)-poly(propylene oxide)-poly(ethylene oxide)).

Figure 8.2. The actual chemical formulae of two different surfactants ((a) Brij 58 and (b) F-127).

Figure 8.3. (a), (b) SEM images of Pd@Pt NPs prepared using Brij 58 (c), The particle size distributions of Pd@Pt NPs prepared using Brij 58 (d), (e) SEM images of Pd@Pt NPs prepared using F-127 (f) The particle size distributions of Pd@Pt NPs prepared using F-127.

Figure 8.4. (a,b) TEM images of Pd@Pt NPs prepared using Brij 58 and (c) the corresponding SAED pattern. (d,e) TEM images of Pd@Pt NPs prepared using F-127 and (f) the corresponding SAED pattern.

Figure 8.5. Wide-angle XRD patterns of porous bimetallic Pd@Pt NPs prepared using two different surfactants (Brij 58 and F-127).

Figure 8.6. High-angle annular dark-field scanning transmission electron microscope (HAADF-STEM) images and elemental mappings, with line scans (insets on far right panels), of porous bimetallic Pd@Pt nanoparticles prepared using two different surfactants: (a) Brij 58 and (b) F-127.

Figure 8.7. (a) Electrochemical active surface area(ECSA) of Pd@Pt NPs prepared using F-127 (blue solid) and Brij 58 (red dot) in 0.5M H_2SO_4 (scan rate: 0.05 V s^{-1}). (b) Bisphenol A detection calibration curves from CV (Pd@Pt NPs prepared using F-127 (blue solid) and Brij 58 (red dot)), (c)Amperometric response of Pd@PtNPs prepared using F-127 (blue solid) and Brij 58 (red dot) with different concentrations of BPA. (d)

Calibration curves from the amperometric of Pd@Pt NPs prepared using F-127 (blue solid) and Brij 58 (red dot) responses over two dynamic ranges of BPA concentration.

Figure 8.8. ECSA values for the Pd@Pt prepared using Brij 58 and F-127.

Figure 9.1. (a) Schematic illustration of the synthesis of Pd/N-C hybrid material and (b) SEM images of Pd/N-C hybrid material.

Figure 9.2. SEM image of Pd/C commercial material.

Figure 9.3. TEM images of Pd/N-C hybrid material: (a,b) low magnification, and (c,d) high magnification.

Figure 9.4. Raman spectrum of Pd/N-C hybrid material.

Figure 9.5. N_2 adsorption-desorption isotherm of Pd/N-C hybrid material.

Figure 9.6. Wide-angle XRD pattern of Pd/N-C hybrid material.

Figure 9.7. (a) HAADF-STEM image, and (b–d) elemental mapping images of Pd/N-C hybrid material.

Figure 9.8. XPS spectra of Pd/N-C hybrid material ((a) survey, (b) C 1s, (c) N 1s, and (d) Pd 3d, respectively).

Figure 9.9. Optimization of experimental parameter.

Figure 9.10. (a,b) CVs for characterization of Pd/N-C hybrid material (with 1.5 wt% Pd) and Pd/C commercial material (10 wt% Pd): (a) Detection of bisphenol A (50 μm) using Pd/N-C hybrid material and Pd/C commercial material electrodes. (b) Bisphenol A detection (5, 10, 50, and 100 μm) calibration curves. c) Amperometric response of Pd/N-C hybrid material/AuNPs/SPCE with different concentrations of BPA. d) Calibration curves from the amperometric responses over two ranges of BPA concentration.

Figure 9.11. Optimization of experimental parameters of Pd/N-C hybrid material. (a) Starting applied potential and (b) final applied potential.

List of Tables

Table 3.1. Description of chemicals and materials used in this doctoral work.

Table 4.1. The cell viability after incubation with Pt nanoparticles in comparison with other reports.

Table 5.1. Comparison of proposed sensors for detection of BPA by the electrochemical method (direct oxidation).

Table 5.2. Recovery of spiked BPA in tap water. RSD: relative standard deviation.

Table 6.1. Comparison of the performance of our Au@Pt NPs with previous reports.

Table 7.1. Comparison of the performances of our Au decorated Au@Pt NPs and of AuPt samples reported in other previous works.

Table 7.2. Comparison of the results obtained in the determination of the glucose concentration of whole blood samples by the proposed sensor and a comparable sensor system.

Table 8.1. Comparison studies of our BPA detection with previous literatures.

Table 9.1. Comparison of our performance with previous literature.

List of Schemes

Shceme 7.1. Schematic illustration of the synthesis of Au@Pt/Au NPs.

List of Abbreviations

TEM	Transmission electron microscopy
HRTEM	High-resolution transmission electron microscopy
XRD	X-ray diffraction
XPS	X-ray photoelectron spectroscopy
SEM	Scanning electron microscopy
CV	Cyclic voltammetry
CA	Chronoamperometry
DPV	Differential pulse voltammetry
EDS	Energy dispersive X-ray spectroscopy
BET	Brunauer Emmett Teller
a.u.	Arbitrary unit
cm	Centimeter
L	Liter
mL	Milliliter
μL	Microliter
M	Molar
mM	Millimolar
μM	Micromolar
nM	Nanomolar
V	Voltage
nm	Nanometer
BPA	Bisphenol A
DPN	Dendritic platinum nanoparticles
PEI	Polyethyleneimine

PC	Phosphatidylcholine
PBS	Phosphate buffer solution

1. Introduction

1.1 General background

Catalysis is a crucial field in applied science, which extends across many areas, such as chemistry, nanomaterial science, etc. Since it was first reported by J.J. Berzelius in 1835, catalysis has been well known as a phenomenon that makes chemical reactions take place faster when an additional non-reactant species (catalysts) is present [1]. In general, catalysts are classified into homogeneous and heterogeneous types. A homogeneous catalyst is composed of molecules dispersed in the same gas or liquid phase as the reactant molecules. In contrast, a heterogeneous catalyst is not in the same phase as the reactants, which are typically liquids or gases adsorbed onto the surface of the solid catalyst. Recently, the production of most industrially important chemicals has involved a catalytic reaction process. Most biochemically significant processes are also catalyzed by enzymes, which are extremely important in biology. In environmental science, typical catalytic converters in automobiles can protect the ozone layer. Catalytic reactions are also preferred in environmental green chemistry because of the reduced amount of waste generated. Among the various catalyst materials, many metals and metal complexes have been used in catalytic reactions, to date.

Among the various metal nanoparticles, non-porous noble metal nanoparticles, such as from gold, platinum, silver, and palladium, are used for catalytic processes because of their high catalytic activity and selectivity towards target species. Their catalytic properties are still unsatisfactory, however, due to their low surface area, which results in insufficient performance. Therefore, catalyst research is focused on the development of new kinds of materials to produce efficient catalysts with high active surface areas compared to the bulk materials. One of the ways of obtaining a high surface area is by

synthesizing porous structures. Porous materials have higher surface areas compared to bulk materials, which results in highly specific catalytic properties. It is well known that porous materials are classified by three different pore size ranges. Micropores are under 2 nm in size, mesopores range from 2 to 50 nm, and macropores are over 50 nm [2].

Porous materials can usually be obtained by two different methods involving hard- and soft-templates. In the hard templates method, the targeted material is synthesized in templates of the desired shape, and thus, this method is limited in practical use [3]. In contrast, the synthesis of porous materials using the soft-template method is much easier to perform due to the solution process, large-scale synthesis, monodisperse size control, and easy process of template removal [3]. The soft-template synthetic method is based on the assembly of surfactants in solution, including P-123, Pluronic® F-127, Brij58®, etc, where the surfactants can form a micelle structure that can support metal nanoparticles.

Platinum (Pt) nanoparticles (NPs) have attracted much attention, particularly as catalysts and electrode materials, due to their unique and excellent catalytic properties. Pt is expensive, however, although it is the most effective catalyst so far that can display excellent performance in fuel cells and sensors. To overcome this disadvantage, many researchers have worked towards enhancing its catalytic activity while reducing the cost *via* the control of its morphology, shape, active surface area, and particle size. Due to these efforts, different types of Pt materials have been synthesized through various methods, although modifications of the shape of Pt NPs are not sufficient to overcome all the problems at this time.

To reduce such problems and enhance the catalytic performance, various types of noble metal-based-materials with porous structures have been reported by many

researchers [4]. Porous Pt NPs are a typical example. Porous Pd and AuNPs have also been used as catalytic materials as alternatives to the Pt based ones [5].

The noble metals are often alloyed with other metals or made into composites with carbon as electrocatalysts. In particular, these materials can be used as electrocatalysts for the detection of many biologically important organic compounds (e.g. glucose, phenolic compounds, and dopamine). For these reasons, the present thesis is focused on the synthesis and characterization of porous noble metals, bimetallic nanoparticles, and composites of metal nanoparticles decorated on carbon, which have a large catalytic surface area. Since they have potential catalytic activity towards biologically important organics, they can be applied in electrochemical sensors that can take advantage of their superior catalytic properties. I have found that these materials are particularly effective for the detection of bisphenol A or glucose *via* the direct oxidation process. Glucose and bisphenol A are the most important target species because glucose is directly related to diabetes mellitus [6], and bisphenol A is an endocrine disrupter that is related to various diseases such as breast cancer, prostate cancer, birth defects, etc [7]. Hence, I am focusing on the demonstration of these nanomaterials for the catalytic oxidation of glucose and bisphenol A. In this thesis, I have synthesized and characterized dendritic Pt, Au@Pt, Au@Pt/Au, Pt@Pd NPs, and Pd NPs embedded N-doped carbon fibers for catalytic reactions involving biologically important organics.

1.2 Motivation of the research

The motivation for this research work is 1) to enhance catalytic performance of noble metals, especially for the catalytic oxidation reaction of organic compounds, and 2) to find new applications of novel porous metals for electrochemical sensor development.

Thus, the research in this thesis is focused on preparing materials with high catalytic performance through the modification of noble metals and composite materials to change their structure and morphology. This includes the development of materials with new shapes, small sizes, more porosity, and homogeneous particles, as well as synthesizing bimetals or metal nanoparticles decorated carbon composites.

1.3 Thesis results

The main goal of this research was to develop and design noble metal based porous NPs for application as electrocatalysts. This work also includes the facile fabrication of electrochemical sensors, which were targeted towards bisphenol A and glucose. The detailed aims and activities of the present study are as follows:

a) To improve their catalytic properties, electrode NPs based on noble metals were synthesised using soft-template and sacrificial methods.
b) To further improve the catalytic properties of electrode materials based on noble metals and noble metal nanoparticles, they were made in different shapes, with porous structures, and in combination with other metals or carbon.
c) To characterize the physical properties of these materials, several types of equipment were used including for X-ray diffraction (XRD), field-emission scanning electron microscopy (FESEM), transmission electron microscopy (TEM), X-ray photoelectron spectroscopy (XPS), and other techniques.
d) To analyse the electrochemical properties of the materials and their sensing performance, this work employed electrochemical experiments, such as cyclic voltammetry, chronoamperometry, and impedance spectroscopy.

The content of each chapter in this thesis is briefly described as follows:

Chapter 1: The chapter introduces the general background of catalysts, and nanoparticles (NPs) for catalysts. The motivation for the aims of the study and the current research are demostrated.

Chapter 2: The chapter presents a literature review on porous NPs used for catalysts and sensing applications, including a brief history and an overview of porous NPs. In addition, the working principles of sensors, including electrochemical phenomena, different noble-metal-based NPs used for electrode fabrication, and various applications using porous NPs are introduced.

Chapter 3: The chapter briefly introduces the materials and chemicals, physical and morphological characterization techniques, and electrochemical characterization methods that were used in this research.

Chapter 4: The chapter describes the synthesis of dendritic platinum nanoparticles (DPNs) using an amphiphilic non-ionic surfactant (Brij-58) and l-ascorbic acid through a sonochemical method. DPNs were characterized by wide-angle X-ray diffraction, small-angle X-ray diffraction, high-resolution transmission electron microscopy, and N_2 adsorption-desorption isotherms. In addition, the cytotoxicity of the NPs was tested using HEK-293 cells.

Chapter 5: The chapter introduces a sensitive sensor prepared for bisphenol A (BPA) detection using DPNs. DPNs which have a high surface area were synthesized by the soft-template method and were coated on gold NPs deposited on a screen-printed carbon electrode. The performance of the DPN modified electrode was compared to that of a platinum black modified electrode. A polyethyleneimine-phosphatidylcholine (PEI-PC) layer was employed to protect the electrode against interference effects from ascorbic

acid, dopamine, acetaminophen, and uric acid, and to enhance its sensitivity. The sensor performance towards BPA detection using amperometry was investigated. In addition, the sensor was evaluated for the detection of BPA in tap water *via* a recovery test.

Chapter 6: The chapter describes the synthesis Au@Pt NPs via the sonochemical method with different molar ratios (e.g. 3:7, 5:5, and 7:3) of Au to Pt precursors. The particle structure was confirmed to be core-shell, and the particle size was estimated for the 3:7, 5:5, and 7:3 ratios of Au to Pt, respectively. The detailed structure and crystallinity of the as-prepared Au@Pt NPs were studied by scanning electron microscopy, transmission electron microscopy with element mapping, and X-ray diffraction. Glucose oxidation using amperometry was undertaken to explore the potential of this material as a glucose sensor.

Chapter 7: The chapter introduces about the synthesis of Au decorated Au@Pt NPs and their use in glucose sensors. Core-shell structured Au@Pt NPs with Au cores and dendritic Pt shells were synthesized using the sonochemical method. Au was then electrochemically incorporated into nano-channels between Pt NPs on Au@Pt NPs (Au@Pt/Au NPs) for a non-enzymatic glucose sensor. The NPs were characterized by wide-angle X-ray diffraction, high-resolution transmission electron microscopy, and their electrochemically active surface area. The sensor performance was determined by amperometry.

Chapter 8: This chapter shows synthetic porous Pd@Pt NPs prepared by Brij 58® or Pluronic® F-127 using the sonochemical method. Due to the different kinds of surfactants, the Pd@Pt NPs have different shapes and morphologies. The NPs were characterized by scanning electron microscopy, wide-angle X-ray diffraction, high-resolution transmission electron microscopy, and electrochemically active surface area measurements.

Chapter 9: The chapter presents a facile synthesis method for palladium NPs-embedded N-doped carbon fibers (Pd/N-C) through electro-polymerization and reduction. Pd/N-C NPs were characterized by wide-angle X-ray diffraction, high-resolution transmission electron microscopy, N_2 adsorption-desorption isotherms, and XPS. Bisphenol A (BPA) was detected by amperometry for two dynamic ranges. To explore the possibility of using this material as a BPA sensor, the detection of BPA was confirmed by amperometry.

Chapter 10: The chapter contains the conclusions of the thesis and general outlook.

1.4 References

[1] G. Busca., Heterogeneous catalytic materials: Solid state chemistry, surface chemistry and catalytic behaviour, 1st ed., Elesevier, Amsterdam, 2014.

[2] B. D. Zdravkov, J. J. Čermák, M. Šefara, J. Janků, Cent. Eur. J. Chem., 2007, **5**, 385-395.

[3] V. Malgras, Q. Ji, Y. Kamachi, T. Mori, F.-K. Shieh, K. C.-W. Wu, K. Ariga, Y. Yamauchi, Bull. Chem. Soc. Jpn., 2015, **88**, 1171-1200.

[4] Y. Xu, B. Zhang, Chem. Soc. Rev., 2014, **43**, 2439-2450.

[5] H. Zhang, M. Jin, Y. Xiong, B. Lim, Y. Xia, Acc. Chem. Res., 2013, **46**, 1783-1794.

[6] M. Brownlee, Nature, 2001, **414**, 813-820.

[7] K. Shim, J. Kim, M. Shahabuddin, Y. Yamauchi, M. S. A. Hossain, J. H. Kim, Sens. Actuators B Chem., 2018, **255**, 2800-2808.

2. Literature review

2.1 Porous catalytic materials

Various catalytic noble metal materials such as gold, platinum, and palladium have been used for specific catalytic processes due to their high activity and selectivity towards target species [1]. The synthesis of catalytic active materials for electrochemical catalysts and sensors that will be used in environmental and medical applications has received considerable attention in recent years. This is due to the rapid growth of the world population coupled with people's increasing life span, exposure to chemicals in the environment, and increasing age-related diseases. For example, diabetes is a global public health problem. It is one of the leading causes of disability and death in the world. Diabetes mellitus is a metabolic disorder that is due to insufficient insulin production or secretion, which causes a high level of glucose in an individual's blood [2]. The estrogen mimics, which are environmental toxins that can lead to various diseases, represent one class of environmental chemicals [3]. Among the various methods to manage and prevent diseases, it is necessary to improve the performance of sensing devices to overcome the limitations of present techniques. This requires the synthesis of new catalytic materials. Among the various materials, porous nanoarchitectures are a key to improving the electrochemical catalysts and sensors. In general, these have been classified into three types: microporous (pore size < 2 nm), mesoporous (2 < pore size < 50 nm), and macroporous (pore size > 50 nm) (Figure 2.1). [4,5] In general, these materials have great potential in catalysts and sensors due to their high surface areas and low specific densities. In particular, noble metal-based porous materials are highly efficient electrocatalysts for the oxidation of small organic molecules such as glucose [6,7], phenolic compounds [8,9], and biological amines [10,11]. They are considered better catalysts for these reactions

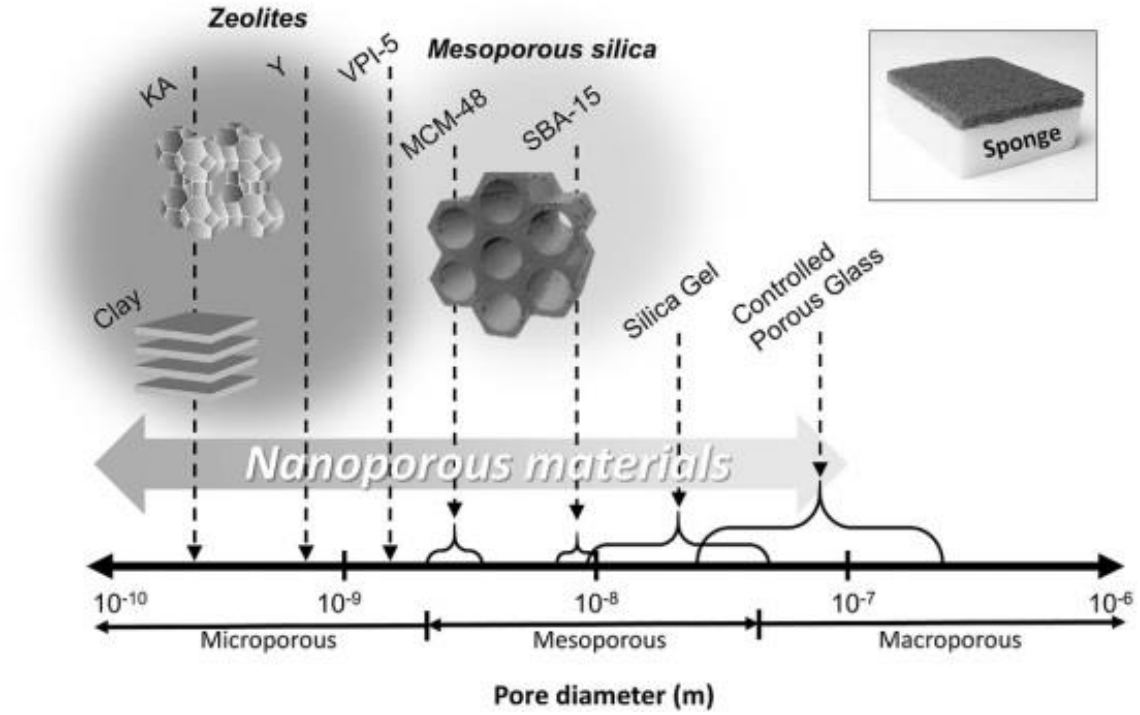

Figure 2.1. Classification of porous materials depending on their pore size [4].
*Nanoporous materials: Pore diameter is nanosized materials.

than non-porous metals. For this reason, these materials have often been used in catalysts and sensors despite being expensive. Various materials, such as bimetallic materials and metals with carbon, have been developed as alternatives.

Bimetallic materials have certain advantages, not only because of the combination of the individual properties characteristic of the two metals, but also due to the synergetic effects of the two metals. Bimetallic materials are synthesised by a range of methods: chemical reduction, thermal decomposition, biosynthesis, galvanic replacement, and sonochemical and radiolytic methods. The particle shapes and sizes of bimetallic materials are precisely determined by their preparation methods and conditions. In addition, the morphology of the metal materials or support materials affect their catalytic activity. Increased active area of the support materials and decreased size of the metallic catalyst improve their performance. For this reason, noble metal-based bimetallic

materials have been attracting attention in the past several years. In addition, noble metal-based materials with carbon hybrids such as Pt/graphene oxide (Pt/GO), Pt/single-walled carbon nanotube (Pt/SWCNT), Pt/multi-walled carbon nanotube (Pt/MWCNT), and Pt/carbon nanofibers (Pt/CNFs) have been steadily developed.

There have been various analytical tools developed to detect target species, including separation analysis, fluorimetry, immunoassay, and electrochemical methods. Of these, the electrochemical method has advantages including a short analysis time, inexpensive instruments, simplicity, and great sensitivity [8]. This method can be easily used for portable devices. For these reasons, researchers have developed enzymatic and non-enzymatic electrochemical sensors using electrochemically active materials. The direct oxidation method, which is a method of detecting target species using a redox reaction, is commonly used. This method requires that the materials have catalytic activity. Electrochemical methods are improved in their performance by the synthesis of materials with higher catalytic activity.

2.2 Synthesis method for porous noble metal based materials

After mesoporous silica using template method was reported in 1992 by Kresge et al. and Beck et al., respectively [12,13], many researchers have been focusing on the synthesis of various porous materials using template methods [14], which have gaining great attention in both industry and academia, due to their unique properties such as tunable pore size, large surface area, and uniform pore size distribution. The synthesis methods are relatively easy and simple to use to obtain porous materials, resulting in interesting morphologies through crystal nucleation and growth. Modifying the morphology by changing the particle size, pore size, or surface area, is an important key to optimizing the material's properties [5,15]. The template methods are mainly classified

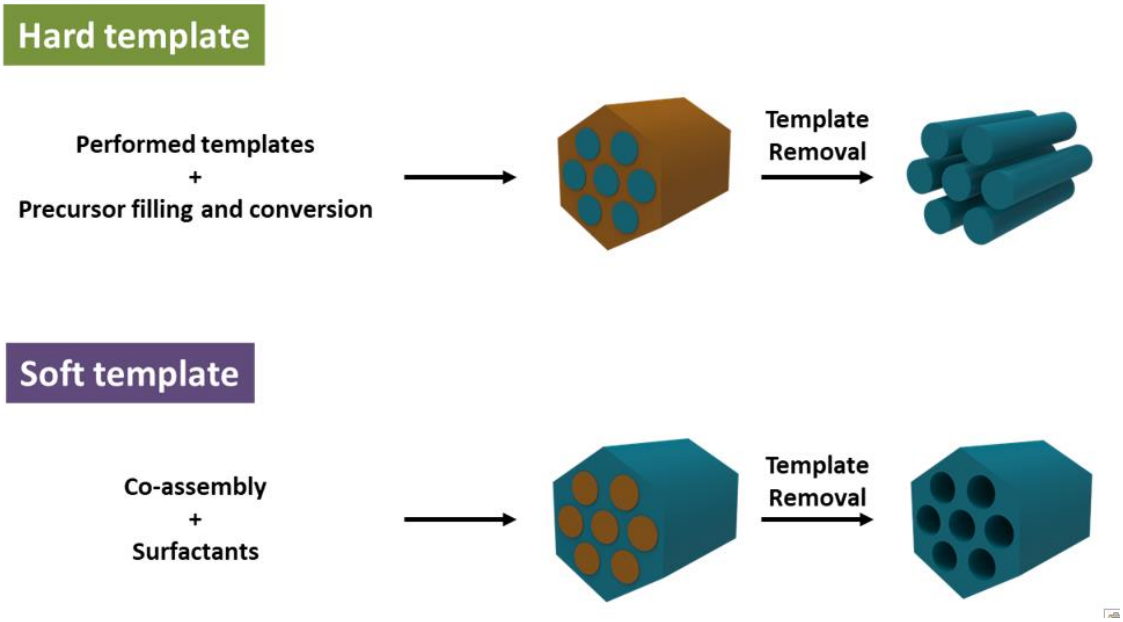

Figure 2.2. The general processes for the hard- and soft- template synthesis methods.

into two classes; the hard-template and the soft-template methods. The hard-template method generally employs silica or anodic aluminum oxide (AAO) as the template. In contract, the soft-template method utilizes surfactants, such as block copolymers and biomolecules. Figure 2.2 shows the general hard- and soft- templates synthesis processes.

2.2.1 Hard templates

A hard template method is used as the common approach for preparing ordered meso/macroscale architectures with metals and carbons, which have well-ordered structures and specific morphologies. Compared to soft templating, this includes three steps for the synthesis of porous nanomaterials; (1) an original template with specific porous structures is prepared, (2) inorganic substances are synthesized using a range of synthetic approaches (e.g. hydrothermal, precipitation, and sol-gel methods), and then, (3) the original template is removed. The morphology of materials is generally a metal replica of the original template. Ordered meso/macroporous materials using MCM-48 [17], and

SBA-15 [18] as templates have been reported. In particular, porous noble metal materials can be easily synthesised by changing template parameters such as surface functionality and pore size controls [19].

Mesoporous silicas as hard templates with a strong framework and stability of high thermal have been used to prepare various types of noble metal structures such as nanowires, nanoworms, and nanoparticles. Ryoo and co-workers developed a meso-structural Pt replica obtained through H_2 reduction that was impregnated into MCM-48 silica [20]. Kuroda et al. employed KIT-6 to synthesise Pt replicas through vapor infiltration of a reductant [21]. In addition, MCM-48 has been used as a hard template to prepare various metal structures with different pore sizes [22].

The morphologies of the resulting mesoporous metal nanostructures have, however, been limited, and most materials were films on the conductive substrates or powders with irregular shapes. The need for new synthetic processes for mesoporous metal structures is related to these limitations in the morphology and particle size. To solve these problems, Yamauchi and co-workers created mesoporous Pt NPs, using KIT-6 [23] and SBA-15 [24] (Figure 2.3a-c) as hard templates. Ascorbic acid (AA) was used in this work for reducing the Pt source. This method is extremely facile and highly reproducible without high temperature. The use of a weak reducing agent such as AA provides enough time for the reductant to access the inner part of the mesoporous silica and Pt can nucleate slowly in the mesoporous silica channel [5]. Various Pt based compositions, such as, Pt–Ru, Pt–Co, and Pt–Ni, have also been reported using the same approach [25,26]. In recent years, hierarchical architectures of nanoporous Pt have been further developed using cage type

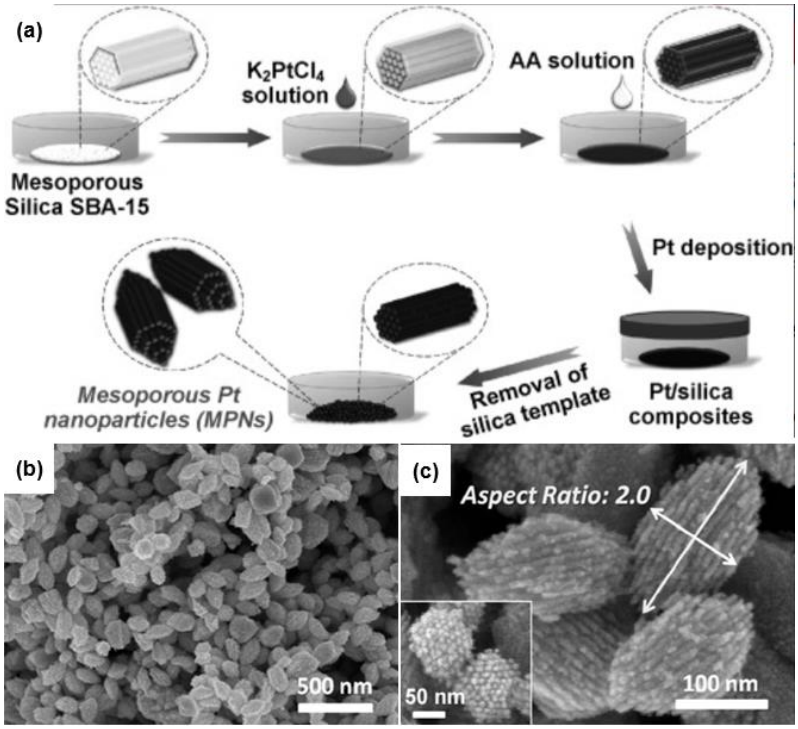

Figure 2.3. (a) Schematic illustration of a synthetic procedure for mesoporous Pt nanoparticles (MPNs). (b, c) SEM images of mesoporous platinum nanoparticlesobtained by using SBA-15 templates [24].

mesoporous silica (LP-FDU-12) as a hard template [27].

2.2.2 Soft templates

The soft-template method uses surfactants, such as block copolymers and bio-molecules, as templates, and these form micelles in the presence of water by self-assembly. Amphiphilic molecules (including block copolymers and surfactants), have hydrophobic and hydrophilic groups, which form the resultant aggregates such as micelles, cylinders, lamellar, and reverse micelles as templates (Figure 2.4) [28]. The micelle structures produce materials with specific structures due to their molecular interactions. The soft-template method is a relatively easy and simple process for the synthesis of materials compared to the hard-template method. The soft-template method is more advantageous for fabricating porous structural materials due to the natural

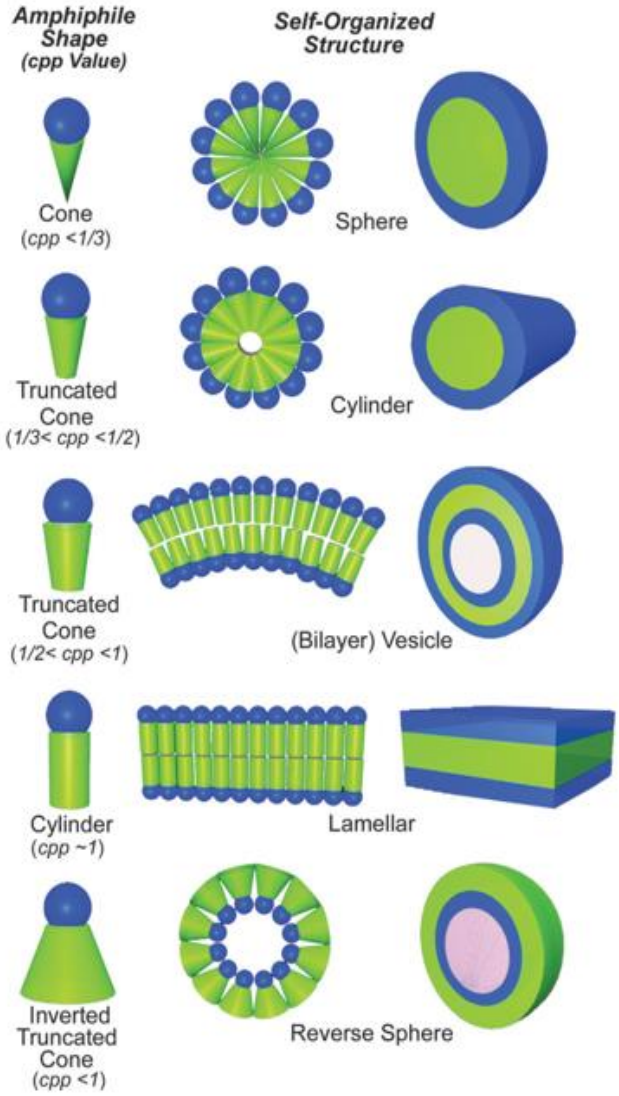

Figure 2.4. Self-organization structures of amphiphilic molecules [28].

abundance and versatile morphology of soft templates. Porous structural materials form aggregations by means of intermolecular or intramolecular interaction forces, such as static electricity, and hydrogen and chemical bonding [29].

When a surfactant is dissolved in water in different concentrations, it is possible to form various stages of the liquid crystal order according to the packing parameters [30]. When inorganic chemicals are added to a surfactant dissolved in water, they interact with the micelles by hydrogen bonding, van der Waals forces, chemical bonding, and static electricity. These results demonstrate that a new interaction between the precursor,

surfactant, and solvent has occurred [29]. The interaction between the liquid crystal phase of the surfactant and the organic-inorganic interface seems to play a decisive role in the formation of mesoporous substances. Most mesoporous materials produced by using surfactants as soft templates are obtained by cooperative assembly, true liquid crystal templates (LCT), and evaporation-induced self-assembly (EISA) [5,16]. In recent years, dendritic Pt nanoparticles (NPs) have been synthesized using a cationic surfactant by Yamauchi and co-workers [31].

Polymers and block copolymers can also be used as soft templates for the synthesis of porous NPs. They have a large molecular weight, high stability, and appropriate molecular structures, which can affect the pore size, pore volume, and surface area [32]. Block copolymers are key element for fabricating mesoporous materials, because they have connected polymer chains with two or more different properties. Their structure and shape can be controlled by using different combinations of blocks. Consequently, the syntheses based on non-Pluronic copolymers as soft-template mostly rely on EISA. Pluronic® F-127 (F-127) as a triblock copolymer has been used for synthesizing mesoporous NPs as well as other block copolymers (Figure 2.5) [33,34]. Figure 2.5a illustrates the synthetic processes and morphologies of various bi- and tri- metallic NPs, such as, PdPt, Au@PdPt, and PdPtCu, using F-127. Figure 2.5b shows the formation process of N-doped mesoporous carbon nanospheres (NMCS) using polystyrene-*b*-poly(ethylene oxide) (PS-*b*-PEO). Using the block copolymers as templates is very beneficial, although, they have the drawback of being vulnerable to high heat treatment. It is still a challenge to solve this problem.

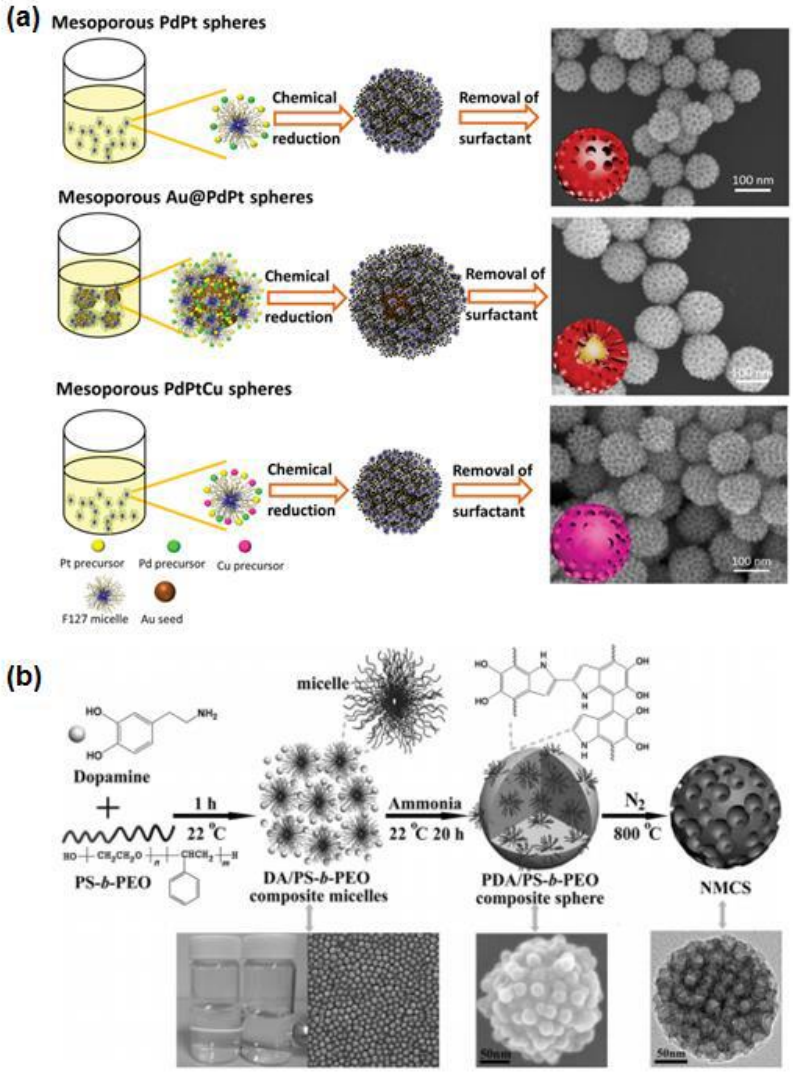

Figure 2.5. (a) Systematic illustration of synthesis of mesoporous bi- (PdPt) and tri- (Au@PdPt and PdPtCu) metallic nanoparticles using F-127 [33], (b) Systematic illustration of the synthesis of NMCS using PS-b-PEO [34].

Biopolymers, including DNA, proteins, and polysaccharides, have great potential as templates due to the advantages of their complex structure, nontoxicity, and easy removal. Many researchers have used biopolymers as templates, such as proteins, DNA, cellulose, etc. In 1991, Mann's group successfully synthesised supramolecular protein cages as templates for different metal nanomaterials [35]. The group used the tobacco mosaic virus (TMV) as a template to synthesise inorganic metal nanotubes [36,37]. The formation of a DNA-silica complex, based on the structure directing effects of N-

trimethoxysilylpropyl-N,N,N-trimethylammonium chloride (TMAPS), was described by Che et al. (Figure 2.6a, b) [38]. Wu et al. synthesised hierarchically porous carbons (HPCs) using cellulose as template [39]. Cicada and butterfly wings have also been used as templates for inorganic nanostructures (Figure 2.6c) [40]. Owing to their unique biomolecule templates, they exhibited excellent electrochemical performances and

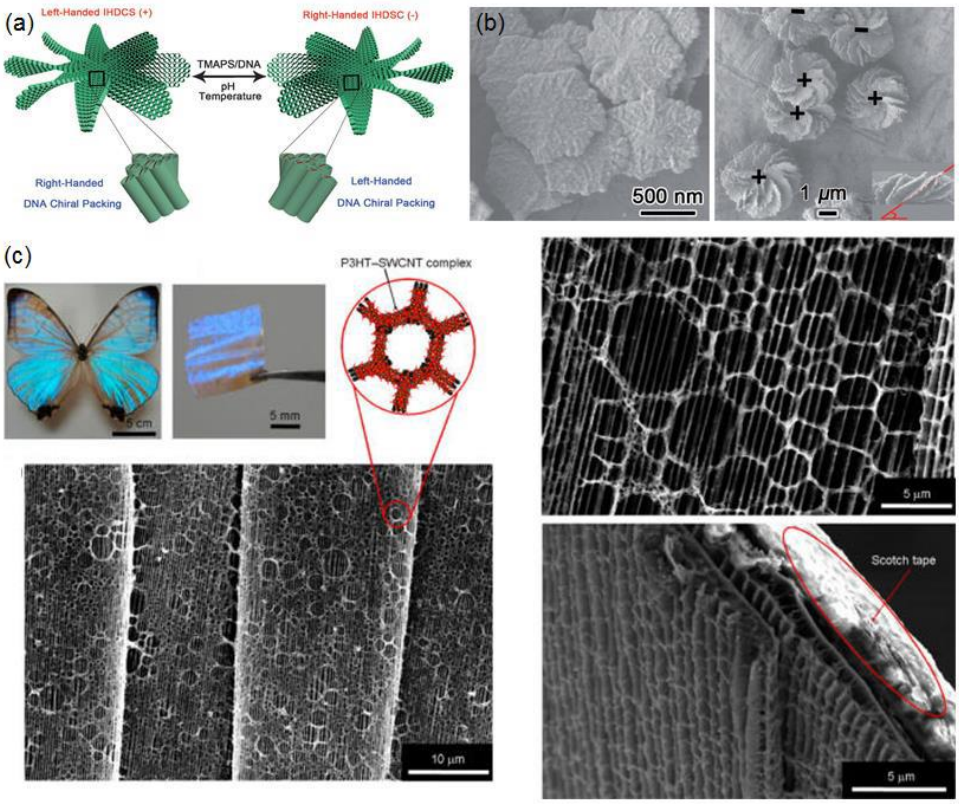

Figure 2.6. (a) Illustration of the macroscopic enantiomeric helical morphologies and corresponding opposite DNA chiral packing of impeller-like helical DNA-silica complexes (IHDSCs) (b) SEM images of the DSCs [38]. (c) Structural characterization of a carbon nanotube (CNT)-butterfly wing composite [40].

catalytic activity. In addition to these methods, various template methods, based on templates such as metal-organic frameworks (MOFs), carbon nanofibers derived from polymers, etc., have also been employed for materials with porous structures.

2.3 Noble metal based porous materials

2.3.1 Porous noble metal materials

In the past several decades, noble metal materials have received considerable attention due to their specific physical and chemical properties, and they have wide applications, as in catalysis, fuel cells, actuators, optics, sensors, and medical therapy [41,42]. Noble metal materials play a crucial role in many heterogeneous catalytic reactions. It is well-known that tuning the size, shape, morphology, and composition strongly affects the properties of materials. Through these modifications, noble metals, such as, Pt, Au, Pd, and Ag, can show enhanced properties for specific applications.

Pt has especially good catalytic and electrical properties [43]. Various Pt morphologies have been studied because increasing the density of catalytic sites is still a critical issue. Various methods, including hydrogen reduction [20] and electrodeposition [44], of impregnation of a Pt precursor into mesoporous silica templates have been developed by many researchers. Attard et al. have reported mesoporous Pt films that were grown using a surfactant-based lyotropic liquid crystal (LLC) through chemical reduction and electrodeposition, respectively [45]. Yamauchi and co-workers synthesized mesoporous Pt nanoparticles using KIT-6 and SBA-15 as hard templates [23,24]. Chengwei et al. produced ordered macro-/mesoporous Pt catalysts using a dual-templating method in 2014 [46]. Kim and co-workers also prepared dendritic mesoporous Pt NPs to check their cytotoxicity for bioapplications [47]. Figure 2.7 shows various noble metal materials, including Pt, Pd, Au, and Ag, that were synthesized using template methods. Nanoporous Pt with a hierarchical architecture was developed using LP-FDU-12 as template (Figure 2.7a) [27]. Since then, such synthesized porous Pt NPs have been applied in various applications and new types of porous Pt NPs are still being reported.

Au nanoparticles (NPs) have also attracted much attention as electrocatalysts, although they have certain disadvantages including a high diffusion coefficient and low thermal stability [28]. Nevertheless, AuNPs with porous structures have been developed by using various synthetic methods. Bartlett et al. described macroporous Au films formed by electrodeposition *via* templates [48]. These films had regular submicron

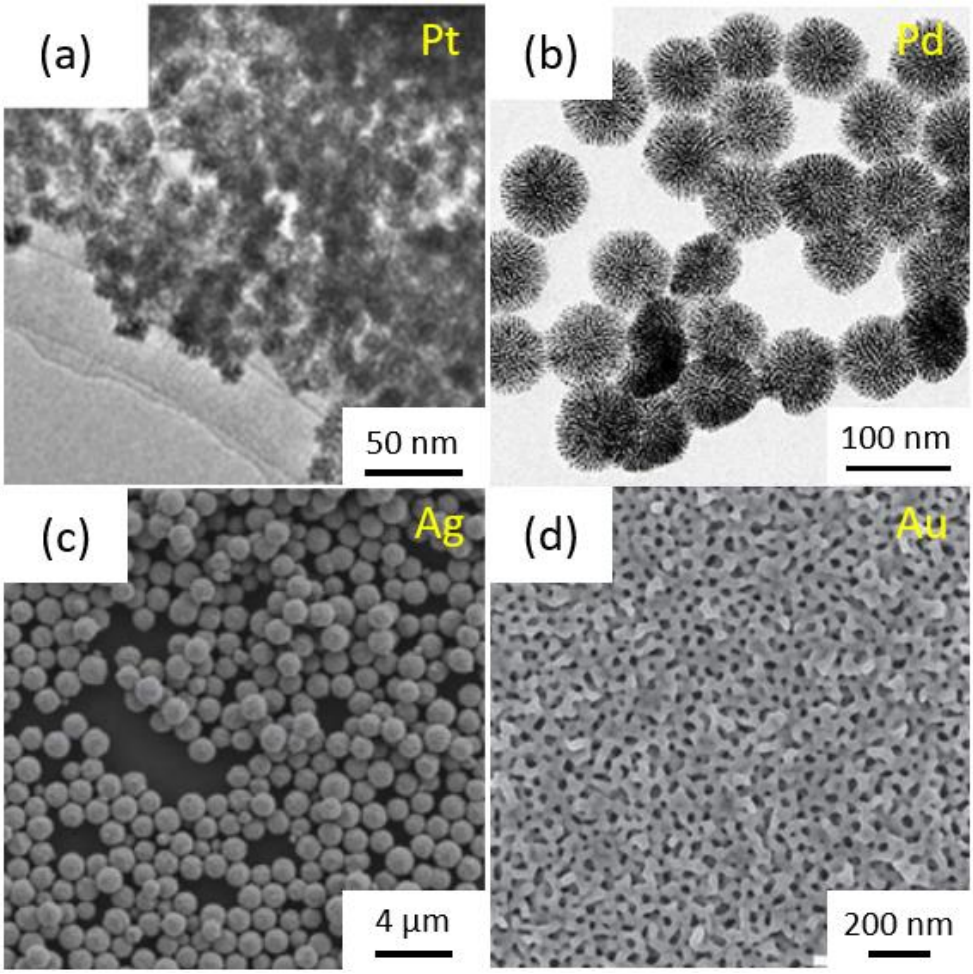

Figure 2.7. TEM images of (a) Pt [27] and (b) Pd [53] porous architectures. SEM images of (c) Ag [52] and (d) Au [50] porous architectures.

spherical holes with strong diffractive optical properties. Hierarchical porous Au films were also developed by the Collinson group in 2012 [49]. Both types of porous Au films have close-packed structures. In 2015, the Yamauchi group synthesized mesoporous gold films using soft-template methods. These films were prepared using PS_{18000}-*b*-PEO_{7500}, and the pore sizes of the Au films were 19 to 40 nm (Figure 2.7d) [50]. Apart from these

noble metals, Ag and Pd porous materials have also been used with various morphologies. In 2010, Ag microspheres synthesized using bacteria as templates were synthesized by the Cui group (Figure 2.7c) [51]. These as-prepared Ag microspheres have a narrow size distribution, and a hollow and porous structure. Huang and co-workers have produced uniform porous Pd nanostructures (Figure 2.7b) [52]. Various noble metal materials with porous structures have exhibited enhanced performance, although they still have cost problems.

2.3.2 Porous noble bimetallic materials and carbon composites decorated with metal nanoparticles

To solve these cost problems and maximize performance, composites were employed to synthesise catalytic materials. Materials composed of two different metal precursors display new catalytic properties arising from both metal elements. In addition, bimetallic materials have many more possibilities for shapes and structures. The structures of bimetallic materials are classified by the distribution modes of the two metal elements,

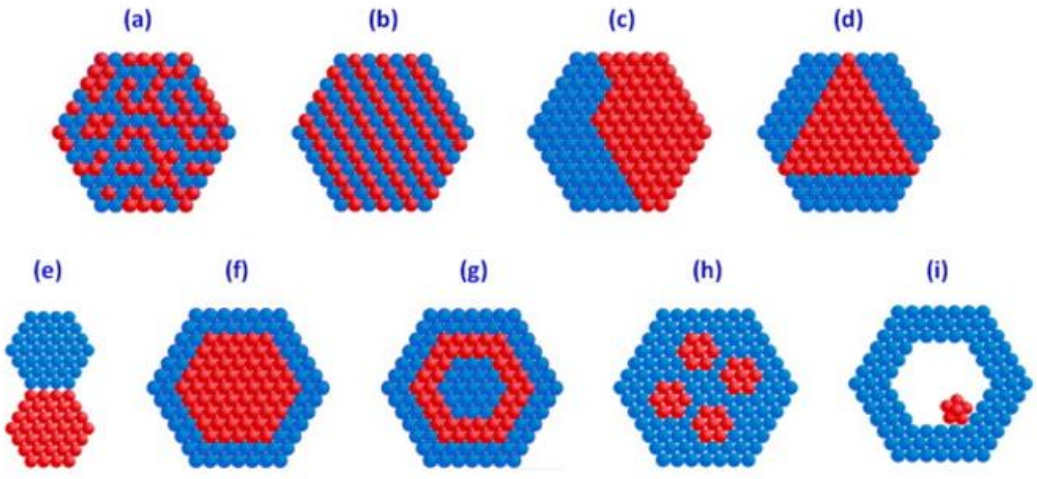

Figure 2.8. Structures of bimetallic nanoparticles: (a) mixed alloys; (b) random alloys; (c) subclusters with two interfaces (d) subclusters with three interfaces; (e) subclusters with small number of A–B bonds; (f) core–shell nanoparticles; (g) multishell core–shell nanoparticles; (h) multiple small core material coated in a single shell material, (i) movable core within hollow shell material [53].

e.g. mixed alloys, random alloys, subclusters with two or three interfaces, core–shell nanoparticles (NPs), multishell core–shell NPs, etc. (Figure 2.8) [53]. When these materials have a porous structure, they improve the catalytic performance.

Pt-based bimetallic porous materials (Pt with Pd, Au, and other metals) have been developed using various template methods. Figure 2.9 displays various Pt based bimetallic materials with many morphologies. Liu et al. have successfully synthesized nanoporous PtCo alloy nanowires using the hard template method (Figure 2.9a) [54]. The Younan Xia group has reported the synthesis of PdPt bimetallic nanodendrites using soft

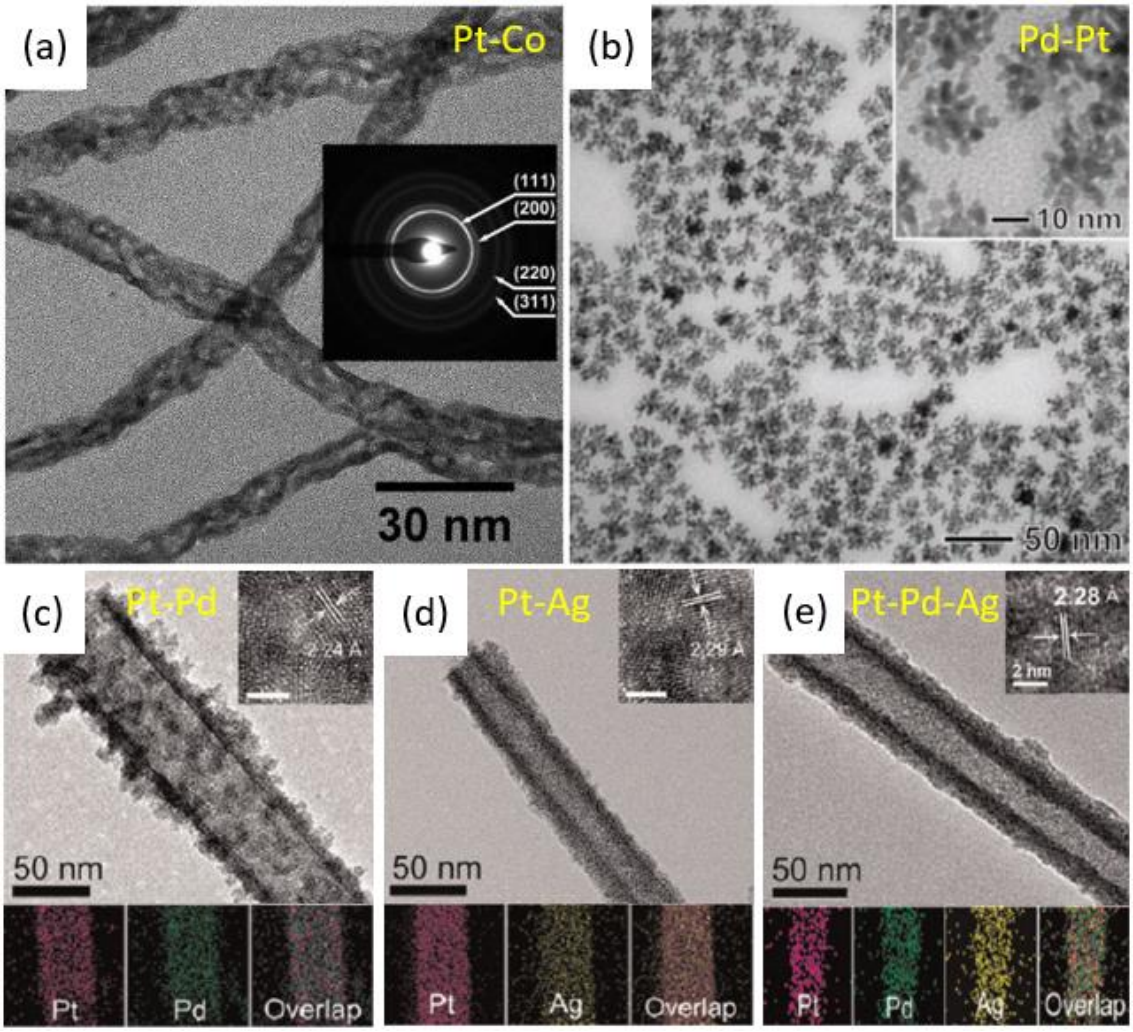

Figure 2.9. TEM images of various Pt-based bimetallic porous materials: (a) nanoporous PtCo alloy nanowires [54], (b) PdPt nanodendrites [55], (c) TEM and EDS mapping images of PtPd alloy nanotubes, (d) TEM and EDS mapping images of PtAg alloy nanotubes, and (e) TEM and EDS mapping images of PtPdAg alloy nanotubes [56].

template methods (Figure 2.9b) [55]. These NPs show high catalytic activity compared to Pt/C. Han and co-workers have successfully prepared multimetallic alloy nanotubes including PtPd, PtAg, PdAg, and PtPdAg [56]. They have produced uniform multicomponent tubular nanostructures using the sacrificial template method (Figure 2.9c-e). Other precious metal-based materials as well as Pt-based materials have also been reported continuously. In addition, hollow PdCu alloy nanospheres were prepared by Lee and co-workers [57]. In recent years, mesoporous AuCu alloy films have been synthesized using block copolymer micelles [58].

Noble metal NPs supported by porous carbon have been attractive for catalytic reactions because of their low cost, large surface area, high aspect ratio, low electrical resistance, and chemical stability. Typical examples are mesoporous carbon with noble metals and carbon nanofibers with noble metals. For example, Ryoo and co-workers have reported ordered nanoporous carbon supporting Pt NPs (around 3 nm) that was synthesized using SBA-15 as a hard template, which had a specific surface area of 2,000 $m^2 g^{-1}$ [59]. Müllen and co-workers synthesized Pt (2 to 5 nm) loaded one-dimensional porous carbon nanotubes (specific surface area: 1,171 $m^2 g^{-1}$) using a template method [60]. In addition, Ying el al. prepared highly dispersed Pt NPs inside unique nitrogen-doped hollow porous carbon polyhedra (Pt@NHPCP) (specific surface area: 516 $m^2 g^{-1}$) from metal-organic frameworks for hydrogen evolution reaction (Figure 2.10a-e) [61]. Chen and co-workers prepared Pt-Co NPs in nitrogen doped hollow porous carbon capsules (PtCo/Co@NHPCC) for the oxygen reduction reaction (Figure 2.10f-j) [62]. These materials displayed new types of synthetic processes for metals combined with carbon materials using other template methods. Pt, as well as other porous carbon

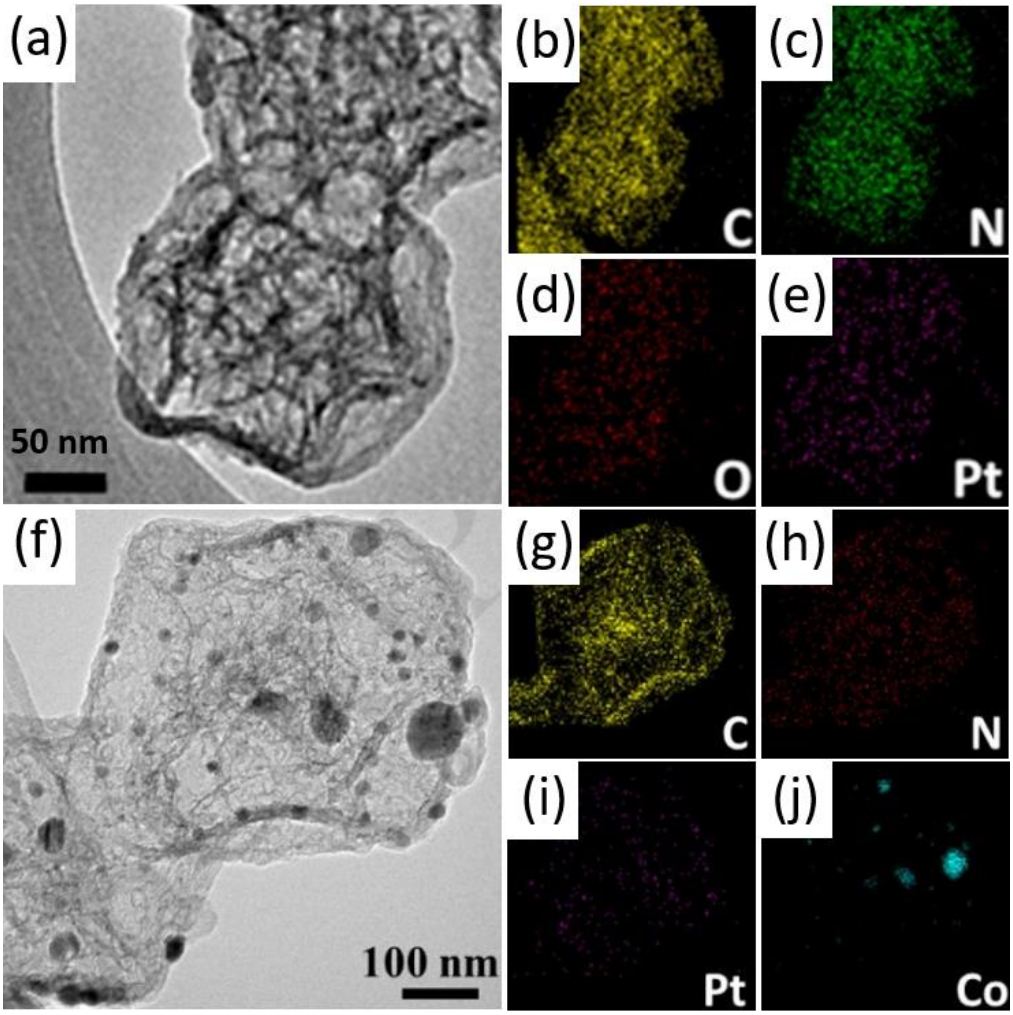

Figure 2.10. (a) TEM image of Pt@NHPCP (b-e) Elemental mapping results for Pt@NHPCP: (b) Carbon, (c) Nitrogen, (d) Oxygen, (e) Platinum [61]. (f) TEM image of PtCo/Co@NHPCC (g-j) Elemental mapping results for PtCo/Co@NHPCC: (g) Carbon, (h) Nitrogen, (i) Platinum, (j) Cobalt [62].

supported noble metals based materials (Pd [63,64], Pd_3Cu [65], PtCo [66], PtNi [67], and PtRu [68]), which are still being developed.

2.4 Electrocatalytic reactions

The electrode reaction generally involves the mass transfer of reactants and products towards or away from the electrode surface through chemical reactions, followed by adsorption of ionic species on the electrode surface [69]. In many cases, the electron transfer reaction is associated with a homogeneous reaction involving the oxidant or reductant. Based on this reaction, electrochemical methods can be used to obtain

thermodynamic and kinetic information and can be applied to many solvents, making them widely applicable to the study of reactions between organic and inorganic species.

The analytical methods for the detection of target species have included several techniques such as separation analysis [70], fluorimetry [71], and immunoassay [72]. These methods have some disadvantages: they demand sophisticated instruments, complex preparation of NPs, tedious sample treatments, and long analysis times. On the other hand, electrochemical methods can feature short analysis times, simplicity, and great sensitivity [8]. For this reason, various electrochemical sensors using noble-metal-based electrodes have been developed to detect various target species, including glucose, ascorbic acid, dopamine, and phenolic compounds. In these cases, the sensor is required to be superior in sensitivity, size, power consumption, stability, selectivity, and cost.

2.4.1 Glucose

Among the various diseases, diabetes mellitus is a metabolic disorder that is due to insufficient insulin production or secretion, which causes a high level of glucose in an individual's blood. Chronic high glucose levels can lead to heart disease, kidney failure, and blindness [73]. Around 400 million people have diabetes mellitus, and it has greatly contributed to deaths worldwide over past decades [74,75]. Thus, the quantitative monitoring of blood glucose and its management are of clinical importance, because it can significantly reduce the risks of diabetes related health complications. Simple glucose monitoring has become even more important in terms of reducing the financial burden stemming from diabetes and its severe complications. The key to management of diabetes patients is to accurately monitor and control the body's glucose levels [76]. The aim of most diabetic treatments is to maintain a patient's blood glucose levels within healthy physiological boundaries. Glucose monitoring is commonly achieved by finger-prick

blood tests several times a day using electrochemical testing strips. The monitoring systems require external calibration, but the development of calibration-free devices could remove the human error associated with current calibration processes. Continuous glucose monitoring of body fluids is attractive for the precise diagnosis and management of the disease.

Electrochemical glucose sensors are classified as enzymatic and non-enzymatic. Enzymatic sensors use glucose oxidase (GOx) or glucose dehydrogenase (GDH), which

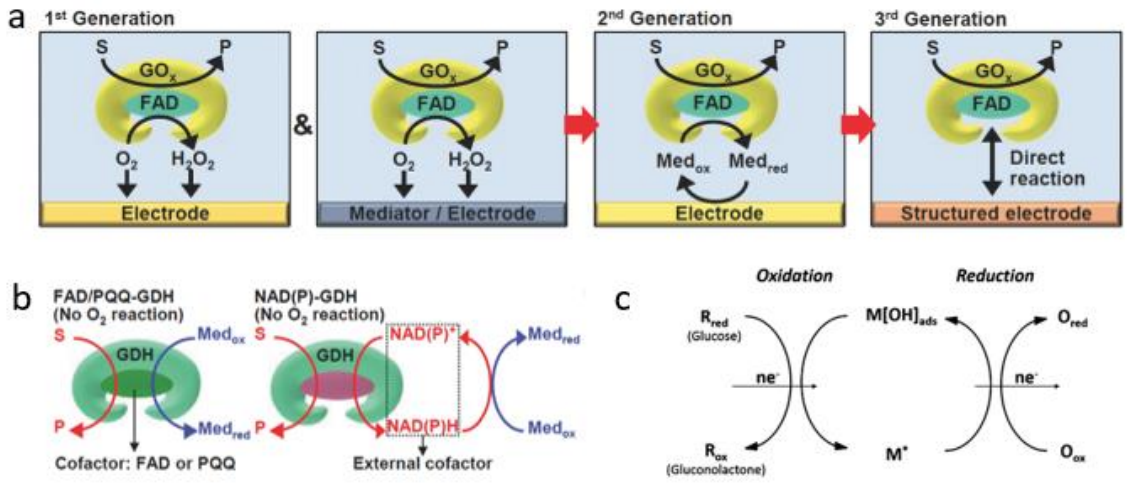

Figure 2.11. Sensing principles of the enzymatic glucose sensor (a) Schematic illustrations showing the GOx-based glucose sensors. (b) Schematic illustrations showing the sensing mechanism of FAD/PQQ-GDH (left) and NAD(P)-GDH (right) glucose sensor [78]. (c) sensing principles of the non-enzymatic glucose sensors [75].

are relatively low in price, highly bioactive, and stable. GOx-based glucose sensors have gone through three generations. The first generation represents the amount of glucose consumed by reacting with the electrodes by consumed O_2 or H_2O_2 produced [77]. The second-generation sensors feature redox mediators that interact directly with the enzyme. Finally, the third generation uses a structurally engineered enzyme to facilitate direct electron exchange between the electrodes and embedded enzyme. Otherwise, GDH-based O_2 supply problems can be avoided because GDH is unable to utilize O_2 [78]. Figure 2.11

shows sensing principles of the enzymatic glucose sensor and the non-enzymatic glucose sensor.

Non-enzymatic glucose sensors use another method, and this is based on the direct electrochemistry of glucose oxidation. This method requires electrochemically active electrode materials, including metals, metal oxides, and carbon. Among the various electrode materials, noble metal based catalytic materials with specific structures, including films, alloys, and core-shell composites, have been widely used as electrodes for non-enzymatic glucose sensors. For example, Asahi and co-workers have reported

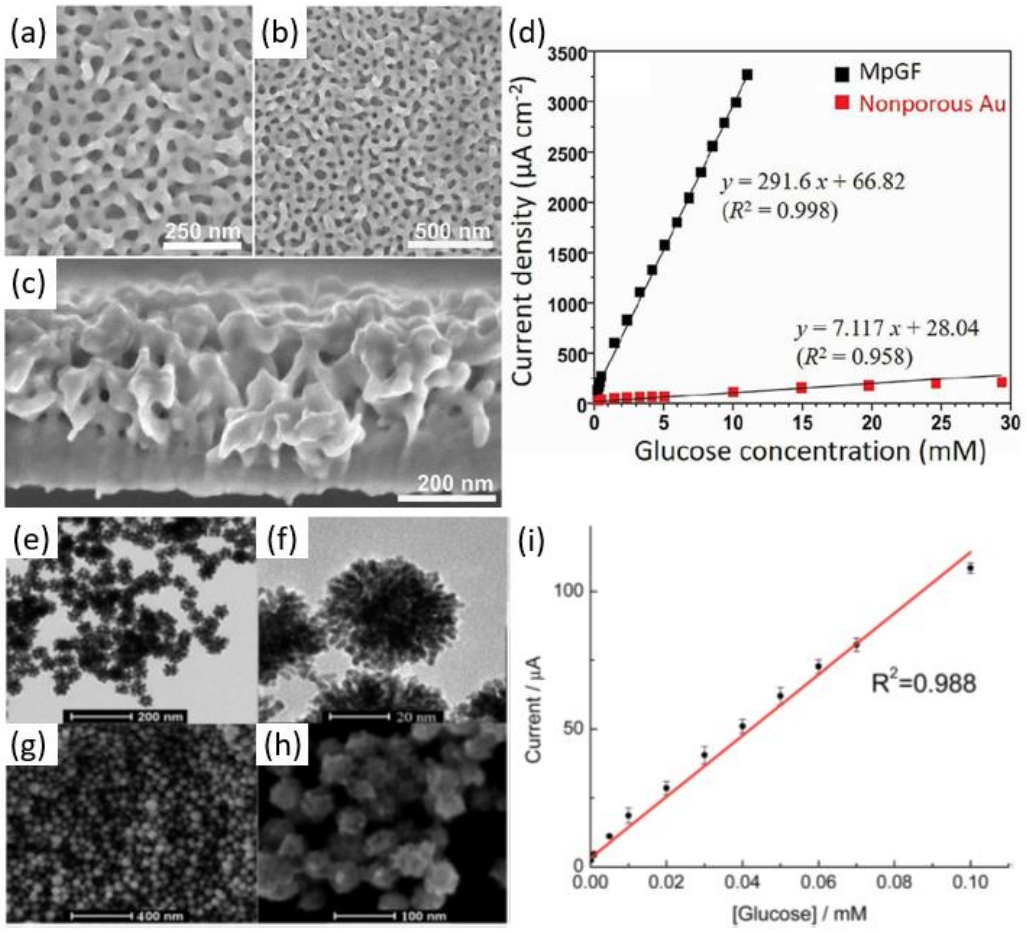

Figure 2.12. SEM image of mesoporous Au film (MpGF): (a) high- and (b) low-magnification, and (c) cross-section, (d) Plot of the amperometric current response to the concentration of glucose. [79]. TEM images of AuPt nanodendrites: (e) low- and (f) high-magnification; SEM images of mesoporous AuPt nanodendrites: (g) low- and (h) high-magnification; (i) the calibration plot for glucose detection using Au/Pt nanodendrite modified electrode [80].

mesoporous gold films using soft-template methods, and the electrodes have shown evidence of wide dynamic ranges between 0.01 and 10 mM in 0.1 M NaOH (Figure 2.12a-d) [79]. Song et al. studied mesoporous Au/Pt dendrites prepared by soft-templating, with the electrode displaying a dynamic range of 0.01–100 mM in 0.1 M NaOH (Figure 2.12e-i) [80]. In addition, Kim and co- workers have developed a non-enzymatic sensor using Au decorated Au@Pt NPs [81]. Many noble-metal based materials as electrode have also studied for use in non-enzymatic glucose sensors [82]. The electrode materials for non-enzymatic glucose sensors commonly have drawbacks, including poor stability, easy loss of activity, and surface poisoning from the adsorbed intermediates in neutral pH. To overcome these disadvantages, Wang and co-workers synthesized macroporous carbon decorated with dendritic Pt NPs for glucose detection in pH 7.4 [83]. PtPd/mesoporous carbon vesicles have also been developed by Guo and co-workers, and the PtPd/mesoporous carbon vesicle modified electrode showed a dynamic range from 1.5 to 12 mM in PBS with pH 7.4 [84]. Nugraha et al. also synthesized mesoporous Au-Cu alloy films as glucose sensors using block copolymer micelles [7].

2.4.2 Phenolic compounds

The biological and bioavailability efficacy of phenolic compounds are strongly influenced by enzymes [85]. Phenolic compounds, including polyphenols, have a potential role in the prevention and treatment of human diseases [86]. Phenolic compounds including bisphenols, which have possible toxic effects on the environment and constitute threats to human health, were also studied [87], however. Bisphenols are defined as compounds consisting of two phenolic nuclei linked by a hydrocarbon bridge.

Of these, bisphenol A, 2,2'-bis(4-hydroxyphenol)propane (BPA), is the most representative of this group.

BPA is used to produce polycarbonate-based plastics and epoxy resins, and these can be easily found in our daily lives. For example, polycarbonate plastics have mainly been used for food containers and drink packaging, and epoxy resins have been employed to coat metal products (e.g. food cans, bottle tops) [88,89]. BPA is an estrogenic environmental toxin and has adverse effects which can be lead to various diseases (e.g. breast cancer, prostate cancer, birth defects, infertility, and obesity) [90,91]. The most common polycarbonate-based products that are used contain BPA due to its cost-effectiveness. This is because the BPA-free polycarbonate plastics are more expensive than BPA-containing products. For these reasons, the detection of BPA is of importance for our health.

BPA is electrochemically active, but direct electrochemical oxidation of BPA offers poor detection sensitivity. In addition, oxidation of BPA in the unmodified electrode results in the formation of oxidation products that contaminate the electrode. To overcome these disadvantages, new electrode materials with high stability, good catalytic activity, and good conductivity must be developed. Many electrochemical BPA sensors have been constructed involving porous materials as electrode materials. Among these materials, noble metal-based materials have been studied for BPA sensors. Kim and co-workers have developed dendritic Pt NPs and Pd NPs-embedded N-doped porous carbon fibers [8,92]. By using the amperometry technique, they obtained two dynamic ranges due to the different kinetics at different concentrations of BPA. Most recently, not only this, but

coupling nanoporous gold leaf and self-assembled cyclodextrin for BPA sensors have been developed [93]. Besides, BPA sensors using porous gold based materials were produced [94,95]. Yan et al and Wannapob et al. proposed very promising biomarker detection, food testing, and environmental monitoring. In addition, Huang et al. prepared molybdenum disulfide nanoflower-chitosan-Au NPs composites as electrode materials

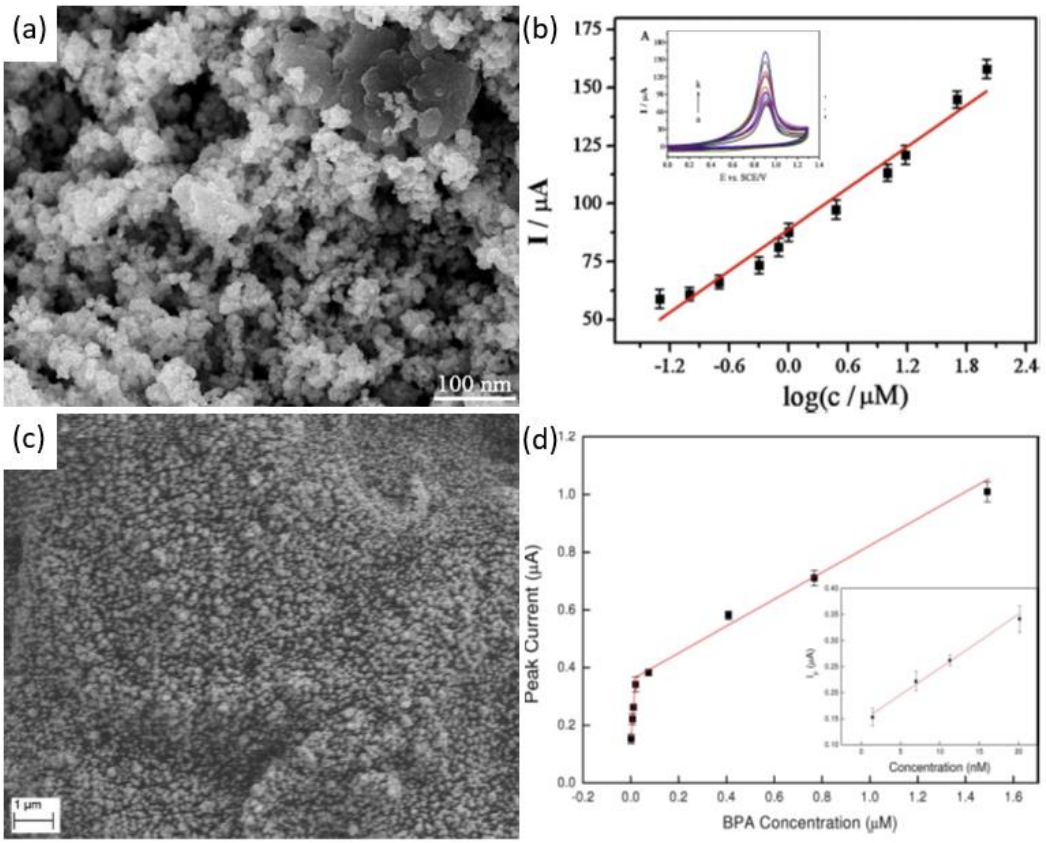

Figure 2.13. (a) SEM image of AuNPs/MoS_2. (b) Relationship between the peak current and the concentration of BPA (Inset: Cyclic voltammograms of BPA AuNPs/MoS_2/GCE in 0.1 M PBS (pH 7.0)) [96]. (c) SEM image of RGO/CNT/AuNPs. (d) DPV peak currents for BPA detection in two linear ranges of 1.45 to 20 nM and 20 to 1,490 nM (Inset: expanded view of measurements of 1.45 to 20 nM of BPA) [97]. GCE: glassy carbon electrode; DPV: differential pulsed voltammetry.

(Figure 2.13a,b) [96]. Wang et al. fabricated a sensitive bisphenol A sensor using a nanocomposite of reduced graphene oxide (RGO), carbon nanotubes (CNTs), and gold NPs (Figure 2.13c,d) [97]. Through this continuous study, the development of BPA sensors has made steady progress.

2.4.3 Biologically important organics (Dopamine, uric acid, and ascorbic acid)

In recent decades, detection of neurotransmitters in the extracellular fluid of the central nervous system and serum has gained attention. Neurotransmitters, such as, ascorbic acid (AA), dopamine (DA), and uric acid (UA), play an important role in the metabolism of the human body. AA is an essential nutrient for humans and is widely used as an antioxidant for the prevention and treatment of colds, scurvy, mental illness, cancer, and AIDS [98,99]. DA is a catecholamine neurotransmitter in the mammalian central nervous system belonging to the excitatory neurotransmitter family. A deficiency of DA is linked to neurological disorders (e.g. schizophrenia and Parkinson's disease) [100,101]. UA is the primary final product of purine metabolism, and is present in serum and urine. Abnormal levels of UA can lead to hyperuricemia and gout [102,103]. In general, AA, DA, and UA are substances that co-exist in a real biological matrix and can be oxidized at nearly the same potential on conventional electrodes.

Various noble-metal based materials have been used as modified electrodes for the electrochemical detection of neurotransmitters. Choi and co-workers prepared 3D nanoporous gold thin films as electrode materials for simultaneous electrochemical detection of DA and AA [104]. They were measured in human serum samples using the differential pulse voltammetry (DPV) method. Zhao et al., prepared hierarchical nanoporous PtTi alloy materials for simultaneous detection of AA, DA, and UA [98] using the DPV method. Noble metal-based materials combined with carbon or graphene based materials have also attracted interest for the detection of AA, DA, and UA. For instance, Chen et al. reported porous bimetallic alloyed PdAg nanoflowers supported on reduced graphene oxide for the detection of AA, DA, and UA with good anti-interference

using the DPV method [105]. Activated graphene/MWCNT nanocomposite loaded Au nanoclusters have prepared for the simultaneous detection of ascorbic acid, dopamine, uric acid and folic acid by Shim and co-workers [106]. Liu and co-workers also synthesized electrospun carbon nanofibers decorated with AgPt bimetallic NPs for dopamine detection [107]. Zou et al. have reported reduced graphene oxide with

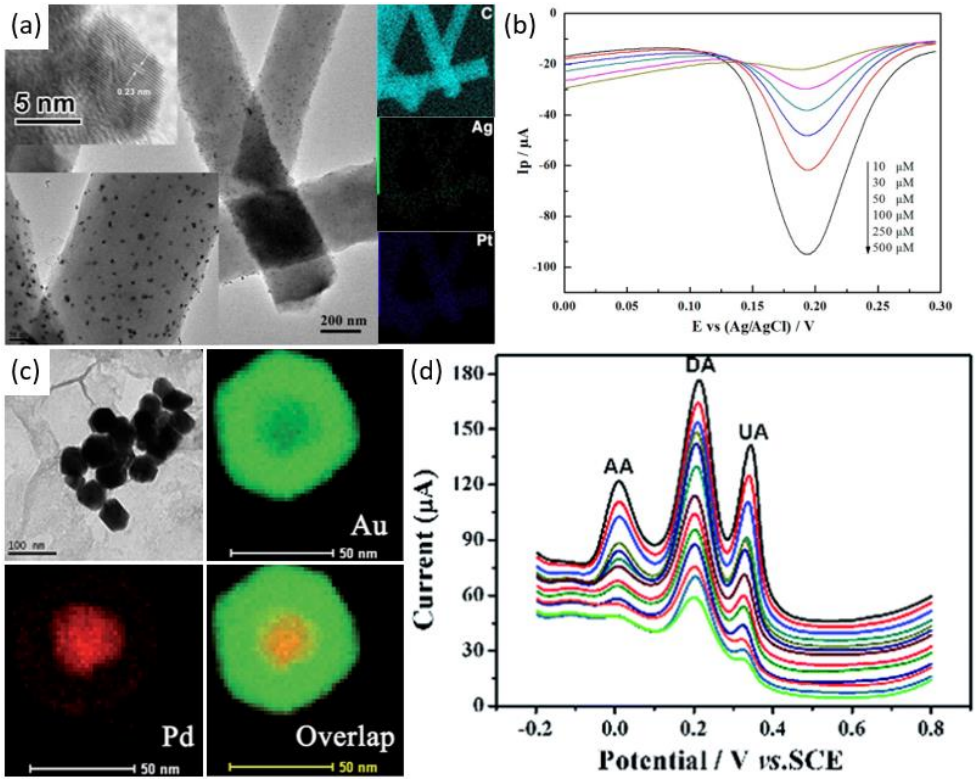

Figure 2.14. (a) TEM images of AgPt/pCNFs and the corresponding elemental mapping. (b) DPV curves of different concentrations of DA (10, 30, 50, 100, 250, 500 μM) on AgPt/pCNFs/GCE [107]. (c) TEM image of Pd@Au/RGO nanocomposite with corresponding elemental mapping (d) DPV curves of Pd@Au/RGO/GCE containing different concentrations of AA from 50 to 2856.63 μM, DA from 1 to 400.56 μM, and UA from 5 to 680.76 μM [108].

bimetallic Pd@Au as a nanocomposite for the detection of dopamine [108]. Neurotransmitter detection based on electrochemical methods is still being reported [109,110].

2.5 References

[1] G. Busca., Heterogeneous catalytic materials: Solid state chemistry, surface chemistry and catalytic behaviour, 1st ed., Elesevier, Amsterdam, 2014.

[2] J. Wang, Electroanalysis, 2001, **13**, 983-988.

[3] L. N. Vandenberg, R. Hauser, M. Marcus, N. Olea, W. V. Welshons, Reproductive Toxicol., 2007, **24**, 139-177.

[4] B. D. Zdravkov, J. J. Čermák, M. Šefara, J. Janků, Cent. Eur. J. Chem., 2007, **5**, 385-395.

[5] V. Malgras, H. Ataee-Esfahani, H. Wang, B. Jiang, C. Li, K. C.-W. Wu, J. H. Kim, Y. Yamauchi, Adv. Mater., 2016, **28**, 993-1010.

[6] J. Yang, X. Liang, L. Cui, H. Liu, J. Xie, W. Liu, Biosens. Bioelectron., 2016, **80**, 171-174.

[7] A. S. Nugraha, V. Malgras, M. Iqbal, B. Jiang, C. Li, Y. Bando, A. Alshehri, J. Kim, Y. Yamauchi, T. Asahi, ACS Appl. Mater. Interfaces, 2018, **10**, 23783-23791.

[8] K. Shim, J. Kim, M. Shahabuddin, Y. Yamauchi, M. S. A. Hossain, J. H. Kim, Sens. Actuators B Chem., 2018, **255**, 2800-2808.

[9] R. Wannapo, P. Thavarungkul, S. Dawan, A. Numnuam, W. Limbut, P. Kanatharana, Electroanalysis, 2017, **29**, 472-480.

[10] D. Zhao, G. Yu, K. Tian, C. Xu, Biosens. Bioelectron., 2016, **82**, 119-126.

[11] Y. Huang, Y.-E Miao, S. Ji, W. W. Tjiu, T. Liu, ACS Appl. Mater. Interfaces, 2014, **6**, 12449-12456.

[12] C. T. Kresge, M. E. Leonowicz, W. J. Roth, J. C. Vartuli, J. S. Beck, Nature, 1992, **359**, 710-712.

[13] J. S. Beck, J. C. Vartuli, W. J. Roth, M. E. Leonowicz, C. T. Kresge, K. D. Schmitt, C. T-W. Chu, D. H. Olson, E. W. Sheppard, S. B. McCullen, J. B. Higgins, J. L. Schlenker, J. Am. Chem. Soc., 1992, **114**, 10834-10843.

[14] V. Malgras, Q. Ji, Y. Kamachi, T. Mori, F.-K. Shieh, K. C.-W. Wu, K. Ariga, Y. Yamauchi, Bull. Chem. Soc. Jpn., 2015, **88**, 1171-1200.

[15] H. Zhang, M. Jin, Y. Xiong, B. Lim, Y. Xia, Acc. Chem. Res., 2013, **46**, 1783-1794.

[16] N. D. Petkovich, A. Stein, Chem. Soc. Rev., 2013, **42**, 3721-3739.

[17] R. Ryoo, S. H. Joo, S. Jun, J. Phys. Chem. B, 1999, **103**, 37, 7743-7746.

[18] S. Jun, S. H. Joo, R. Ryoo, M. Kruk, M. Jaroniec, Z. Liu, T. Ohsuna, O. Terasaki, J. Am. Chem. Soc., 2000, **122**, 10712-10713.

[19] C. Zhu, D. Du, A. Eychmüller, Chem. Rev., 2015, **115**, 8896-8943.

[20] H. J. Shin, R. Ryoo, Z. Liu, O. Terasaki, J. Am. Chem. Soc., 2001, **123**, 1246-1247.

[21] Y. Doi, A. Takai, Y. Sakamoto, O. Terasaki, Y. Yamauchi, K. Kuroda, Chem. Commun., 2010, **46**, 6365-6367.

[22] Z. Liu, Y. Sakamoto, T. Ohsuna, K. Hiraga, O. Terasaki, C. H. Ko, H. J. Shin, R. Ryoo, Angew. Chem. Int. Ed., 2000, **39**, 3107-3110.

[23] H. Wang, M. Imura, Y. Nemoto, S.-E. Park, Y. Yamauchi, Chem. Asian J., 2012, **7**, 802-808.

[24] H. Wang, H. Y. Jeong, M. Imura, L. Wang, L. Radhakrishnan, N. Fujita, T. Castle, O. Terasaki, Y. Yamauchi, J.Am. Chem. Soc., 2011, **133**, 14526-14529.

[25] P. Karthika, H. Ataee-Esfahani, Y.-H. Deng, K. C.-W. Wu, N. Rajalakshmi, K. S. Dhathathreyan, D. Arivuoli, K. Ariga, Y. Yamauchi, Chem. Lett., 2013, **42**, 447-449.

[26] P. Karthika, H. Ataee-Esfahani, H. Wang, M. A. Francis, H. Abe, N. Rajalakshmi, K. S. Dhathathreyan, D. Arivuoli, Y. Yamauchi, Chem. Asian J., 2013, **8**, 902-907.

[27] K. Kani, V. Malgras, B. Jiang, M. S. A. Hossain, S. M. Alshehri, T. Ahamad, R. R. Salunkhe, Z. Huang, Y. Yamauchi, Chem. Asian J., 2018, **13**, 106-110.

[28] M. Ramanathan, L. K. Shrestha, T. Mori, Q. Ji, J. P. Hill, K. Ariga, Phys. Chem. Chem. Phys., 2013, **15**, 10580-10611.

[29] Y. Xie, D. Kocaefe, C. Chen, Y. Kocaefe, J. Nanomaterials, 2016, 2302595.

[30] R. Nagarajan, Langmuir, 2002, **18**, 31-38.

[31] K. Kani, M. B. Zakaria, J. Lin, A. A. Alshehri, J. Kim, Y. Bando, J. You, M. S. A. Hossain, J. Bo, Y. Yamauchi, Bull. Chem. Soc. Jpn., 2018, **91**, 1333-1336.

[32] Y. Deng, J. Wei, Z. Sun, D. Zhao, Chem. Soc. Rev., 2013, **42**, 4054-4070.

[33] B. Jiang, C. Li, M. Imura, J. Tang, Y. Yamauchi, Adv. Sci., 2015, **2**, 1500112.

[34] J. Tang, J. Liu, C. Li, Y. Li, M. O. Tade, S. Dai, Y. Yamauchi, Angew. Chem. Int. Ed., 2015, **54**, 588-593.

[35] F. C. Meldrum, V. J. Wade, D. L. Nimmo, B. R. Heywood, S. Mann, Nature, 1991, **349**, 684-687.

[36] W. Shenton, T. Douglas, M. Young, G. Stubbs, S. Mann, Adv. Mater., 1999, **11**, 253-256.

[37] C. E. Fowler, W. Shenton, G. Stubbs, S. Mann, Adv. Mater., 2001, **13**, 1266-1269.

[38] B. Liu, L. Han, S. Che, Angew. Chem. Int. Ed., 2012, **51**, 923-927.

[39] S. Dutta, S.-Y. Huang, C. Chen, J. E. Chen, Z. A. Alothman, Y. Yamauchi, C.-H. Hou, K. C.-W. Wu, ACS Sustain. Chem. Eng., 2016, **4**, 1885-1893.

[40] E. Miyako, T. Sugino, T. Okazaki, A. Bianco, M. Yudasaka, S. Iijima, ACS Nano, 2013, 7, 8736-8742.

[41] S. Guo, E. Wang, Nano Today, 2011, **6**, 240-264.

[42] J. Gong, G. Li, Z. Tang, Nano Today, 2012, **7**, 564-585.

[43] Z. Peng, H. Yang, Nano Today, 2009, **4**, 143-164.

[44] C.-W. Wu, Y. Yamauchi, T. Ohsuna, K. Kuroda, J. Mater. Chem., 2006, **16**, 3091-3098.

[45] G. S. Attard, P. N. Bartlett, N. R. B. Coleman, J. M. Elliott, J. R. Owen, J. H. Wang, Science, 1997, **278**, 838-840.

[46] C. Zhang, H. Yang, T. Sun, N. Shan, J. Chen, L. Xu, Y. Yan, J. Power Sources, 2014, **245**, 579-582.

[47] K. Shim, J. Kim, Y.-U. Heo, B. Jiang, C. Li, M. Shahabuddin, K. C.-W. Wu, M. S. A. Hossain, Y. Yamauchi, J. H. Kim, Chem. Asian J., 2017, **1**, 21-26.

[48] P. N. Bartlett, J. J. Baumberg, Peter R. Birkin, M. A. Ghanem, M. C. Netti, Chem. Mater., 2002, **14**, 2199-2208.

[49] B. Zhao, M. M. Collinson, J. Electroanal. Chem., 2012, **684**, 53-59.

[50] C. Li, Ö. Dag, T. D. Dao, T. Nagao, Y. Sakamoto, T. Kimura, O. Terasaki, Y. Yamauchi, Nature Commun., 2015, **6**, 6608.

[51] D.-P. Yang, S. Chen, P. Huang, X. Wang, W. Jiang, O. Pandoli, D. Cui, Green Chem., 2010, **12**, 2038-2042.

[52] X. Huang, Y. Li, Y. Chen, E. Zhou, Y. Xu, H. Zhou, X. Duan, Y. Huang, Angew. Chem., 2013, **125**, 2580-2584.

[53] A. Zaleska-Medynska, M. Marchelek, M. Diak, E. Grabowska, Adv. Colloid Interface Sci., 2016, **229**, 80-107.

[54] L. Liu, E. Pippel, R. Scholz, U. Gösele, Nano Lett., 2009, **9**, 4352-4358.

[55] B. Lim, M. Jiang, P. H. C. Camargo, E. C. Cho, J. Tao, X. Lu, Y. Zhu, Y. Xia, Science, 2009, 324, 1302-1305.

[56] B.-S. Choi, Y. W. Lee, S. W. Kang, J. W. Hong, J. Kim, I. Park, S. W. Han, ACS Nano, 2012, **6**, 5659-5667.

[57] S.-H. Han, J. Bai, H.-M. Liu, J.-H. Zeng, J.-X. Jiang, Y. Chen, J.-M. Lee, ACS Appl. Mater. Interfaces, 2016, **8**, 30948-30955.

[58] A. S. Nugraha, V. Malgras, M. Iqbal, B. Jiang, C. Li, Y. Bando, A. Alshehri, J. Kim, Y. Yamauchi, T. Asahi, ACS Appl. Mater. Interfaces, 2018, **10**, 23783-23791.

[59] S. H. Joo, S. J. Choi, I. Oh, J. Kwak, Z. Liu, O. Terasaki, R. Ryoo, Nature, 2001, **412**, 169-172.

[60] G. Cui, L. Zhi, A. Thomas, U. Kolb, I. Lieberwirth, K. Müllen, Angew. Chem., 2007, **119**, 3534-3537.

[61] J. Ying, G. Jiang, Z. P. Cano, L. Han, X.-Y. Yang, Z. Chen, Nano Energy, 2017, **40**, 88-94.

[62] J. Ying, J. Li, G. Jiang, Z. P. Cano, Z. Ma, C. Zhong, D. Su, Z. Chen, Appl. Catal. B, 2018, **225**, 496-503.

[63] Z. Li, J. Liu, C. Xia, F. Li, ACS Catal., 2013, **3**, 2440-2448.

[64] F. Wang, J. Xu, X. Shao, X. Su, Y. Huang, T. Zhang, ChemSusChem, 2016, **9**, 246-251.

[65] W. Wang, W. Jing, L. Sheng, D. Chai, Y. Kang, Z. Lei, Appl. Catal. A, 2017, **538**, 123-130.

[66] G. H. Wang, Z. Cao, D. Gu, N. Pfänder, A. C. Swertz, B. Spliethoff, H. J. Bongard, C. Weidenthaler, W. Schmidt, R. Rinaldi, F. Schüth, Angew. Chem. Int. Ed., 2016, **55**, 8850-8855.

[67] J. Y. Chen, Q. J. Niu, G. K. Chen, J. Nie, G. P. Ma, J. Phys. Chem. C, 2017, **121**, 1463-1471.

[68] T. Maiyalagan, T. O. Alaje, K. Scott, J. Phys. Chem. C, 2012, **116**, 2630-2638.

[69] A. J. Bard, L. R. Faulkner, Electrochemical methods: Fundamentals and applications, 2nd ed., Wiley, New York, 2001.

[70] H.-B. Noh, P. Chandra, Y.-J. Kim, Y.-B. Shim, Anal. Chem., 2012, **84**, 9738-9744.

[71] K. A. Rawat, J. R. Bhamore, R. K. Singhal, S. K. Kailasa, Biosens. Bioelectron., 2017, **88**, 71-77.

[72] G. Lai, H. Zhang, A. Yu, H. Ju, Biosens. Bioelectron., 2015, **74**, 660-665.

[73] M. Brownlee, Nature, 2001, **414**, 813-820.

[74] P. Zimmet, K. G. M. M. Alberti, J. Shaw, Nature, 2001, **414**, 782-787.

[75] H. Zhu, L. Li, W. Zhou, Z. Shao, X. Chen, J. Mater. Chem. B, 2016, **4**, 7333-7349.

[76] U. Schwedes, M. Siebolds, G. Mertes, Diabetes Care, 2002, **25**, 1928-1932.

[77] J. Wang, Chem. Rev. 2008, 108, 814-825.

[78] H. Lee, Y. J. Hong, S. Baik, T. Hyeon, D.-H. Kim, Adv. Healthcare Mater., 2018, **7**, 1701150.

[79] A. S. Nugraha, C. Li, J. Bo, M. Iqbal, S. M. Alshehri, T. Ahamad, V. Malgras, Y. Yamauchi, T. Asahi, ChemElectroChem, 2017, **4**, 2571-2576.

[80] Y. Song, C. Zhu, H. Li, D. Dua, Y. Lin, RSC Adv., 2015, **5**, 82617-82622.

[81] K. Shim, W.-C. Lee, M.-S. Park, M. Shahabuddin, Y. Yamauchi, M. S. A. Hossain, Y.-B. Shim, J. H. Kim, Sens. Actuators B Chem., 2019, **278**, 88-96.

[82] K. Tian, M. Prestgard, A. Tiwari, Mater. Sci. Eng. C, 2014, **41,** 100-118.

[83] X. Yu, Y. Zhang, L. Guo, L. Wang, Nanoscale, 2014, **6**, 4806-4811.

[84] X. Bo, J. Bai, L. Yang, L. Guo, Sens. Actuators B Chem., 2011, **157**, 662-668.

[85] D.A. Vattem, R. Randhir, K. Shetty, Process Biochem., 2005, **40**, 2225-2238.

[86] G. R. Velderrain-Rodríguez, H. Palafox-Carlos, A. Wall-Medrano, J. F. Ayala-Zavala, C-Y. O. Chen, M. Robles-Sánchez, H. Astiazaran-García, E. Alvarez-Parrilla, G. A. Gonzalez-Aguilar, Food Funct., 2014, **5**, 189-197.

[87] H. Chen, J. Yao, F. Wang, Y. Zhou, K. Chen, R. Zhuang, M. M.F. Choi, G. Zaray, Sci. Total Environ., 2010, **408**, 1043-1049.

[88] H. Yin, L. Cui, S. Ai, H. Fan, L. Zhu, Electrochim. Acta, 2010, **55**, 603-610.

[89] H. Yoshida, H. Harada, H. Nohta, M. Yamaguchi, Anal. Chim. Acta, 2013, **488**, 211-221.

[90] L. N. Vanderberg, R. Hauser, N. Marcus, W. V. Welshons, Reprod. Toxicol. 2007, **24**, 139-177.

[91] H. Mielke, U. Gundert-Remy, Toxicol. Lett., 2009, **190**, 32-40.

[92] K. Shim, Z.-L. Wang, T. H. Mou, Y. Bando, A. A. Alshehri, J. Kim, M. S. A. Hossain, Y. Yamauchi, J. H. Kim, ChemPlusChem, 2018, **83**, 401-406.

[93] R. Zhang, Y. Zhang, X. Deng, S. Sun, Y. Li, Electrochim. Acta, 2018, **274**, 417-424.

[94] X. Yan, C. Zhou, Y. Yan, Y. Zhu, Electroanalysis, 2015, **27**, 2718-2724.

[95] R. Wannapob, P. Thavarungkul, S. Dawan, A. Numnuam, W. Limbut, P. Kanatharana, Electroanalysis, 2017, **29**, 472-480.

[96] K.-J. Huang, Y.-J. Liu, Y.-M. Liu, L.-L. Wanga, J. Hazard. Mater., 2014, **276**, 207-215.

[97] Y.-C. Wang, D. Cokeliler, S. Gunasekaran, Electroanalysis, 2015, **27**, 2527-2536.

[98] D. Zhao, G. Yu, K. Tian, C. Xu, Biosens. Bioelectron., 2016, **82**, 119-126.

[99] S.-j. Kim, Y. K. Cho, C. Lee, M. H. Kim, Y. Lee, Biosens. Bioelectron., 2016, **77**, 1144-1152.

[100] S. Sansuk, E. Bitziou, M. B. Joseph, J. A. Covington, M. G. Boutelle, P. R. Unwin, J. V. Macpherson, Anal. Chem., 2013, **85**, 163-169.

[101] Y. Li, H. Song, L. Zhang, P. Zuo, B.-c. Ye, J. Yao, W. Chen, Biosens. Bioelectron., 2016, **78**, 308-314.

[102] Q. Zhua, J. Bao, D. Huo, M. Yang, C. Hou, J. Guo, M. Chen, H. Fa, X. Luo, Y. Ma, Sens. Actuators B Chem., 2017, **238**, 1316-1323.

[103] J. Huang, Y. Liu, H. Hou, T. You, Biosens. Bioelectron., 2008, **24**, 632-637.

[104] W. A. El-Said, J.-H. Lee, B.-K. Oh, J.-W. Choi, Electrochem. Commun., 2010, **12**, 1756-1759.

[105] L.-X. Chen, J.-N. Zheng, A.-J. Wang, L.-J. Wu, J.-R. Chen, J.-J. Feng, Analyst, 2015, **140**, 3183-3192.

[106] A. A. Abdelwahab, Y.-B. Shim, Sens. Actuators B Chem., 2015, **221**, 659-665.

[107] Y. Huang, Y.-E Miao, S. Ji, W. W. Tjiu, T. Liu, ACS Appl. Mater. Interfaces, 2014, **6**, 12449-12456.

[108] C. Zou, J. Zhong, J Wang, Y. Shiraishi, S. Li, B. Yan, J. Guo, Y. Du, RSC Adv., 2016, **6**, 92502-92509.

[109] K. Zhang, X. Chen, Z. Li, Y. Wang, S. Sun, L. Wang, T. Guo, D. Zhang, Z. Xue, X. Zhou, X. Lu, Talanta, 2018, **178**, 315-323.

[110] X. Mei, Q. Wei, H. Long, Z. Yu, Z. Deng, L. Meng, J. Wang, J. Luo, C.-T. Lin, L. Ma, K. Zheng, N. Hu, Electrochim. Acta, 2018, **271**, 84-91.

3. Experimental

3.1 Overview

In this doctoral work, two methods, including soft and sacrificial templates, were adopted to synthesise noble metal based NPs and composites. After preparing the nanomaterials, wide- and low-angle X-ray diffraction (XRD), field emission scanning electron microscopy (FESEM), transmission electron microscopy (TEM), energy dispersive X-ray spectroscopy (EDS), Raman spectroscopy, the Brunauer-Emmett-Teller (BET) surface area analysis technique, and X-ray photoelectron spectroscopy (XPS) were used for characterization of samples. To analyse the electrochemical properties of the materials and sensing performance, cyclic voltammetry, chronoamperometry, and electrochemical impedance spectroscopy (EIS) were employed. Finally, these prepared materials were used as electrodes for glucose and bisphenol A sensors. The logical flow of the experimental route along with the characterizations is shown in Figure 3.1 below.

3.2 Materials and chemicals

The list of materials and chemicals used in this studyis presented in Table 3.1.

Table 3.1. Description of chemicals and materials used in this doctoral work.

Materials/Chemicals	Formula	Purity (%)	Supplier
Potassium tetrachloroplatinate(II)	K_2PtCl_4	98 %	Sigma–Aldrich, Australia
Brij 58® (polyethylene glycol hexadecyl ether)	$HO(CH_2CH_2O)_{20}C_{16}H_{33}$	N/A	Sigma–Aldrich, Australia
L-ascorbic acid	$C_6H_8O_6$	N/A	Sigma–Aldrich, Australia

Bisphenol A (2,2-Bis(4-hydroxyphenyl)propane)	$(CH_3)_2C(C_6H_4OH)_2$	≥99 %	Sigma–Aldrich, Australia
Poly(ethyleneimine) Solution		50 % (w/v) in H_2O	Sigma–Aldrich, Australia
Acetaminophen	$CH_3CONHC_6H_4OH$	N/A	Sigma–Aldrich, Australia
Dopamine hydrochloride	$(HO)_2C_6H_3CH_2CH_2NH_2 \cdot HCl$	N/A	Sigma–Aldrich, Australia
Uric acid	$C_5H_4N_4O_3$	N/A	Sigma–Aldrich, Australia
Phosphatidylcholine		N/A	Avanti Polar Lipids, Inc., USA
Sodium phosphate monobasic	NaH_2PO_4	N/A	Sigma–Aldrich, Australia
Sodium phosphate dibasic	Na_2HPO_4	N/A	Sigma–Aldrich, Australia
Gold(III) chloride trihydrate	$HAuCl_4 \cdot 3H_2O$	≥99.9 %	Sigma–Aldrich, Australia
D-(+)-glucose	$C_6H_{12}O_6$	≥99.5 %	Sigma–Aldrich, Australia
Nafion®			Sigma–Aldrich, Australia
Sodium chloride	NaCl	≥99 %	Sigma–Aldrich, Australia
Sulfuric acid	H_2SO_4	95 ~ 98 %	Sigma–Aldrich, Australia
Sodium tetrachloropalladate(II)	Na_2PdCl_4	98 %	Sigma–Aldrich, Australia

Chloroplatinic acid hexahydrate	$H_2PtCl_6 \cdot 6H_2O$	≥37.50 % Pt basis	Sigma–Aldrich, Australia
Pluronic® F-127		N/A	Sigma–Aldrich, Australia
Aniline	$C_6H_5NH_2$	JIS Special Grade	Wako Pure Chemical Industries, Ltd. , Japan
Nitric acid	HNO_3	JIS Special Grade	Wako Pure Chemical Industries, Ltd. , Japan
Carbon paper			Toray, Japan

3.3 Materials preparation

Materials preparation and synthesis were conducted by using soft templates and electrochemical methods. All methods will be explained in detail in each chapter.

3.4 Physical and morphological characterization techniques

The physical and morphological characterization techniques used to characterize the synthesized material are briefly discussed in this section.

3.4.1 X-ray powder diffraction (XRD)

X-ray powder diffraction (XRD) is a fast analytical technique that is mainly used for phase identification of unknown crystalline materials and can provide information about the unit cell dimensions. Since all crystals are characterized by a unique *d*-spacing, the pattern is functionally related to the crystal structure described by Bragg's law (Equation 3.1).

$$n\lambda = 2d \sin\theta \quad (3.1)$$

In this thesis, GBC MMA diffractometer with Cu Kα radiation (λ = 1.5406 Å) at the University of Wollongong was employed to conduct X-ray powder diffraction.

3.4.2 Brunauer-Emmett-Teller (BET) Analysis

Brunauer-Emmett-Teller (BET) analysis is a technique fpr evaluating the specific surface area and pore size distribution of sample materials using adsorption and desorption techniques. The aim of BET theory is to explain the gas adsorption on the surfaces of solid-state materials. BET analysis is performed at liquid nitrogen temperature (77 K) at various relative pressures. In this thesis, a Belsorp-mini II instrument were used for BET measurements.

3.4.3 X-Ray Photoelectron Spectroscopy (XPS)

X-ray photoelectron spectroscopy (XPS) is a surface sensitive quantitative spectroscopy method that is used to analyze the element composition including an element's chemical and electronic states. The XPS spectrum is obtained by simultaneously measuring the number of electrons and the kinetic energy, which have exited from depths of 0 to 10 nm from the surface of the material. The ratio of valences and valence states of an element can be determined by the characteristic binding energy associated with the electrons in their orbitals. In this thesis work, XPS was conducted on ESCALAB 250 and VG Scientific ESCALAB 2201XL instruments.

3.4.4 Scanning electron microscopy (SEM)

The scanning electron microscope is one type of electron microscope, which scans the surface of materials with a focused beam to produce images. Electrons and atoms of the sample interact with each other to generate information on the surface topography and composition of the sample. The surface topography and composition of the sample are

obtained from various signals including secondary electrons (SE), back-scattered electrons (BSE), characteristic X-rays, specimen currents under illumination, and transmitted electrons. In this thesis, the morphology and structure of the samples were studied with a field-emission scanning electron microscope (JEOL 7500 and Hitachi SU-8000).

3.4.5 Transmission electron microscopy (TEM)

Transmission electron microscopy (TEM) is one of microscopy techniques that is used to obtain various types of information including on the morphology and crystal structure of a sample. This technique is generally used to characterize nanoscale materials down to atomic resolution. In the TEM, the electron beam passes through the ultra-thin sample and reaches the imaging lens and detector. The TEM images are formed by the interaction between the electrons and the sample when the electron beam passes through the ultra-thin sample. In this doctoral work, the TEM images of the samples were collected on a JEOL 2010, JEOL 2100 and HITACHI H-7600.

3.5 Electrochemical characterizations techniques

3.5.1 Cyclic voltammetry

Cyclic voltammetry (CV) is one kind of potentiodynamic electrochemical technique. This technique is commonly used to confirm the electrochemical characteristics of molecules adsorbed onto the electrode. CV is performed by recording the response current when cycling the potential of the working electrode at the specified scan speed. In this thesis, the CV curves were obtained on a potentiostat/galvanostat (Ivium and Kosentech).

3.5.2 Amperometry

Amperometry is one kind of electrochemical technique. This technique involves the detection of ions in solution based on the electric current or changes in electric current. The simplest forms of amperometric measurement are single potential or direct current (DC) amperometry. The potential is applied between the two electrodes located in the column effluent and the measured current changes as the electroactive analyte is oxidized at the anode or reduced at the cathode. In this doctoral work, the CA graphs were obtained on a potentiostat/galvanostat (Ivium and Kosentech).

4. Synthesis and cytotoxicity of dendritic platinum nanoparticles with HEK-293 cells

4.1 Introduction

Since the reports on mesoporous nanoparticles (NPs) in the early 90s [1,2]. various nano-architectures of porous NPs have gained attention in both industry and academia, because of their high surface area, tunable pore size, and uniform/narrow pore size distribution. Owing to these controllable properties, mesoporous or nanoporous NPs have been in high demand and they were designed for various applications, such as energy storage [3,4], catalysis [5,6], and biomedical applications [7,8]. There are two key approaches to obtain mesoporous NPs. One is the soft-templates method, in which various mesoporous structures (e.g., two-dimensional (2D) hexagonal structure, cubic structure, etc.) with the desired shapes (e.g., films, rods, tubes, NPs, etc.) are created by the self-assembly of micelles [9]. The other is the hard-templates method, in which the targeted NPs are deposited into the confined spaces of a template with the desired morphology [10,11]. Soft-templates in particular is a very simple approach using low-molecular-weight (e.g., P-123, F-127, Brij58) and high-molecular-weight (e.g., triblock copolymers) amphiphilic molecules as pore-directing agents.

Recently, platinum (Pt) NPs have been widely used in catalysis (e.g., methanol oxidation reaction [12-17], electrochemical oxidation of ethanol [18,19], oxygen reduction reaction [14,20-22], etc. [23,14]), sensors (e.g., glucose [16,24], methanol [25]), and biomedical applications (e.g., cancer therapy [26,27]) owing to their high catalytic activity and good biocompatibility. Investigations on surfactant-mediated syntheses of dendritic Pt nanoparticles (DPNs) with nanoporous architectures have been reported [28-

31]. It is of high interest to expand the applicability of Pt NPs over multiple fields, therefore, through our study, we aimed to achieve an enhanced performance for biomedical applications using size-controlled DPNs, prepared with an amphiphilic molecular surfactant and a sonochemical method.

NPs for biomedical applications have shown enormous potential in recent years as therapeutic mediators for many diseases, including cancer [32-34]. One of the major limitations, however, in using metallic NPs, is their nonspecific untargeted toxicity. To apply our DPNs in biomedical fields, it is necessary to understand various processes induced by these NPs in human tissues and genetic material to further improve their sensitizing properties. Hence, for any new material being developed for therapeutic purposes, the determination of its toxicity to human tissues is highly important. Furthermore, using metal NPs with a thermal method is one of the other important applications for cancer therapy. Since the optical properties of the NPs in the infrared range have provided a pathway for the development of new techniques, cancer therapy using NPs along with the photothermal treatment has become more effective, which is one reason why we are interested in exploring the cytotoxicity of DPNs.

Amphiphilic molecules (non-ionic surfactants) have been used to prepare DPNs (Figure 4.1a) using a sonication process for rapid synthesis and tuning the kinetics of the reaction. The mesoporous Pt NPs were characterized via transmission electron microscopy (TEM), X-ray diffraction (XRD), small angle X-ray scattering (SAXS), ultraviolet/visible (UV/Vis) spectroscopy and the Brunauer–Emmett–Teller (BET) theory.

4.2 Experimentals

Chemicals: Potassium tetrachloroplatinate(II) (K_2PtCl_4, 98%), polyethylene glycol hexadecyl ether (Brij 58, $HO(CH_2CH_2O)_{20}C_{16}H_{33}$), and l-ascorbic acid (AA, $C_6H_8O_6$, reagent grade) were purchased from Sigma–Aldrich and used without further purification.

Characterizations: Detailed microstructures were examined using a JEOL-2100 or a JEOL-2010 transmission electron microscope (TEM). Wide-angle powder X-ray diffraction (XRD) patterns were obtained using a GBC MMA XRD at a scanning rate of $2° \text{ min}^{-1}$. Small-angle XRD patterns were collected by using NANO VIEWER equipment with a Micro Max-007 HF high-intensity micro-focus rotating-anode X-ray generator. UV/Vis data was collected on a Shimadzu UV-3600 spectrophotometer. Nitrogen adsorption-desorption data were recorded using a Belsorp-mini II instrument.

Cytotoxicity test: The cultures of HEK-293 human embryonic kidney cells were started with approximately 100000 cells mL^{-1} in 10% fetal bovine serum (FBS)-supplemented Dulbecco's Modified Eagle's Medium (DMEM) in a 24-well microtiter plate. The cultures were then added at different concentrations of platinum NPs, ranging from 15 to 45 $\mu g \text{ mL}^{-1}$, keeping one blank for reference. The cultures were then incubated for 24 h or 48 h in an incubator with 5% CO2 and 95% humidified atmosphere. The cells were removed from the culture by trypsinization after incubation and washed 2 times with Dulbecco's phosphate buffered saline (PBS; pH: 7.4) to remove any presence of serum that could interfere with the staining. The cells were then re-suspended in PBS, and aliquots of 20 µL were made from all the different cultures. Equal amounts (v/v) of pre-filtered 0.4% trypan blue stain were added to the aliquots, and the solutions were allowed to settle for 1 min. The samples were then observed under an inverted microscope in a Fuchs-Rosenthal hemocytometer to determine the cell viability.

4.3 Results and discussions

For the synthesis of DPNs, we prepared two different vessels containing 5 mL of each sample for 20 mM K_2PtCl_4 aq solution, 1 mL of 50 mg Brij 58 aq solution and 5 mL of 0.1 mL ascorbic acid (AA) aq solution, and each solution was kept at room temperature (20 ^oC) and at 60 ^oC. Both the K_2PtCl_4 and Brij 58 solutions were then mixed in another vessel and, subsequently, the AA aqueous solution was placed in 20 ^oC and 60 ^oC baths,

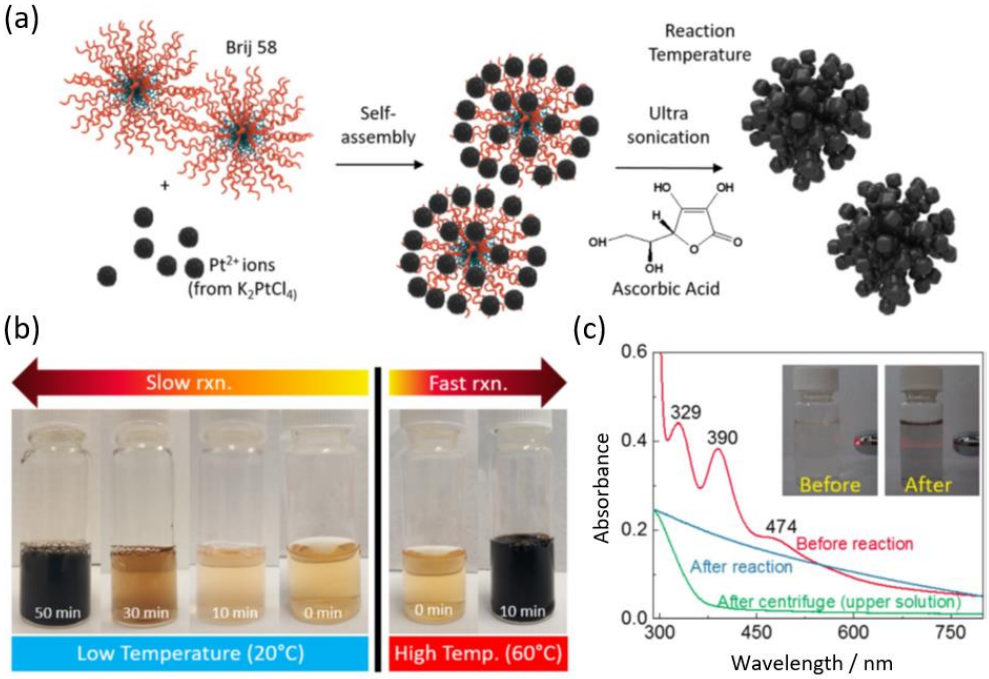

Figure 4.1. (a) Schematic illustration of the synthesis of DPNs. (b) Photographs of the color change during synthesis (room temperature (20 ℃), 60 ℃). (c) UV/Vis spectra before reaction (red), after reaction (blue) and after centrifuge (upper solution). Inset: the Tyndall effect on DPN suspension in solution.

respectively, for chemical reduction. The two mixed solutions were reacted at room temperature (20 ^oC) and 60 ^oC, respectively, for 10 to 50 min with thorough ultra-sonication (220-240 V, 50-60 Hz). After the reactions, the precipitates were collected by centrifugation and washed several times with deionized (DI) water to remove the surfactant and excess reactants.

Different shapes and sizes of DPNs were obtained at 20 °C and 60 °C, which confirmed the temperature effect. It seems that the DPNs synthesized at 60 °C were denser than those synthesized at 20 °C (Figure 4.2). The reduction time for the Pt complexes ($[PtCl_4]^{2-}$) was decreased by increasing the reaction temperature. When the $[PtCl_4]^{2-}$ was reduced at 20 °C with AA, the size of the obtained Pt particles was estimated to be 23 nm (Figure 4.2a–d), and the color of the solution had changed completely over 50 min (Figure 4.1b). When $[PtCl_4]^{2-}$ reacted at 60 °C with AA, however, the solution turned black within

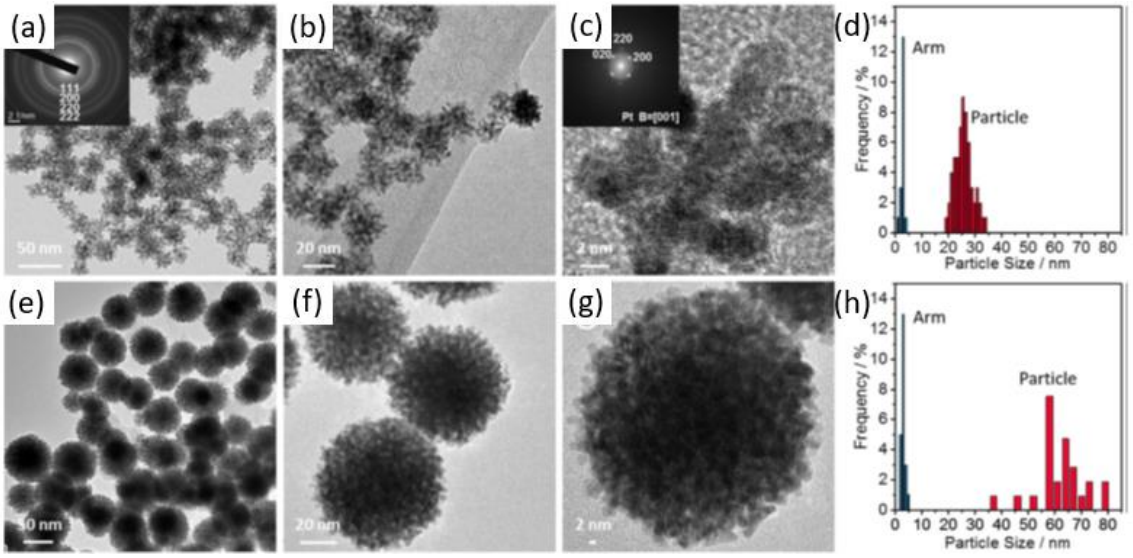

Figure 4.2. TEM images of DPNs obtained at 20 ℃ (a–c) and 60 ℃ (e–g): Corresponding SAED (inset of (a)) and FFT pattern (inset of (c)). (d, h) The particle and arm size distributions of DPNs obtained at different temperatures (20 ℃ (d) and 60 ℃ (h))

10 min (Figure 4.1b), and the Pt particle size was found to be around 60 nm (Figure 4.2e–h). This means that the reduction of $[PtCl_4]^{2-}$ is strongly affected by the reaction temperature. A higher reduction temperature might enhance the diffusivity of Pt ions, resulting in larger Pt particles in a short time. Considering our purpose for bioapplications, we used the smaller Pt particles for further investigations.

The reaction of the Pt precursors was investigated through UV/Vis spectroscopy (Figure 4.1c), AA being used as a reducing agent. Before the formation of DPNs,

absorption bands corresponding to the Pt complexes were clearly detected at 329 nm, 390 nm and 474 nm, respectively. After the reaction, these three peaks completely disappeared, indicating that the Pt ions were changed from Pt^{2+} to Pt^{0} owing to their reduction by AA ($C_6H_8O_6 + Pt^{2+} \rightarrow C_6H_6O_6 + Pt^{0} + 2H^{+}$) during synthesis [35,36]. Thus, the $[PtCl_4]^{2-}$ reduction can be achieved by using ascorbic acid via sonication. During the reaction, the Tyndall effect showing the presence of NPs in the solution was observed through light scattering effect [37]. The yield of this reaction was approximately 98 %.

The shape, size and crystalline structure of DPNs were confirmed by TEM at 20 ^{o}C and 60 ^{o}C (Figure 4.2). We found that the average diameter of the obtained Pt at 20 ^{o}C and 60 ^{o}C were approximately 23 nm and 60 nm, respectively, with a narrow size distribution (Figure 4.2d and h), with the Pt particles being welldispersed without agglomeration. The selected area diffraction (SAED) pattern further confirmed the nature of the face-centered-cubic (fcc) crystal structure with concentric rings from the (111),

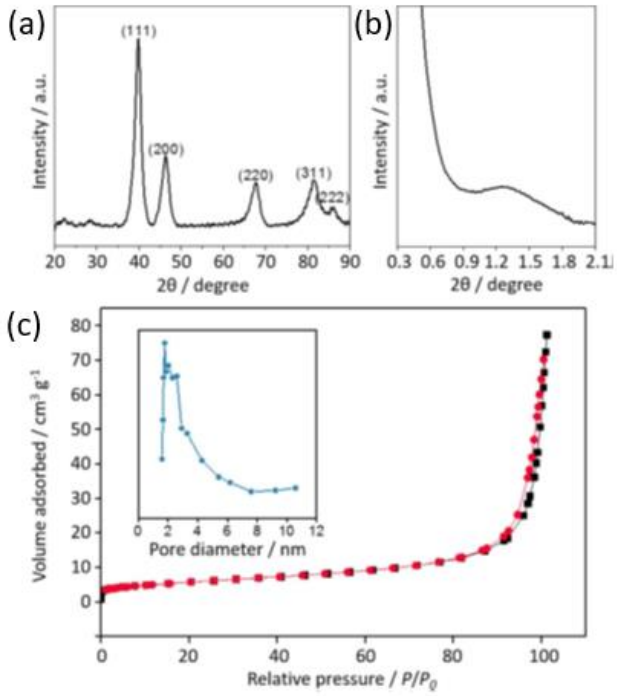

Figure 4.3. Characterization of DPNs: (a) wide-angle XRD, (b) low-angle XRD, and (c) N_2 adsorption-desorption isotherm; inset: pore size distribution by the Barrett-Joyner-Halenda (BJH) method.

(200), (220) and (222) planes (inset, Figure 4.2a). A high-resolution TEM (HRTEM) image of one Pt particle and the corresponding fast Fourier transform (FFT) were further examined (inset, Figure 4.2c), and they were in good agreement with the Pt single crystal. The lattice fringes were clearly observed. Interestingly, the DPNs prepared at 20 ^{o}C and 60 ^{o}C consisted of nanosized arms of 2–4 nm in the same width (Figure 4.2d and h). Each arm had grown as a faceted single crystal, and they were all interconnected. For this reason, some spaces were observed between the nanosized arms.

The degree of crystallinity of Pt was further investigated by wide-angle XRD

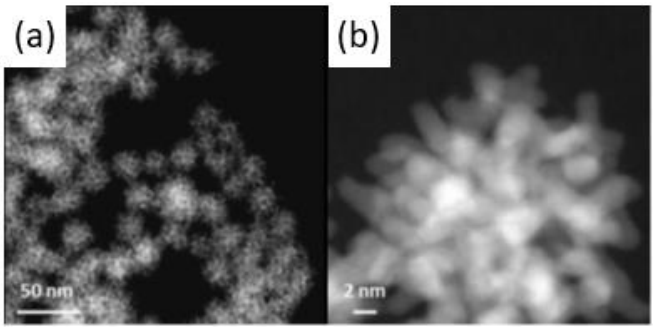

Figure 4.4. TEM images of DPNs obtained at room temperature (20℃).

measurement. The pattern of the DPNs showed several peaks from the (111), (200), (220), (311) and (222) planes (Figure 4.3a), which were assigned to the fcc crystal structure. This pattern was consistent with the SAED pattern shown in Figure 4.2a. Low-angle XRD was carried out to further examine the periodicity of nanospace created between the arms. One broad diffraction peak at around 1.258 (d=7.1 nm) was clearly observed, which is typical for disordered mesoporous NPs (Figure 4.3b). This value corresponds to the pore-to-pore distance. The porosity was studied by N_2 adsorption-desorption isotherms (Figure 4.3c). From the Barrett-Joyner-Halenda (BJH) method, an average mesopore diameter of 2-4 nm was obtained for the Pt particles. These results were consistent with TEM

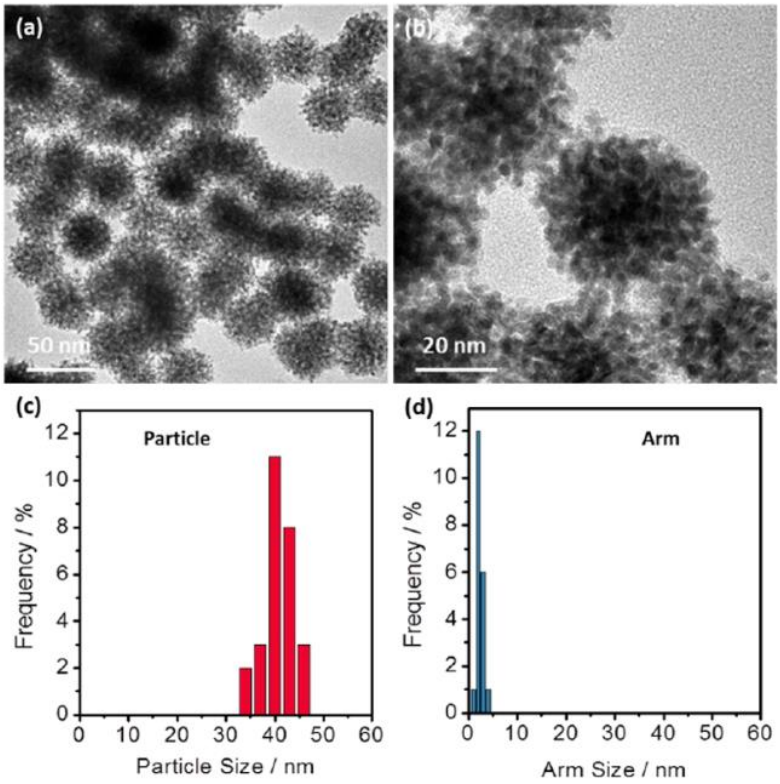

Figure 4.5. (a, b) TEM images of DPNs obtained at room temperature (20℃) with stirring. (c) The particle size distribution. (d) The arm size distribution.

observations and were indicative of their porous structure containing mesopores (Figure 4.4). The specific surface area obtained by the Brunauer- Emmett-Teller (BET) method was approximately 47 $m^2 g^{-1}$. According to the literature, other related nanostructured Pt particles normally had smaller surface areas in the range of 18 to 30 $m^2 g^{-1}$ [38]. Compared to these results, our Pt NPs had a relatively high surface area, which would be expected to contain more catalytic sites.

To further investigate the effect of sonication, we used a stirring method during the synthesis of DPNs at 20 ^oC and 60 ^oC, respectively. As a result, the average diameter of DPNs synthesized at 20 ^oC increased from 23 nm to 40 nm (Figure 4.5), while the size of DPNs synthesized at 60 ^oC decreased slightly from 60 nm to 55 nm (Figure 4.6) compared to the sonochemical method. In addition, we could confirm that sonication at 20 and 60 ^oC showed narrower size distributions of DPNs than those from the reaction without

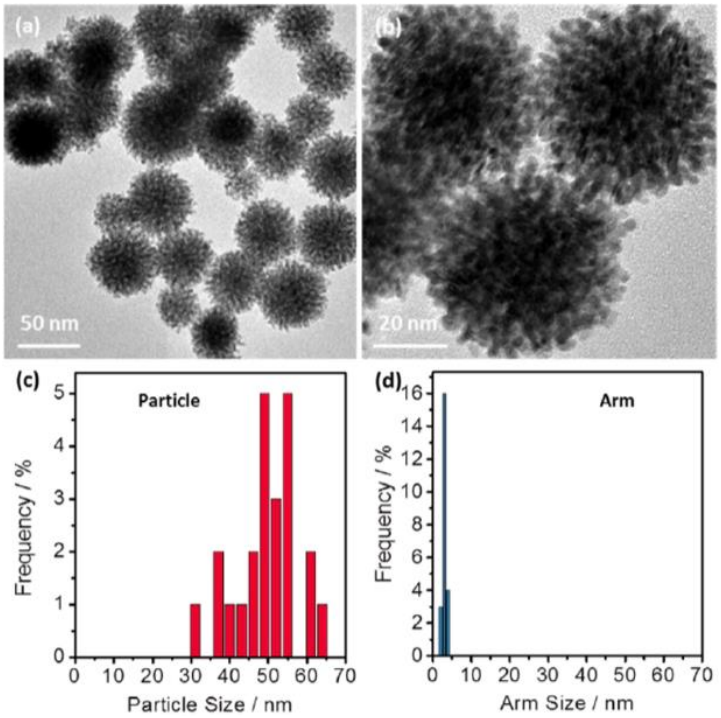

Figure 4.6. (a, b) TEM images of DPNs obtained at 60 ℃ with stirring. (c) The particle size distribution. (d) The arm size distribution.

sonication with stirring (Figure 4.5 and 4.6). Moreover, the reaction time of DPNs using

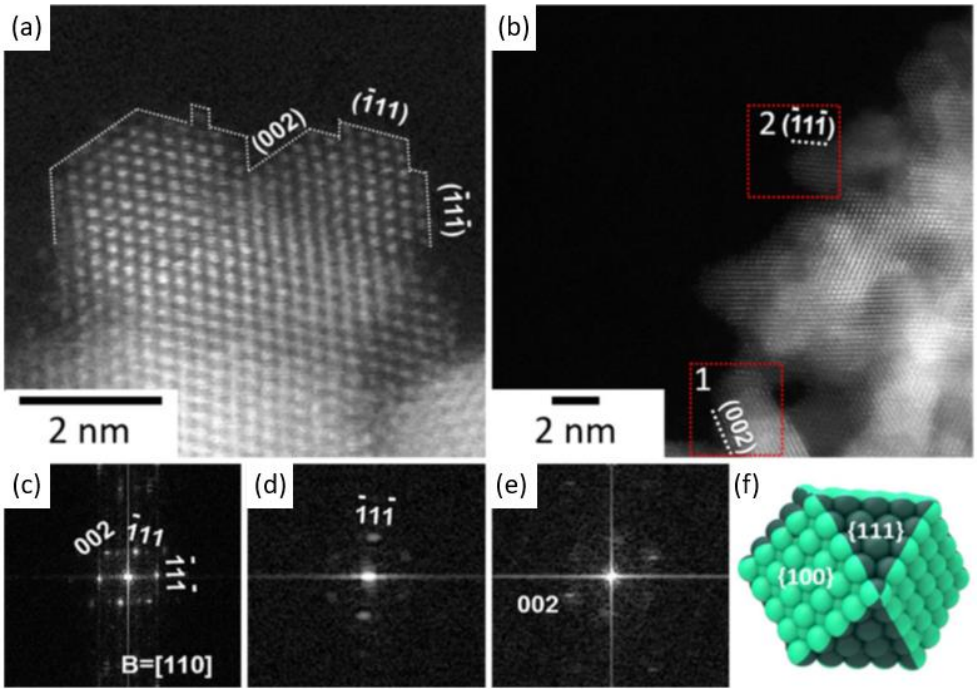

Figure 4.7. HAADF-STEM study of DPNs: (a) high magnification image in [110] beam direction, (b) low magnification image under off-axis conditions, (c) FFT pattern of (a). (d, e) FFT patterns at positions 1 and 2 of (b). (f) Structure of single crystal Pt nanoparticle. {111} and {100} facets were still observed under off axis conditions, which implied that both planes were facet planes.

sonication was shorter. A previous study confirmed a similar process [39]. These results showed that the reaction conditions affected the particle size with controllability, although the arm width had been almost constant.

To gain a better understanding, we needed in-depth studies on the grain growth mechanism of Pt. Controlling the facets would be highly desirable, because these determine the physicochemical properties and other properties of the NPs. {111} and {200} facet planes were observed at various beam orientations (Figure 4.7a–b) with FFT

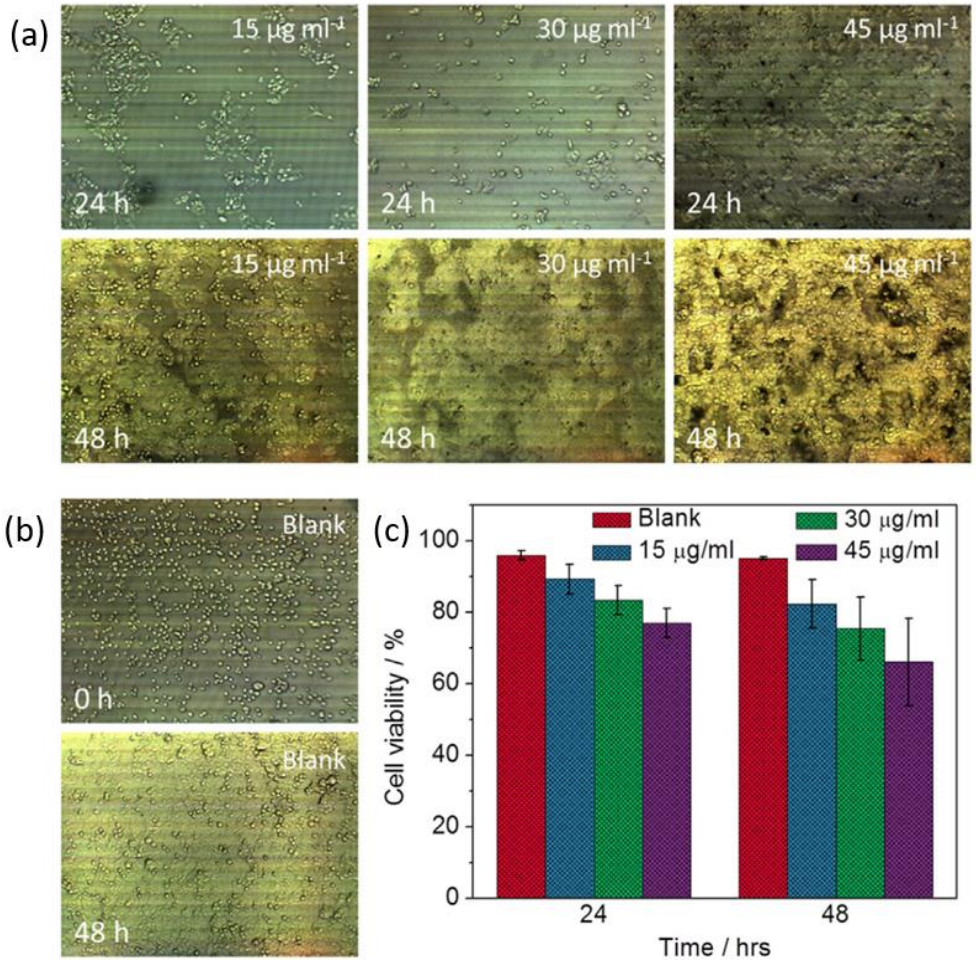

Figure 4.8. (a) Images of cells in culture at different concentrations of DPNs. (b) Images of cells in culture at 0 h and 48 h without Pt nanoparticles. Blank culture with no nanoparticles added subjected to trypan blue staining method showed 95.55% viability. (c) Cell viability test of DPNs from HEK-293 cells according to different concentrations.

patterns (Figure 4.7c–e). In the larger DPNs synthesized at 60 ^{o}C (Figure 4.8), the same crystalline facets were observed. According to the literature, the most dominant facets of the Pt structure are {111} and {100} facets, which has been proved by our Pt particles (Figure 4.7f). Our TEM observation showed that the {110} facet does not exist and the {111} exists as the predominant facet in the Pt crystal. This is probably because the {111} surface energy is much lower than those of the {100} and {110} facets [40–42].

For the purposes of using these DPNs in biomedical applications, we examined their cytotoxic effects on normal human cells (Figure 4.8). After incubating the cells with the DPNs, the cells showed different viability depending on the concentration of the NPs and the incubation time. As the concentration of the NPs increased, the cell viability decreased, suggesting a dose-dependent cytotoxicity. Similarly, when the cells were incubated for an extended period of time, the number of viable cells in the cell media decreased, indicating the proliferation of cells was affected by DPNs. Microscopic observations showed no noticeable change in the shape and size of the cells from the 15 and 30 μg mL^{-1} concentration samples, and they appeared almost identical to those from the blank culture, whereas the culture containing 45 μg mL^{-1} DPNs showed a dark colored coating of platinum NPs on the cells. As shown in Figure 4.8a, after incubation for 48 h, all of the

Table 4.1. The cell viability after incubation with Pt nanoparticles in comparison with other reports.

Cell	Incubation Time (h)	Particles	Pt concentration	Cell viability (%)	Ref.
HEK-293	24	Mesoporous Pt nanoparticles (23 nm)	0–45 μg/ml	77–96	This work
HEK-293	48	Mesoporous Pt nanoparticles (23 nm)	0–45 μg/ml	66–95	This work
BT-20	24	Dendritic Pt nanoparticles (20 nm)	0–100 μg/ml	80–98	45
MCF-7	24	Pt nanoparticles (34 nm)	1–8 μg/ml	46–87	33
HepG-2	24	Pt nanoparticles (34 nm)	1–8 μg/ml	8–96	33

HepG-2	48	Apoferritin-encapsulated Pt nanoparticles (AFt–Pt) (4.3 nm)	0–140 μg/ml	80–100	46
HepG-2	48	Polyvinylpyrrolidone stabilized Pt nanoparticles (PVP–Pt) (4.7 nm)	0–140 μg/ml	30–100	46
MCF-7	24	Ac-G9 dendrimer-encapsulated Pt NPs (10 nm)	1–30 nM	87–97	47
HeLa	24	Ac-G9 dendrimer-encapsulated Pt NPs (10 nm)	1–30 nM	85–98	47
NHEKs	24	Pt nanoparticles (5.8 nm)	0–25 μg/ml	88–100	48
NHEKs	24	Pt nanoparticles (57 nm)	0–25 μg/ml	83–100	48
NHEKs	48	Pt nanoparticles (5.8 nm)	0–25 μg/ml	82–100	48
NHEKs	48	Pt nanoparticles (57 nm)	0–25 μg/ml	75–100	48

cultures showed a dark and dense presence of platinum NPs. The cultures with 15 and 30 μg mL^{-1} of Pt NPs showed continuous growth of cells after 48 h along with a bulk aggregation of cells that could not be partly differentiated individually (Figure 4.8c). This might be due to the cytotoxic effects of the platinum NPs on the DNA of the cells [43,44]. When the concentration of DPNs increased to 45 μg mL^{-1}, we found that all cells aggregated and thus it was difficult to distinguish each cell, and such a cell agglomeration indicated cell death. The DPNs revealed comparable toxicity compared to that of the Pt NPs as shown in previous reports (Figure 4.8b and Table 4.1) [45-48].

4.4 Conclusions

In summary, we have synthesized uniform DPNs of a small size by using a sonochemical method. The obtained DPNs had a high surface area and narrow pore size distribution. In an HRTEM study, the synthesized DPNs exhibited fcc crystal structure with concentric rings representing the (111), (200), (220), and (222) planes in their SAED pattern. We confirmed the cytotoxicity of the DPNs, by studying their interaction with HEK-293 cells. These results showed potential for the use of these Pt NPs as a pathway

for various biomedical applications such as photothermal agents, drug vehicles, and biosensors.

4.5 References

[1] C. T. Kresge, M. E. Leonowicz, W. J. Roth, J. C. Vartuli, J. S. Beck, Nature, 1992, **359**, 710-712.

[2] J. S. Beck, J. C. Vartuli, W. J. Roth, M. E. Leonowicz, C. T. Kresge, K. D. Schmitt, C. T-W. Chi, D. H. Olson, E. W. Sheppard, S. B. McCullen, J. B. Higgins, J. L. Schlenkert, J. Am. Chem. Soc., 1992, **114**, 10834-10843.

[3] L. Shen, Q. Che, H. Li, X. Zhang, Adv. Funct. Mater., 2014, **24**, 2630-2637.

[4] S. Dong, X. Chen, L. Gu, X. Zhou, H. Xu, H. Wang, Z. Liu, P. Han, J. Yao, L. Wang, G. Cui, L. Chen, ACS Appl. Mater. Interfaces, 2011, **3**, 93-98.

[5] Y. Wang, J. Zhang, X. Wang, M. Antonietti, H. Li, Angew. Chem. Int. Ed., **2010**, 49, 3356-3359; Angew. Chem., 2010, **122**, 3428-3431.

[6] Z.-R. Tian, W. Tong, J.-Y. Wang, N.-G. Duan, V. V. Krishnan, S. L. Suib, Science, 1997, **276**, 926-930.

[7] I. I. Slowing, B. G. Trewyn, S. Giri, V. S.-Y. Lin, Adv. Funct. Mater., 2007, **17**, 1225-1236.

[8] J. Kim, H. S. Kim, N. Lee, T. Kim, H. Kim, T. Yu, I. C. Song, W. K. Moon, T. Hyeon, Angew. Chem. Int. Ed., 2008, **47**, 8438-8441; Angew. Chem., 2008, **120**, 8566-8569.

[9] Y. Shi, Y. Wan, D. Zhao, Chem. Soc. Rev., 2011, **40**, 3854-3878.

[10] V. Malgras, H. Ataee-Esfahani, H. Wang, B. Jiang, C. Li, K. C.-W. Wu, J. H. Kim, Y. Yamauchi, Adv. Mater., 2016, **28**, 993-1010.

[11] Y. Deng, J. Wei, Z. Sun, D. Zhao, Chem. Soc. Rev., 2013, **42**, 4054-4070.

[12] M. Rauber, I. Alber, S. Meller, R. Neumann, O. Picht, C. Roth, A. Schçkel, M. E. Toimil-Molares, W. Ensinger, Nano Lett., 2011, **11**, 2304-2310.

[13] S. M. Alia, G. Zhang, D. Kisailus, D. Li, S. Gu, K. Jensen, Y. Yan, Adv. Funct. Mater., 2010, **20**, 3742-3746.

[14] J. Zhang, K. Li, B. Zhang, Chem. Commun., 2015, **51**, 12012-12015.

[15] Y. Kuang, Y. Zhang, Z. Cai, G. Feng, Y. Jiang, C. Jin, J. Luo, X. Sun, Chem. Sci., 2015, **6**, 7122-7129.

[16] Q. Shen, L. Jiang, H. Zhang, Q. Min, W. Hou, J.-J. Zhu, J. Phys. Chem. C, 2008, **112**, 16385-16392.

[17] J. Wang, X.-B. Zhang, Z.-L. Wang, L.-M. Wang, W. Xing, X. Liu, Nanoscale, 2012, **4**, 1549-1552.

[18] X. Zhang, W. Lu, J. Da, H. Wang, D. Zhao, P. A. Webley, Chem. Commun., 2009, 195-197.

[19] S. Mourdikoudis, M. Chirea, T. Altantzis, I. Pastoriza-Santos, J. Pérez-Juste, F. Silva, S. Bals, L. M. Liz-Marzán, Nanoscale, 2013, **5**, 4776-4784.

[20] T. Yu, D. Y. Kim, H. Zhang, Y. Xia, Angew. Chem. Int. Ed., 2011, **50**, 2773-2777; Angew. Chem., 2011, **123**, 2825-2829.

[21] C. Wang, H. Daimon, T. Onodera, T. Koda, S. Sun, Angew. Chem. Int. Ed., 2008, **47**, 3588-3591; Angew. Chem., 2008, **120**, 3644-3647.

[22] G. Zhang, S. Sun, M. Cai, Y. Zhang, R. Li, X. Sun, Sci. Rep., 2013, **3**, 1526.

[23] A. Cuesta, G. Cabello, C. Guti8rrez, M. Osawa, Phys. Chem. Chem. Phys., 2011, **13**, 20091-20095.

[24] X. Niu, H. Zhao, C. Chen, M. Lan, ChemCatChem, 2013, **5**, 1416-1425.

[25] D.-S. Park, M.-S. Won, R. N. Goyal, Y.-B. Shim, Sens. Actuators B, 2012, **174**, 45-50.

[26] M. Manikandan, N. Hasan, H.-F. Wu, Biomaterials, 2013, **34**, 5833-5842.

[27] D. Chen, C. Zhao, J. Ye, Q. Li, X. Liu, M. Su, H. Jiang, C. Amatore, M. Selke, X. Wang, ACS Appl. Mater. Interfaces, 2015, **7**, 18163-18169.

[28] L. Wang, Y. Nemoto, Y. Yamauchi, J. Am. Chem. Soc., 2011, **133**, 9674-9677.

[29] L. Wang, Y. Yamauchi, J. Am. Chem. Soc., 2009, **131**, 9152-9153.

[30] L. Wang, Y. Yamauchi, J. Am. Chem. Soc., 2010, **132**, 13636-13638.

[31] L. Wang, Y. Yamauchi, J. Am. Chem. Soc., 2013, **135**, 16762-16765.

[32] P. V. Asharani, Y. Lianwu, Z. Gong, S. Valiyaveettil, Nanotoxicology, 2011, **5**, 43-54.

[33] H. Mohammadi, A. Abedi, A. Akbarzadeh, M. J. Mokhtari, H. E. Shahmabadi, M. R. Mehrabi, S. Javadian, M. Chiani, Int. Nano Lett., 2013, **3**, 28.

[34] J. Rajput, J. R. Moss, A. T. Hutton, D. T. Hendricks, C. E. Arendse, C. Imrie, J. Organomet. Chem., 2004, **689**, 1553-1568.

[35] C. Li, Y. Yamauchi, Phys. Chem. Chem. Phys., 2013, **15**, 3490-3496.

[36] L. Wang, C. Hu, Y. Nemoto, Y. Tateyama, Y. Yamauchi, Cryst. Growth Des., 2010, **10**, 3454-3460.

[37] J. W. Liaw, S.-W. Tsai, H.-H. Lin, T.-C. Yen, B.-R. Chen, J. Quant. Spectrosc. Radiat. Transfer, 2012, **113**, 2234-2242.

[38] H. Wang, M. Imura, V. Malgras, C. Li, L. Wang, Y. Yamauchi, J. Inorg. Organomet. Polym. Mater., 2015, **25**, 245-250.

[39] L. Wang, H. Wang, Y. Nemoto, Y. Yamauchi, Chem. Mater., 2010, **22**, 2835-2841.

[40] H. Akbarzadeh, H. Abroshan, G. A. Parsafar, Solid State Commun., 2010, **150**, 254-257.

[41] S. Sun, G. Zhang, D. Geng, Y. Chen, R. Li, M. Cai, X. Sun, Angew. Chem., 2011, **123**, 442-446.

[42] Y. Xia, Y. Xiong, B. Lim, S. E. Skrabalak, Angew. Chem. Int. Ed., **2009**, 48, 60-103; Angew. Chem., 2009, **121**, 62-108.

[43] E. Porcel, S. Liehn, H. Remita, N. Usami, K. Kobayashi, Y. Furusawa, C. L. Sech, S. Lacombe, Nanotechnology, 2010, **21**, 085103.

[44] J. Pelka, H. Gehrke, M. Esselen, M. Terk, M. Crone, S. Br-se, T. Muller, H. Blank, W. Send, V. Zibat, P. Brenner, R. Schneider, D. Gerthsen, D. Marko, Chem. Res. Toxicol., 2009, **22**, 649-659.

[45] C.-Y. Hong, Y. Yamauchi, K. C.-W. Wu, Chem. Lett., 2011, **40**, 408-409.

[46] X. Liu, W. Wei, C. Wang, H. Yue, D. Ma, C. Zhu, G. Ma, Y. Du, J. Mater. Chem., 2011, **21**, 7105-7110.

[47] X. Wang, Y. Zhang, T. Li, W. Tian, Q. Zhang, Y. Cheng, Langmuir, 2013, **29**, 5262-5270.

[48] P. Konieczny, A. G. Goralczyk, R. Szmyd, L. Skalniak, J. Koziel, F. L. Filon, M. Crosera, A. Cierniak, E. K. Zuba-Surma, J. Borowczyk, E. Laczna, J. Drukala, E. Pyza, D. Semik, O. Woznicka, A. Klein, J. Jura, Int. J. Nanomed., 2013, **8**, 3963-3975.

5. Efficient electrochemical bisphenol-A oxidation by self-supported dendritic platinum nanoparticles on screen-printed carbon electrode

5.1 Introduction

Over the past several decades, exposure to chemicals in the environment has been causing various problems for human health. Among the problem chemicals is bisphenol A (BPA, 2,2-bis(4-hydroxyphenyl) propane), which is one of the raw nanoparticles (NPs) used to produce the polycarbonate-based plastics and epoxy resins that are ubiquitous in our daily lives. For example, polycarbonate plastics are used for food containers, drink packaging, and medical devices. In addition, epoxy resins are used to coat metal products (e.g. food cans, bottle tops, etc.) [1,2]. Also, the threshold values are set for Bisphenol A in water sample by the European Chemicals Bureau, it has defined the predicted no effect concentration (PNEC) for BPA in freshwater is 1.5 μg L^{-1} and for marine water is 0.15 μg L^{-1} [3]. Even though BPA is an estrogenic environmental toxin that can lead to breast cancer, prostate cancer, birth defects, infertility, precocious development in girls, diabetes, and obesity [4,5], the most prevalent polycarbonate-based products still rely on BPA because of its cost-effectiveness. It is thus important to study methods for robust, selective, and sensitive BPA detection.

There have been various analytical methods for the detection of BPA, including separation analysis [6-8], fluorimetry [9,10], immunoassay [11-13], fluorescence [14], field-effect transistor [15], and laser direct writing [16]. These methods, however, demand sophisticated instruments, complex preparation of materials, tedious sample treatment, and long analysis time. Importantly, electrochemical methods can offer inexpensive instruments, short analysis time, simplicity, and great sensitivity. With this

back-ground, many electrochemical sensors have been developed to detect BPA using the direct oxidation reaction [17], which requires electrochemically active electrode NPs such as carbon [18,19], graphene [14,20], metal oxides [21–23], metal composites [24–26], and metals [27–29]. Since the direct oxidation of BPA may cause the deactivation of carbon or noble metal electrodes by poisoning, it is still a great challenge to develop more reliable, sensitive, and selective approaches. In addition, BPA oxidation occurs at a relatively high potential, lowering the selectivity due to co-oxidation of interfering species. It is thus necessary to find a new catalytic electrode material to enhance the sensor performance through direct BPA oxidation without electrode poisoning.

Such electrode materials, including carbon and various metals or precious metals, have been explored as potential candidates. Among the candidates, platinum (Pt) as an electrocatalytic material is used in various applications despite its high cost, because it can detect a wide range of various species [30]. After the invention of nanoporous/mesoporous structures with high surface area, noble metals, including Pt, have become highly attractive choices. In particular, they can be applied for the oxidation/detection of some organic species, such as glucose [7,31,32], phenols [28], and methanol [33–35], due to their high catalytic activity and controllable morphology.

Recently, Pt NPs with high surface to volume ratios have received much attention because they can provide outstanding electrochemistry performance compared to bulk platinum NPs [36–39]. Based on these advantages, we have introduced dendritic platinum nanoparticles (DPNs) for sensing BPA *via* its electrochemical oxidation reaction. A BPA sensor using only DPN electrode would be disturbed, however, by some other organic species, which directly affect the oxidization of the DPN layer. Thus, it is necessary to avoid interference from positively charged oxidisable species. One way to avoid the interference and enhance the sensitivity is to coat the DPN surface with a selective

polymer layer (polyethyleneimine, PEI) that has a positive charge, and/or lipid molecules (phosphatidylcholine, PC) bearing ammonium and phosphate head groups. BPA in particular bears OH groups, and they form hydrogen bonds with the head groups of PC, so that the sensor probe coated with a PEI layer having tertiary amine groups can provide additional interaction with BPA.

In the present work, therefore, the DPNs were prepared by the sonochemical method using micelles, and their morphology and structure were carefully characterized. The sensor was pre-pared with a layer of DPNs coated Au NPs deposited on a screen-printed carbon electrode, followed by the selective mem-brane with positive and interactive head groups. Hence, we formed a layer composed of PEI [40] and PC [41] on the DPN surface. The sensor performance of the DPN modified electrode was compared with that of a commercial platinum nanoparticle (Pt black) electrode through electrochemical methods. We also examined the interference effects of foreign species. Finally, the reliability of the as-designed sensor was evaluated using tap water with a view toward practical applications.

5.2 Experimental

Reagents and nanoparticles: Potassium tetrachloroplatinate(II) (K_2PtCl_4, 98%), polyethylene glycol hexadecyl ether (Brij 58, $HO(CH_2CH_2O)_{20}C_{16}H_{33}$), L-ascorbic acid (AA, $C_6H_8O_6$, reagent grade) bisphenol A (BPA), polyethyleneimine (PEI), acetaminophen (AP), dopamine (DA), and uric acid (UA) were obtained from Sigma-Aldrich. Platinum black was purchased from Alfa Aesar. Phosphatidylcholine (PC) was purchased from Avanti Polar Lipids, Inc. (USA). Phosphate buffer solution (0.1 M, pH 7.4) was prepared by mixing stock solutions of0.1 M NaH_2PO_4 and 0.1 M Na_2HPO_4.

Instruments: A screen-printed carbon electrode (SPCE) was used as a disposable all-solid-state sensor strip for the detection of bisphenol A. The carbon was insulated, with an area of 0.03141 cm^2 exposed for the working electrodes. Ag/AgCl was used as the reference electrode and pure carbon was also used as the counter electrode (Figure 5.1a) [42,43]. Amperograms and cyclic voltammograms (CVs) were recorded using a potentiostat/galvanostat (Ivium, Netherlandand, Kosentech, Korea). Detailed microstructures were examined using transmission electron microscopy (TEM) (JEOL-2100, Japan) and scanning electron microscopy (SEM) (Hitachi SU-8000, Japan). Wide-angle powder X-ray diffraction (XRD) patterns were obtained with a GBC MMA XRD at a scanning rate of 2° min^{-1}. X-ray photo-electron spectroscopy (XPS) was conducted on an ESCALAB 250. The wetting properties of DPNs, PEI/DPNs, and PEI-PC/DPNs samples were analysed by a contact angle 101 measurement system (PSM Company). The minimized energy between BPA and PC was calculated using Chem 3D pro12.0 (Perkin Elmer Informatics) and the obtained chemical structures at minimized energy state were described in Figure 5.7a.

Preparation of dendritic platinum nanoparticles (DPNs): For the preparation of the DPNs, we used the following solutions: 5 ml of 20 mM K_2PtCl_4 aqueous solution, 1 ml of 50 mg Brij® 58 aqueous solution, and 5 ml of 0.1 M ascorbic acid (AA) aqueous solution, respectively, with each solution kept at room temperature (20℃). The K_2PtCl_4 and Brij 58 solutions were mixed in another vessel, and subsequently, the AA aqueous solution was added. The mixed solution was reacted at room temperature (20℃) for 50 min under ultrasonication (220–240 V, 50–60 Hz). The precipitates were collected by centrifugation and washed several times with deionized (DI) water to remove the surfactant and excess reactants [44].

Preparation of gold nanoparticles (AuNPs): For the preparation of the colloidal gold solution, 1 ml of $HAuCl_4 \cdot 3H_2O$ (1 wt %) was stirred into 90 ml deionized water for 1 min, and then 2 ml of 38.8 mM sodium citrate was added to the solution with stirring for 1 min. Following this, 1 ml of fresh 0.075 wt % $NaBH_4$ in 38.8 mM sodium citrate solution was added very slowly with continuous stirring. The reaction mixture was allowed to stand for 15-20 min and then used without purification [45].

Preparation of PEI-PC/DPNs/AuNPs electrode: AuNPs (as prepared solution), DPNs (1 mg mL^{-1}), and Polyethyleneimine-Phosphatidylcholine (PEI-PC) membrane solutions were sequentially coated on a screen-printed carbon electrode, and the as-prepared electrode was dried in an oven at 55^{o}C: Firstly, the gold nanoparticles (AuNPs) were dropped onto the screen-printed carbon electrode (SPCE) and were dried. Secondly, the dendritic platinum nanoparticles (DPNs) were dropped on the AuNPs modified SPCE and were dried. The electrode surface was then activated by potential cycling from - 0.55 V to 1.1 V with a scan rate of 0.2 V s^{-1} for 30 cycles in 0.5 M sulfuric acid, and washed with distilled water (DI water). Finally, a membrane solution prepared by mixing PEI (0.5%) with PC (0.5 mM) (95 wt %: 5 wt %) was coated on the DPNs/AuNPs/SPCE and used for the experiments.

5.3 Results and discussion

To demonstrate the performance of the sensor using dendritic platinum nanoparticles (DPNs) for bisphenol A (BPA) detection, we strategically designed a three-layer electrode architecture, with the layers (from the top down) consisting of polyethyleneimine/phosphatidylcholine (PEI-PC), DPNs, and gold nanoparticles (AuNPs), respectively (denoted as PEI-PC/DPNs/AuNPs). Herein, the purpose of the

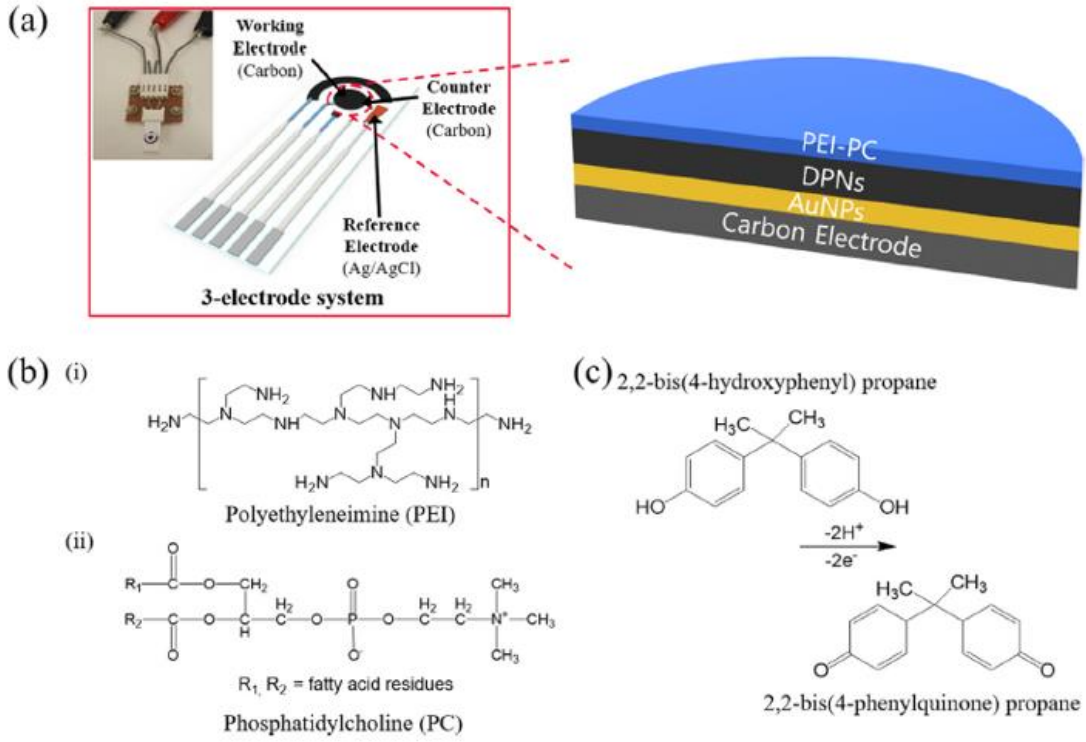

Figure 5.1. Photograph and schematic illustration of PEI-PC/DPNs/AuNPs electrode. (b) Chemical structures of polyethyleneimine (PEI) and phosphatidylcholine (PC). (c) Bisphenol A oxidation.

PEI-PC was to enhance sensitivity and to reduce the interference effect on the BPA sensor. The AuNPs were also used for stabilization of the screen-printed carbon electrode (SPCE). A photograph of the setup and a detailed illustration of the PEI-PC/DPNs/AuNPs on the SPCE are clearly shown in Figure 5.1a. Figure 5.1b displays the chemical structures of the components of PEI-PC, which can offer enhancement of the sensor's selectivity and

sensitivity due to their polarity and charge properties [46,47]. In the as-prepared electrode, the bisphenol A is detected from its electrochemical oxidation reaction, a two-electron and two-proton process, in which it is converted to 2,2-bis(4-phenylquinone) propane (Figure 5.1c).

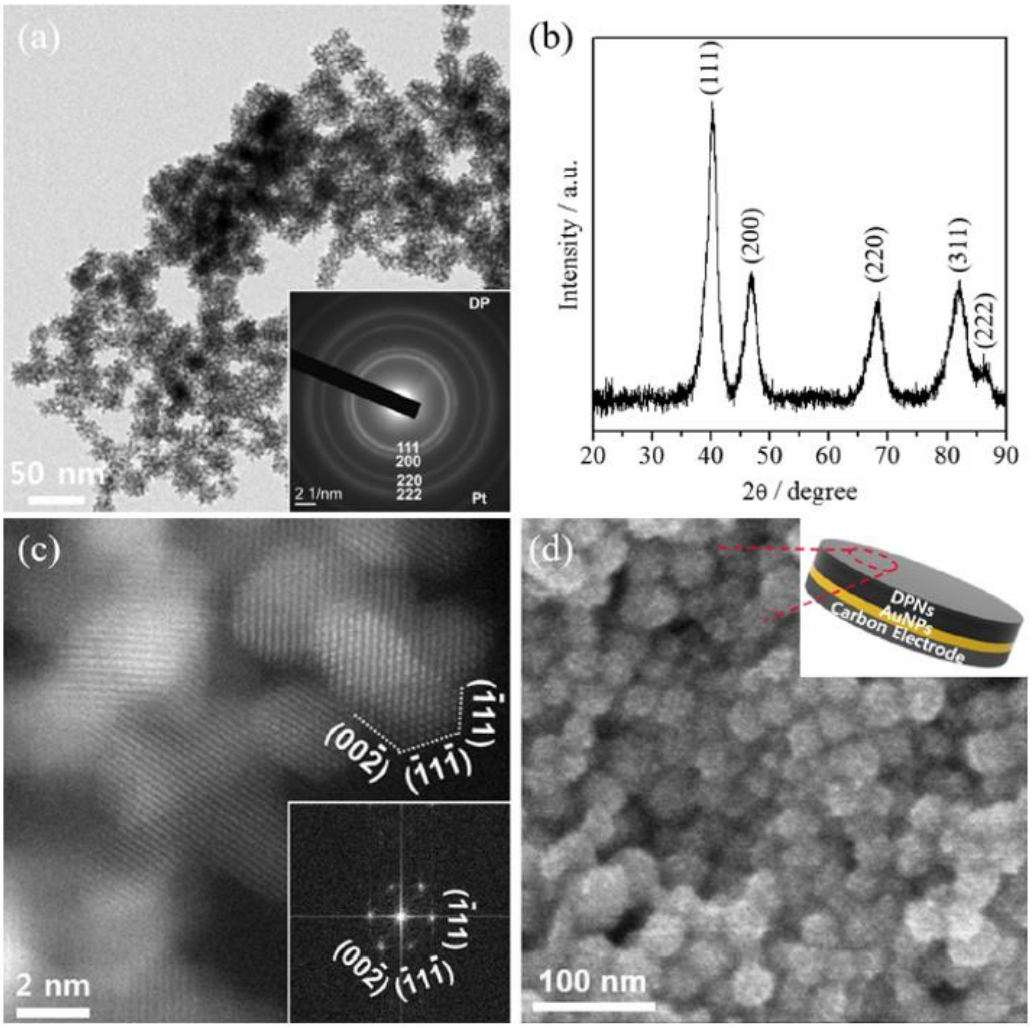

Figure 5.2. TEM image of prepared DPNs (inset: SAED pattern). (b) Wide-angle XRD pattern of DPN. (c) HAADF-STEM image of DPNs (inset: FFT pattern). (d) SEM image of DPNs/AuNPs on electrode (schematically illustrated in inset).

The structure of the DPNs prepared by the sonochemical method was observed by transmission electron microscopy (TEM) as shown in Figure 5.2. The as-prepared DPNs showed a dendritic structure with an abundance of pores 2-4 nm in size, which offer highly catalytic sites. The average size of the DPNs was estimated to be around 25 nm

(Figure 5.2a). The selected area diffraction pattern (SAED) in the inset confirmed that the particles have a typical face-centred-cubic(fcc) structure. In detail, the particles show concentric rings representing the (111), (200), (220), and (222) planes. This is further supported by the wide-angle X-ray diffraction (XRD) pattern, which exactly corresponds to the fcc structure (Figure 5.2b). From detailed high-angle annular dark field scanning TEM (HAADF-STEM) analysis, the {111} and {200} facets were observed in various beam orientations using fast Fourier transform (FFT) patterns (inset in Figure 5.2c). Based on this information, the DPNs were directly deposited on the AuNPs/carbon electrode. As can be seen in Figure 5.2d, the top-view scanning electron microscope (SEM) image provides the evidence of the successful coverage by DPNs. The DPN-coated electrode is composed of particles with homogeneous shapes and sizes.

The electrochemical active surface areas (ECSA) of the DPNs and commercial Pt black powders were closely compared using cyclic voltammetry (CV) in the range of -0.55 V to + 1.1 V (vs. Ag/AgCl) in a 0.5 M sulfuric acid (H_2SO_4) solution at the scan rate of 0.1 V s^{-1}. We observed that the DPNs possessed a relatively high hydrogen adsorption/desorption currents compared to the Pt black. From the results, the ECSA determined for DPNs was 5.46 m^2 g^{-1}, while that for the Pt black was estimated to be 3.78 m^2 g^{-1} (Figure 5.3a), indicating that the DPNs had more catalytic active sites. We propose that the DPNs reveal an enhanced current response for BPA due to their highly catalytic surfaces and sites.

The as-prepared electrode was further tested for electrochemical BPA detection. Before the determination of BPA, two DPNs (or Pt black)/AuNPs/carbon electrodes were first activated by scanning the potential from 0.0 V to 0.6 V at a scan rate of 0.1 V s^{-1} for 20 cycles. Through this step, it allows the stabilization of the baseline and the electrodes can get more reproducible response. After the electrodes were activated, CVs were

recorded in various concentrations of BPA by scanning the potential from 0.0 V to 0.6 V at a scan rate of 0.1 V s^{-1}. During the scan to the positive direction to + 0.6 V from 0.0 V, the voltammetric responses of the Pt black (Figure 5.3b) and DPNs (Figure 5.3c) powders to BPA in a phosphate buffered saline (PBS)buffer solution revealed a clear oxidation

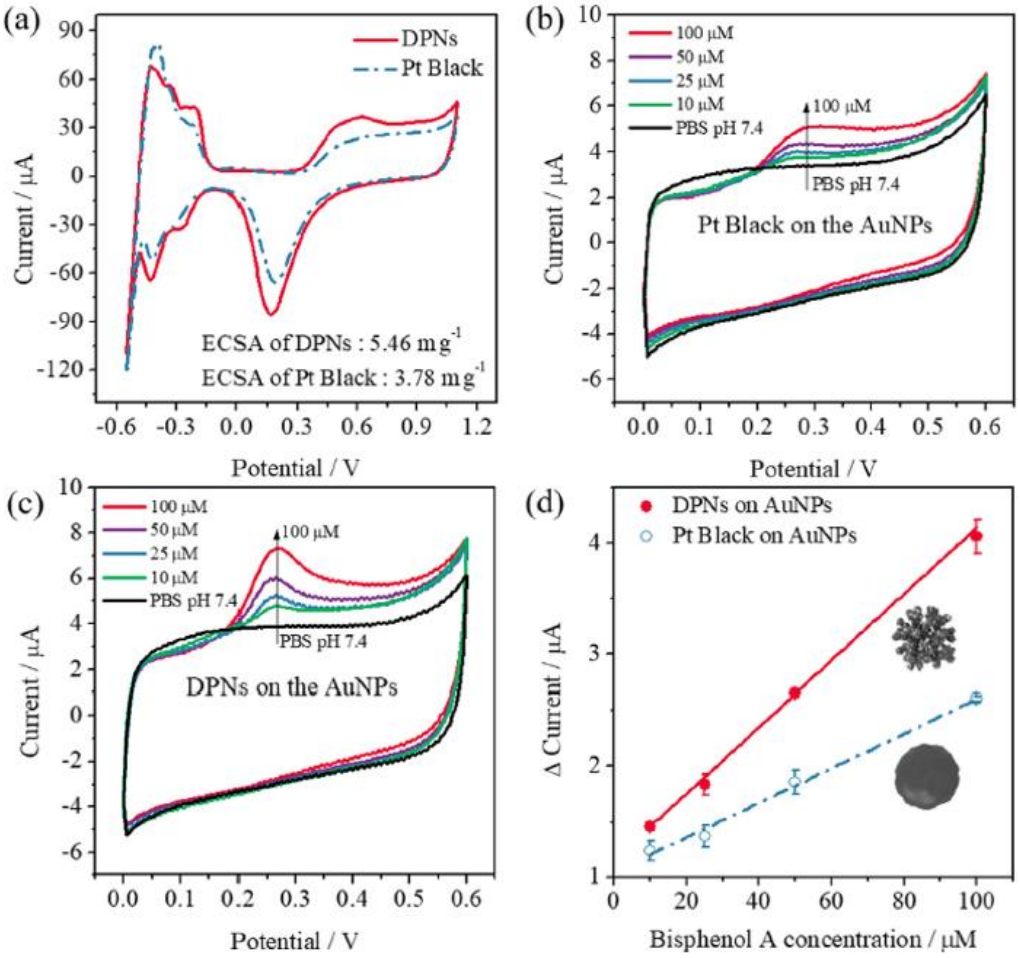

Figure 5.3. Cyclic voltammograms (CVs) for characterization of DPNs and Pt Black on the AuNPs modified electrodes. (a) Determination of electrochemical active surface area (ECSA) of DPNs and Pt Black. (b) Detection of various concentrations (10, 25, 50, and 100 µM) of bisphenol A using Pt Black electrode. (c) Detection of various concentrations (10, 25, 50, and 100 µM) of bisphenol A using DPNs electrode. (d) Bisphenol A detection calibration curves (DPNs and Pt black), with insets showing DPN and Pt Black particles.

peak at around + 0.27 V vs. Ag/AgCl (sat. KCl) (Figure 5.3b and c) in both cases, while no redox peaks were observed on either electrode in a blank PBS solution. From the results, the obtained response current of the DPNs was about two times higher than that of the Pt black. In addition, the calibration plots showed that the sensitivity of the DPNs

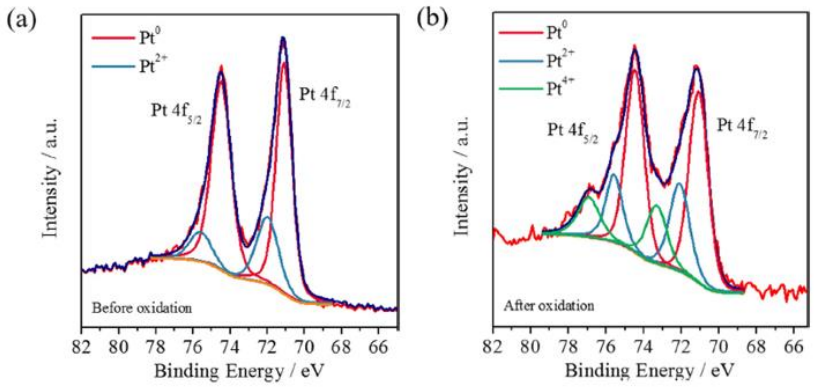

Figure 5.4. XPS analysis of surface of DPNs electrode: (a) before BPA oxidation, (b) after BPA oxidation.

modified electrode (slope = 0.0298 μA μM^{-1}) (red) is 2 times higher than that of the Pt black modified electrode (slope = 0.0155 μA μM^{-1}) (blue) (Figure 5.3d). These results indicate that the DPNs electrode has much better BPA sensing capability than commercially available Pt black electrodes. As a result, our DPNs were clearly worth applying on a BPA sensor.

To further characterize its working principle as a BPA sensor, we also evaluated the surface conditions of the DPNs modified electrode. For this purpose, detailed XPS spectra were obtained for the DPNs electrode before and after the oxidation of BPA in the phosphate buffer solution (PBS), as can be seen in Figure 5.4a and b. The XPS spectra of the DPNs modified electrode revealed peaks at 74.49 eV, 71.10 eV (Pt^0); and 75.6, 71.99

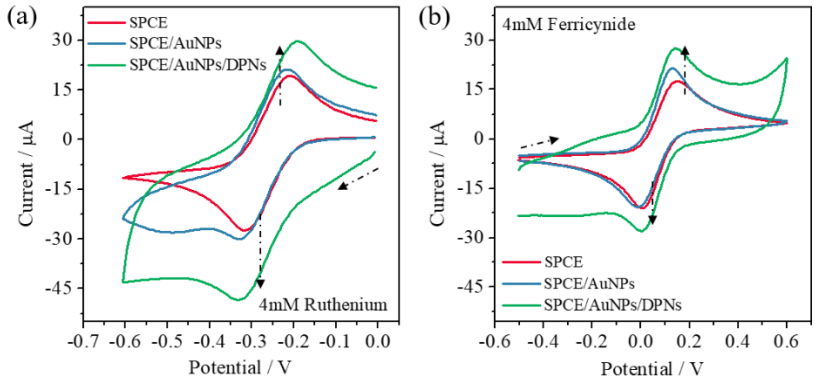

Figure 5.5. Redox currents of electrodes in (a) 4 mM $Ru(NH_3)_6Cl_3$ and (b) 4 mM $K_3[Fe(CN)_6]$ from cyclic voltammetry.

eV (Pt^{2+}) before the oxidation (Figure 5.4a). After the BPA oxidation, peaks were observed at 74.45 eV, 71.07 eV (Pt^0); 75.57 eV, 72.09 eV (Pt^{2+}); and 76.91 eV, 73.31 eV (Pt^{4+}) (Figure 5.4b). It should be noted that an additional peak (Pt^{4+}) was clearly present after the BPA oxidization on the DPNs electrode. That is to say, both Pt^0 and air oxidized Pt^{2+} at the DPNs surface are partially oxidized to Pt^{4+} during the oxidation of BPA. This result can support an electrochemical oxidation reaction of the BPA, as described in Fig. 5.1c. The detailed electrochemical surface properties of different electrodes in negatively charged $K_3Fe(CN)_6$ and positively charged $[Ru(NH_3)_6]Cl_3$ solutions are provided in Figure 5.5.

The electrochemical surface properties of the bare SPCE electrode and each subsequent layer of the electrode were characterized through the observation of the redox behaviors of the negatively charged $K_3[Fe(CN)_6]$ and the positively charged $Ru(NH_3)_6Cl_3$ ions. CVs were recorded for the SPCE, AuNPs/SPCE, and DPNs/AuNPs/SPCE layers in

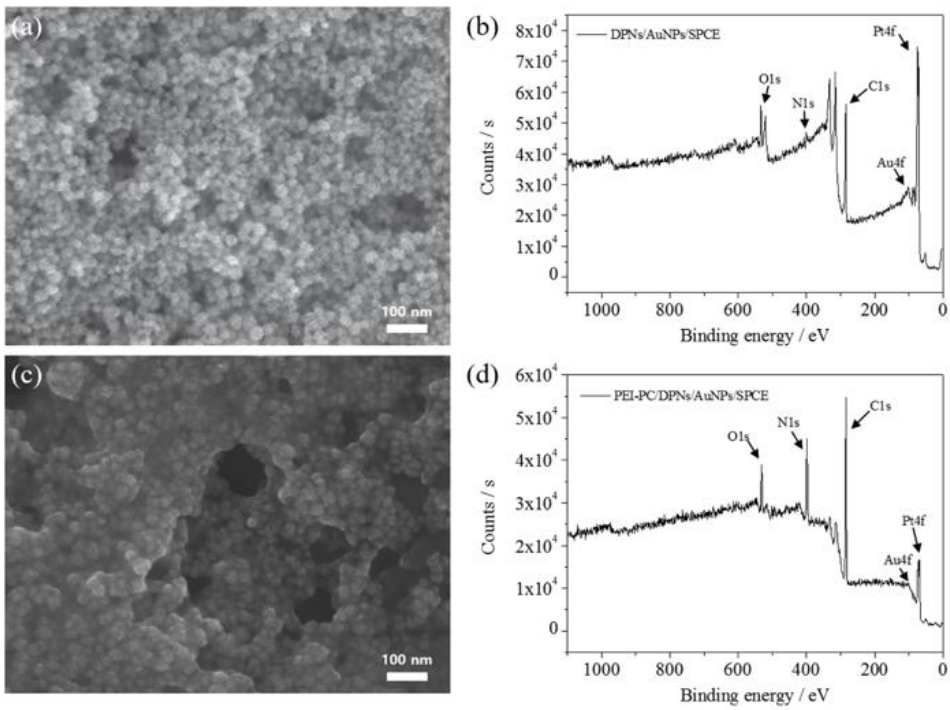

Figure 5.6. (a) SEM image of DPNs/AuNPs/SPCE. (b) XPS survey spectrum of DPNs/AuNPs/SPCE. (c) SEM image of PEI-PC/DPNs/AuNPs/SPCE. (d) XPS survey spectrum of PEI-PC/DPNs/AuNPs/SPCE.

4 mM hexaammineruthenium(III) chloride ($Ru(NH_3)_6Cl_3$) between 0.0 and -0.6 V (Figure 5.5a) and 4 mM potassium ferricyanide(III) ($K_3[Fe(CN)_6]$) solution between -0.5 V and 0.6 V (Figure 5.5b). Herein, the CVs for all the layers revealed a quasi-reversible process, showing a pair of redox peaks in both $K_3[Fe(CN)_6]$ and $Ru(NH_3)_6Cl_3$ solutions, which indicates that the surface charge of the modified electrode was almost neutral. In the case of the DPNs electrode, the redox peak current was slightly increased, reflecting the high porosity of the DPNs. According to these results, the DPNs modified electrode did not have a specific response to any negative or positive charges.

Finally, we also needed to confirm the surface oxidization and surface morphology of DPNs with and without PEI-PC. From the SEM observations, the surface was composed of homogeneously dispersed DPNs before deposit of the PEI-PC layer (Figure 5.6a), while a murky image of DPNs was observed after the PEI-PC layer coat-ing (Figure 5.6c). That is to say, there is an obvious thin coating layer of PEI-PC on the DPNs. The formation of each layer was additionally confirmed using XPS (Figure 5.6b and d). The XPS spectra obtained for the PEI-PC layer showed O1s, N1s, and C1s peaks with relatively strong intensity after PEI-PC coating, while the XPS intensity of Pt 4f was relatively decreased. This indicates that the PEI-PC layer covered the electrode surface completely.

As was described above, to improve the sensitivity and reduce interference effects, the DPNs/AuNPs/SPCE (denoted as DPNs-modified electrode) was covered with a functional layer, which was drop-coated by mixed solutions of PEI and PC with different weight percentages. Anion permeation can be achieved by covering the electrode with a positively charged PEI layer to protect it from interference by other species [40]. Otherwise, the PC, having both positively charged tertiary amine and negatively charged

phosphate groups in the head part, would give the coating a neutral property [41]. In addition, the tail group of the PC molecule has a hydrophobic property that can protect the sensor from other hydrophilic interfering species, and also, the head group of PC can form a hydrogen bond with the OH group of BPA to enhance the sensitivity of the sensor. Theoretically, a highly sensitive layer can be designed through the orientation of the head group of the PC so that it faces inward and the tail part faces outward on the PEI layer. Based on these considerations, the selectivity and sensitivity to the target species was improved, so that the interference effect by positively charged molecules was reduced, and the hydro-gen bond formation between the head groups of PC and BPA could enhance the sensitivity. To support our hypothesis about the complex interaction between

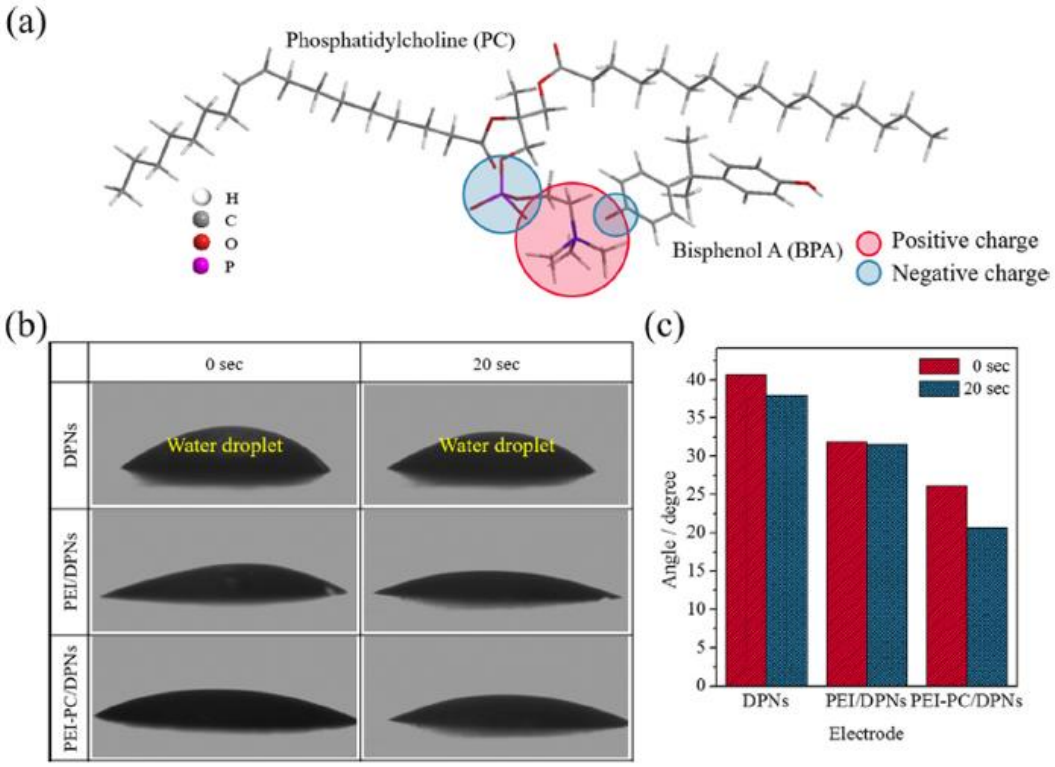

Figure 5.7. (a) The chemical structure of interaction of between BPA and PC at minimized energy. (b) Photographs of water contact angles of various layers (DPNs, PEI/DPNs, and PEI-PC/DPNs). (c) Contact angles of various layers (DPNs, PEI/DPNs, and PEI-PC/DPNs).

the BPA and the PC, their interactions were studied by calculating the minimized energy. The interaction of deprotonated phenyl groups of BPA and $(CH_3)_3N^+$ groups of PC was expected to be stable (Figure 5.7a). Therefore, the rationally design sensor can be fabricated using a PEI-PC layer. To evaluate its reliability, CVs were recorded for a sample solution containing bioorganic interfering molecules, such as dopamine, and the sensor showed a reduced response for positively charged interfering species. This indicates that the PEI-PC layer plays an important role in protecting the sensor from interference effects and improving sensitivity.

Most conventional electrodes composed of various metal NPs have the drawbacks that they simultaneously detect mixed species, including ascorbic acid (AA), acetaminophen (AP), uric acid (UA), and dopamine (DA), even at different oxidation potentials. With this background, our strategic PEI-PC coating was introduced onto the DPNs-modified electrode due to its selectively oxidized functionality and minimization of interference effects. To obtain the best response from the PEI-PC/DPNs/AuNPs, therefore, the experimental conditions were systematically optimized in terms of the amount of DPNs, the concentration of PEI, and the ratio of PC to PEI (Figure 5.8). In regard to the amount of DPNs, 3 μL (1 mg mL^{-1}) of DPNs was drop-coated on the AuNPs deposited on the SPCE from one to four times, as can be seen in Supporting Information Figure 5.8a. In detail, the CVs (not shown here) were evaluated for the DPNs-modified electrodes with different amounts of DPNs (3 μL–12 μL) in PBS solution containing various concentrations of BPA (2.5 μM–10 μM). The results clearly revealed that the electrode coated with 3 μL (1 mg mL^{-1}) of DPNs gave us the steepest calibration slope.

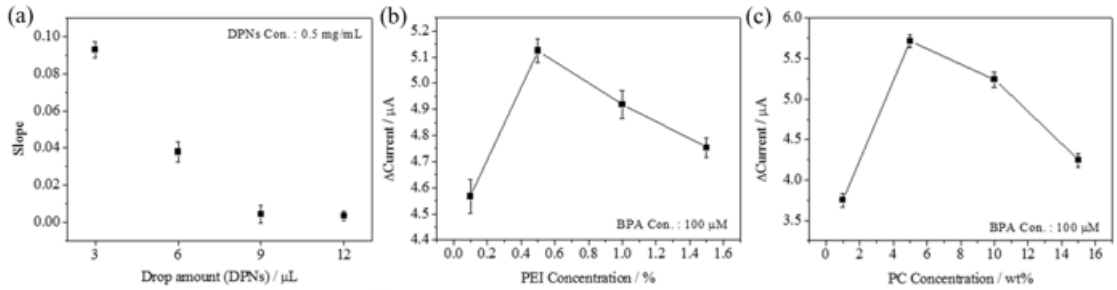

Figure 5.8. Optimization of experimental parameters in terms of (a) deposited amount (DPNs), (b) PEI concentration, and (c) PC concentration.

The effect of PEI concentration on the response current was investigated between 0.1 and 1.5% in 100 M of BPA solution (Figure 5.8b). In this case, 0.5% PEI minimized the decrease in the current response. As was mentioned above, however, using only PEI was not enough to avoid interference and to give more selectivity. Hence, the DPNs surface was covered with a lipid (PC) layer along with the PEI, where the - OH group of BPA was more interactive to the head group of PC molecules through the hydrogen bond formation. To optimize the is, the weight (wt %) ratio of PEI to PC was varied on the DPNs layer. As shown in Figure 5.8c, the maximum response and selectivity toward BPA were observed for the sensor probe with a ratio of 95: 5 wt % (PEI:PC), which was finally applied to the subsequent experiments.

To confirm the adaptability of as-optimized polymer layers (PEI-PC), we evaluated the sample solution permeability for different layer architectures. The water contact angle for all samples was measured at time intervals of 0 and 20 s, (Figure 5.7b). The angles for three samples at 0 s and 20 s were 40.7° and 38° (DPNs); 31.9° and 31.6° (PEI/DPNs); 26.2° and 20.7° (PEI-PC/DPNs), respectively (Figure 5.7c). This suggests that the wettable nature of the DPNs surface also increases with the surface modification using PEI and PC. In particular, the PEI-PC/DPNs layer reveals the lowest contact angle, which is the best condition. In addition, the wetting property for all samples was further

increased with increasing wetting time, which indicates the better interaction of target species in the solution to be measured with increasing time. With this experimental result, the PEI-PC layer can give us greater responsiveness.

Finally, the interference effects on BPA detection using the PEI-PC/DPNs/AuNPs/SPCE sensor probe were further investigated with 0.5% PEI and 0.5% PEI with PC (0.5 mM phosphatidylcholine, ratio 0.5% PEI (95 wt %) and PC (5 wt %)). In addition, only the DPNs electrode was tested as reference. After electrode activation,

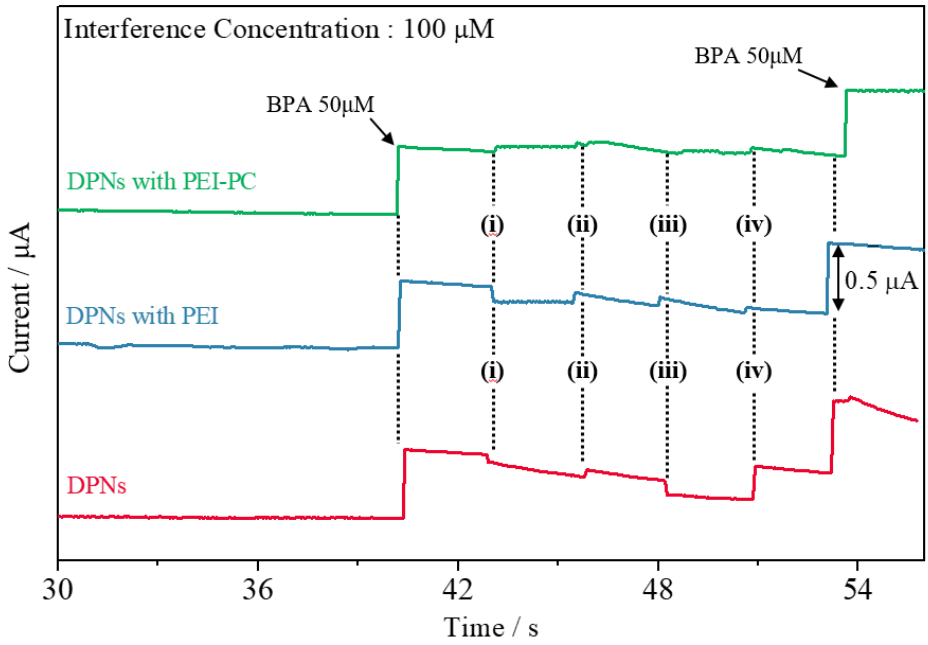

Figure 5.9. Amperograms of the addition of 50 µM BPA and 100 µM of other interfering species in various electrodes (i: ascorbic acid, ii: acetaminophen, iii: uric acid, and iv: dopamine).

the amperometric responses for the oxidation of BPA and the expected interfering species were assessed between the initial potential of 0.0 V and the final potential of 0.4 V: bisphenol A (BPA) as a reference, and (i) ascorbic acid (AA), (ii) acetaminophen (AP), (iii) uric acid (UA), and (iv) dopamine (DA) (Figure 5.9). All the interference was decreased in the order of DPNs/AuNPs, PEI/DPNs/AuNPs, and PEI-PC/DPNs/AuNPs layers. The interference effects were investigated for AA, AP, UA, and DA a reduction

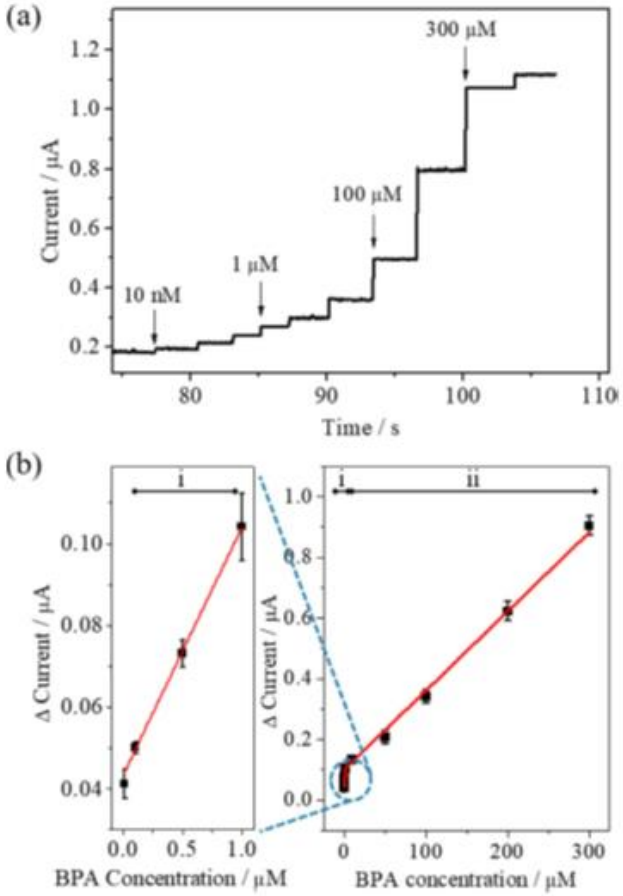

Figure 5.10. (a) Amperometric response of PEI-PC/DPNs/AuNPs modified SPCE according to different concentrations of BPA. (b) Calibration curves from the amperometric responses at two ranges of BPA concentration: of (i) 0.01–1 µM and (ii) 1–300 µM.

in response current was observed on AA (14%), AP (24%), UA (35%), and DA (22%), respectively. After only PEI coating, the response current was somewhat decreased compared to that of bare DPNs, where the percent ratios of the response current were AA (13%), AP (16%), UA (22%), and DA (18%), respectively. On the other hand, the PEI-PC coated-electrode showed a greatly decreased interference effect for AA (4%), AP (3%), UA (5%), and DA (3%) (Figure 5.9). The electrodes with only a PEI layer showed high-interference responses (over 10%), while the PEI-PC modified electrode displayed low-interference responses (below 5%).

A typical current response curve was observed during successive addition of various concentrations of BPA in a 0.1 M PBS solution using chronoamperometry (CA) (Figure 5.10a). In detail, the stepping potential of 0.4 V was applied to obtain amperograms of the BPA sensor probe with the PEI-PC/DPNs/AuNPs architecture. Two dynamic ranges of the calibration plot for the BPA detection were determined from 0.01 to 1.0 μM and from 1.0 μM to 300 μM with respective correlation coefficients of 0.9957 and 0.9864, respectively (Figure 5.10b). Two different linear ranges are due to the different kinetics at different concentrations of BPA. The oxidation kinetics in the low concentration range was related to only adsorption process, and the oxidation process at high concentration range depended on adsorption and diffusion of BPA [48,49]. The detection limit (DL)of BPA was determined to be 6.63 ± 0.77 nM. Compared to previous reports [19,23,24,26,29,50–57], the DL reported in this work was quite comparable to those for

Table 5.1. Comparison of proposed sensors for detection of BPA by the electrochemical method (direct oxidation).

Active materials	Linear range	Detection limit	References
DPNs	0.01-1, 1-300 μM	6.6 nM	This work
MCM-41	0.088-0.22 μM	38 nM	23
Pt/Gr-CNTs	0.06-10.0 μM	42 nM	24
AuNPs/MoS_2	0.05-100 μM	5 nM	26
Pd@TiO_2-SiC	0.01-5, 5-200 μM	4.3 nM	29
MWCNTs-PEI	0.01-50 μM	3.3 nM	19
Arg-G	0.005-40 μM	1.1 nM	50
Laccase-Thionine-Carbon black	0.5-50 μM	200 nM	51
MWCNTs	4.9-82.5 μM	84 nM	52
ZrO_2/Nano-ZSM-5	0.006-600 μM	3 nM	53
Na-doped WO_3	0.081-22.5 μM	28 nM	54
AuPdNPs/GNs	0.05–10 μM	8 nM	55
AuNP/PVP/PGE	0.03–1.1 μM	1 nM	56
GO/MWCNT	0.05 to 1, 1 to 650 μM	4.4 nM	57

* Gr-CNT (Graphene-carbon), MCM-41 (Mesoporous silica), AuNPs (Gold nanoparticles), MWCNTs (Multi-walled carbon nanotubes), PEI (Polyethylenimine), Arg-G (Arginine functionalized graphene), Nano-ZSM-5 (Nanocrystalline ZSM-5 zeolite), GNs (Graphene nanosheets), PVP (polyvinylpyrrolidone), PGE (pencil graphite electrode), GO (graphene oxide), MWCNT (multiwalled carbon nanotubes).

other sensing NPs using the direct oxidation method (Table 5.1). In order to investigate its reliability, we also investigated the PEI-PC/DPNs/AuNPs modified

Table 5.2. Recovery of spiked BPA in tap water. RSD: relative standard deviation.

Sample	Spiked (µM)	Found (µM)	Recovery (%)	RSD (%)
Tap water	1	0.95	94.55	3.06
	5	5.13	102.63	2.65
	10	10.39	103.90	6.77

electrode for the detection of BPA in tap water through a recovery study. Blank solutions were mixed from tap water and PBS in the ratio of 1:1, and three different concentrations of BPA were obtained by mixing it with the blank solution. In this case, the range of recovery was from 95% to 104% (Table 5.2), indicating that our sensor design paves the way toward practical application.

5.4 Conclusions

We have successfully fabricated and evaluated the highly catalytic dendritic platinum nanoparticles (DPNs) for detection of bisphenol A (BPA). As-prepared DPNs having a high surface area showed very selective and sensitive detection as the sensor. More-over, the interference effect was obviously reduced by top coating of PEI and PC. Finally, our sensor was further tested in a tap water through recovery study toward practical applications.

5.5 References

[1] H. Yin, L. Cui, S. Ai, H. Fan, L. Zhu, Electrochim. Acta, 2010, **55**, 603-610.

[2] H. Yoshida, H. Harada, H. Nohta, M. Yamaguchi, Anal. Chim. Acta, 2003, **488**, 211-221.

[3] G. M. Kleˇcka, C. A. Staples, K. E. Clark, N. V. D. Hoeven, D. E. Thomas, S. G. Hentges, Environ. Sci. Technol., 2009, **43**, 6145-6150.

[4] L. N. Vanderberg, R. Hauser, N. Marcus, W. V. Welshons, Reprod. Toxicol., 2007, **24**, 139-177.

[5] H. Mielke, U. Gundert-Remy, Toxicol. Lett., 2009, **190**, 32-40.

[6] Z. Kuklenyik, J. Ekong, C. D. Cutchins, L. L. Needham, A. M. Calafat, Anal. Chem., 2003, **75**, 6820-6825.

[7] E. Maiolini, E. Ferri, A. L. Pitasi, A. Montoya, M. D. Giovanni, E. Errani, S. Girotti, Analyst, 2014, **139**, 318-324.

[8] H.-B. Noh, P. Chandra, Y.-J. Kim, Y.-B. Shim, Anal. Chem., 2012, **84**, 9738-9744.

[9] X. Wang, H. Zeng, L. Zhao, J.-M. Lin, Anal. Chim. Acta, 2006, **556**, 313-318.

[10] J. Fan, H. Guo, G. Liu, P. Peng, Anal. Chim. Acta, 2007, **585**, 134-138.

[11] J. Zhang, S.-Q. Zhao, K. Zhang, J.-Q. Zhou, Chemosphere, 2014, **95**,105-110.

[12] M.-H. Piao, H.-B. Noh, M. A. Rahman, M.-S. Won, Y.-B. Shim, Electroanalytical, 2008, **20**, 30-37.

[13] M. A. Rahman, M. J. A. Shiddiky, J.-S. Park, Y.-B. Shim, Biosens. Bioelectron., 2007, **22**, 2464-2470.

[14] Y. Zhu, Y. Cai, L. Xu, L. Zheng, L. Wang, B. Qi, C. Xu, ACS Appl. Mater. Interfaces, 2015, **7**, 7492-7496.

[15] S. G. Kim, S.L. Lee, J. Jun, D. H. Shin, J. Jang, ACS Appl. Mater. Interfaces, 2016, **8**, 6602-6610.

[16] C. Cheng, S. Wang, J. Wu, Y. Yu, R. Li, S. Eda, J. Chen, G. Feng, B. Lawrie, A. Hu, ACS Appl. Mater. Interfaces, 2016, **8**, 17784-17792.

[17] K. V. Ragavan, N. K. Rastogi, M. S. Thakur, TrAC Trends Anal. Chem., 2013, **52**, 248-260.

[18] J. A. Rather, K. D. Wael, Sens. Actuators B: Chem., 2013, **176**, 110-117.

[19] Y. Yang, H. Zhang, C. Huang, N. Jia, Sens. Actuators B: Chem., 2016, **235**, 408-413.

[20] H. Fan, Y. Li, D. Wu, H. Ma, K. Mao, D. Fan, B. Du, Q. Wei, Anal. Chim. Acta, 2012, **711**, 24-28.

[21] L. Hu, C.-C. Fong, X. Zhang, L. L. Chan, P. K. S. Lam, P. K. Chu, K.-Y. Wong, M. Yang, Environ. Sci. Technol., 2016, **50**, 4430-4438.

[22] C. Hou, W. Tang, C. Zhang, Y. Wang, N. A. Zhu, Electrochim. Acta, 2014, **144**, 324-331.

[23] F. Wang, J. Yang, K. Wu, Anal. Chim. Acta, 2009, **638**, 23-28.

[24] Z. Zheng, Y. Du, Z. Wang, Q. Feng, C. Wang, Analyst, 2013, **138**, 693-701.

[25] D. Pan, Y. Gu, H. Lan, Y. Sun, H. Gao, Anal. Chim. Acta, 2015, **853**, 297-302.

[26] K.-J. Huang, Y.-J. Liu, Y.-M. Liu, L.-L. Wang, J. Hazard. Mater., 2014, **276**, 207-215.

[27] R. Wannapob, P. Thavarungkul, S. Dawan, A. Numnuam, W. Limbut, P. Kanatharana, Electroanalysis, 2016, **28**, 1-10.

[28] Z. Zheng, J. Liu, M. Wang, J. Cao, L. Li, C. Wang, N. Feng, J. Electrochem. Soc., 2016, **163**, B192-B199.

[29] L. Yang, H. Zhao, S. Fan, B. Li, C.-P. Li, Anal. Chim. Acta, 2014, **852**, 28-36.

[30] M. Malgras, H. Ataee-Esfahani, H. Wang, B. Jiang, C. Li, K. C.-W. Wu, J. H. Kim, Y. Yamauchi, Adv. Mater., 2016, **28**, 993-1010.

[31] Q. Shen, L. Jiang, H. Zhang, Q. Min, W. Hou, J.-J. Zhu, J. Phys. Chem. C, 2008, **112**, 16385-16392.

[32] X. Niu, H. Zhao, C. Chen, M. Lan, ChemCatChem, 2013, **5**, 1416-1425.

[33] D.-S. Park, M.-S. Won, R. N. Goyal, Y.-B. Shim, Sens. Actuators B: Chem., 2012, **174**, 45-50.

[34] M. Rauber, I. Alber, S. Müller, R. Neumann, O. Picht, C. Roth, A. Schökel, M. E. Toimil-Molares, W. Ensinger, Nano Lett., 2011, **11**, 2304-2310.

[35] S. M. Alia, G. Zhang, D. Kisailus, D. Li, S. Gu, K. Jensen, Y. Yan, Adv. Funct. Mater., 2010, **20**, 3742-3746.

[36] L. Wang, Y. Yamauchi, J. Am. Chem. Soc., 2009, **131**, 9152-9153.

[37] L. Wang, Y. Yamauchi, J. Am. Chem. Soc., 2010, **132**, 13636-13638.

[38] B. Jiang, C. Li, M. Imura, J. Tang, Y. Yamauchi, Adv. Sci., 2015, **2**, 1500112.

[39] B. P. Bastakoty, Y. Li, S. Guragain, S. M. Alshehri, M. J. A. Shiddiky, Z. Liu, K. Shim, J. H. Kim, M. S. A. Hossain, V. Malgras, Y. Yamauchi, Mater. Lett., 2016, **182**, 190-193.

[40] L. L. Israel, E. Lelloushe, S. Ostrovsky, V. Yarmiayev, M. Bechor, S. Michaeli,J.-P.M. Lellouche, ACS Appl. Mater. Interfaces, 2015, **7**, 15240-15255.

[41] M. Pasenkiewicz-Gierula, Y. Takaoka, H. Miyagawa, K. Kitamura, A. Kusumi, Biophys. J., 1999, **76**, 1228-1240.

[42] N.-H. Kwon, K.-S. Lee, M.-S. Won, Y.-B. Shim, Analyst, 2007, **132**, 906-912.

[43] D.-M. Kim, S.-J. Cho, C.-H. Cho, K.-B. Kim, M.-Y. Kim, Y.-B. Shim, Biosens. Bioelectron., 2016, **79**, 165-172.

[44] K. Shim, J. Kim, Y.-U. Heo, B. Jiang, C. Li, M. Shahabuddin, K. C.-W. Wu, M. S. A. Hossain, Y. Yamauchi, J. H. Kim, Chem. Asian J., 2017, **1**, 21-26.

[45] M. J. A. Shiddiky, Y.-B. Shim, Anal. Chem., 2007, **79**, 3724-3733.

[46] M. A. Rahman, A. Kothalam, E. S. Choe, M.-S. Won, Y.-B. Shim, Anal. Chem., 2012, **84**, 6654-6660.

[47] N. G. Gurudatt, M. H. Naveen, C. Ban, Y.-B. Shim, Biosens. Bioelectron., 2016, **86**, 33-40.

[48] H. Zhu, A. Sigdel, S. Zhang, D. Su, Z. Xi, Q. Li, S. Sun, Angew. Chem. Int. Ed., 2014, **53**, 12716-12720.

[49] M. H. Naveen, N. G. Gurudatt, H.-B. Noh, Y.-B. Shim, Adv. Funct. Mater., 2016, **26**, 1590-1601.

[50] Y. Zhang, L. Wang, D. Lu, X. Shi, C. Wang, X. Duan, Electrochim. Acta, 2012, **80**, 77-83.

[51] M. Portaccio, D. D. Tuoro, F. Arduini, D. Moscone, M. Cammarota, D. G. Mita, M. Lepore, Electrochim. Acta, 2013,**109**, 340-347.

[52] L. A. Goulart, F. C. D. Moraes, L. H. Mascaro, Mater. Sci. Eng. C, 2016, **58**, 768-773.

[53] B. Kaur, B. Satpati, R. Srivastava, RSC Adv., 2016, **6**, 65736-65746.

[54] Y. Zhou, L. Yang, S. Li, Y. Dang, Sens. Actuators B: Chem., 2017, **245**, 238-246.

[55] B. Su, H. Shao, N. Li, X. Chen, Z. Cai, X. Chen, Talanta, 2017**, 166**, 126-132.

[56] Y. T. Yaman, S. Abaci, Sensors, 2016, **16**, 756.

[57] J. Li, D. Kuang, Y. Feng, F. Zhang, M. Liu, Microchim. Acta, 2011, **172**, 379-386.

6. Rationally designed bimetallic Au@Pt nanoparticles for glucose oxidation

6.1 Introduction

Metal nanoparticles (NPs) have attracted significant attention in various fields because of their unique chemical and physical properties, which can be easily tuned by tailoring their size, shape, and composition. Surface area and crystallinity also affect their properties [1]. Among these NPs, noble metals, including Pt, Au, Ag, and Pd, are particularly important for catalysts [2,3], sensors [4,5], photonics [6,7], and medicine [8,9]. As explained in one of the most extensive studies, Pt NPs are highly attractive due to their superior catalytic activity, despite their high cost [2]. To overcome this issue, various mesoporous architectures have been employed to reduce the relative Pt content. In particular, the catalytic efficiency can be easily improved through a large surface-to-volume ratio. In addition to these methods, composition changes to partially replace the Pt by the addition of carbon and/or metals (Fe, Co, Ni, Pd, Au, and Ag) have also been accelerated for greater catalytic activity and durability [10-18].

According to this research background, bimetallic NPs are expected to exhibit unique properties, not only a combination of the properties characteristic of the two metals, but also due to the synergetic effects of the two metals [19]. It is well known that bimetallic NPs are synthesised by various methods: chemical reduction, thermal decomposition, biosynthesis, galvanic replacement, and sonochemical and radiolytic methods. The structures of bimetallic NPs are classified into three types: (i) core-shell, (ii) cluster in cluster, and (iii) random alloy and alloy structures. The shape and size of bimetallic NPs are precisely determined by their preparation methods and conditions. Due to these properties, bimetallic based NPs, which have the structures of nanospheres [20,21],

nanowires/tubes [22,23], nanosheets [24,25], and nanocages/frames [2,26], have been suggested and employed for different catalysis and sensor applications.

In detail, a range of bimetallic based NPs are used as electrode materials in the sensing field to detect methanol [27], glucose [28], phenol [29], hydrogen peroxide [30], and biologically important small organic molecules [31]. Among them, glucose oxidation reactions in particular were included in our study because diabetes mellitus has contributed greatly to human suffering. Many electrode materials have already been reported for non-enzymatic detection of biologically important organic compounds, including glucose. It is still necessary, however, to find new catalytic electrode materials to enhance sensing performance in neutral solution. Metal based electrode materials are known to show the good catalytic performance in basic solution. In neutral solution, however, glucose oxidation is even more important for practical industry and biological application fields. Hence, composites of Au and Pt NPs are still being explored as potential candidate electrode materials. Therefore, we selected Au and Pt composite material to form core-shell structure for a highly sensitive glucose oxidation reaction.

In this work, we synthesised core-shell Au@Pt structures with different molar ratios (Au^{3+} to Pt^{2+} (denoted as Au@Pt) = 3:7, 5:5, 7:3) by a surfactant-assisted process using the ultrasonic irradiation method [32]. Changing the precursor's content ratio is expected to modify the thickness of the Pt shell in the core-shell structures of Au@Pt NPs. The NPs were precisely characterized by transmission electron microscopy (TEM), wide-angle powder X-ray diffraction (XRD), cyclic voltammetry (CV), and chronoamperometry (CA). We finally examined the glucose oxidation reaction according to the thickness of the Pt shell, which resulted from the different composition ratios of Au to Pt.

6.2 Experimental

Reagents and nanoparticles: Polyethylene glycol hexadecyl ether (Brij 58®, $HO(CH_2CH_2O)_{20}C_{16}H_{33}$), potassium tetrachloroplatinate(II) (K_2PtCl_4, 98%), D-(+)-glucose, and gold(III) chloride trihydrate ($HAuCl_4 \cdot 3H_2O$, ≥ 99.9% trace metals basis) were obtained from Sigma-Aldrich Co. (USA). A phosphate buffer solution (PBS) was prepared using 0.1 M sodium dihydrogen phosphate (NaH_2PO_4, Sigma-Aldrich Co. USA) and 0.1 M disodium hydrogen phosphate ($Na_2H_2PO_4$, Sigma-Aldrich Co. USA). All aqueous solutions were prepared in doubly distilled water (18 MΩ cm).

Preparation of different molar ratios of core-shell Au@Pt NPs: Three different ratios (3:7, 5:5, 7:3) of Au ($HAuCl_4$, 20 mM) to Pt (K_2PtCl_4, 20 mM) in mixed solutions were prepared (5 ml). The solution was then mixed with Brij 58® (0.05 g) in a vial, and 5.0 mL of ascorbic acid (AA) solution (0.1 M) was added. This solution was reacted at room temperature for 1 hour under ultrasonication (220-240 V, 50-60 Hz). The precipitates were collected by centrifugation and washed several times with a deionized (DI) water and ethanol mixed solution to remove the surfactant and excess reactants.

Instruments: The morphology and structure of the different molar ratios (3:7, 5:5, 7:3) of Au@Pt were observed using TEM (JEOL 2010 and JEOL-2100, Japan) and SEM (JEOL 7500, JAPAN). Wide-angle powder XRD patterns were obtained with a GBC MMA XRD at a scan rate of 2° min^{-1}. Size distribution analysis obtained using SZ-100 (HORIBA, JAPAN). The screen-printed carbon electrodes (SPCEs) were composed of carbon, Ag/AgCl, and carbon as a three electrode system (working, reference, and counter electrodes). A solid-state Ag/AgCl reference electrode was prepared according to a previous report. The electrode was printed on a polystyrene-base film with carbon and silver inks (Jujo Chemical, Japan) employing a screen printer (Bando Industrial, Korea)

[4]. Amperograms and cyclic voltammograms (CVs) were recorded using a potentiostat/galvanostat (Kosentech Model PT-1 and EG & G PAR Model PAR 273A).

6.3 Results and discussions

For the synthesis of core-shell structured Au@Pt nanoparticles (NPs), amphiphilic $HAuCl_4$ and K_2PtCl_4 in different molar ratios (Au:Pt = 3:7, 5:5, 7:3) with Brij58® were reacted using the sonochemical method (Figure 6.1). Firstly, the Au (20 mM) and Pt (20 mM) precursor solutions were mixed in different molar ratios, and then Brij 58 solution was added into each solution. Secondly, ascorbic acid (AA) solution as a reducing agent was mixed with each prepared solution under ultrasonication. The procedure involved the

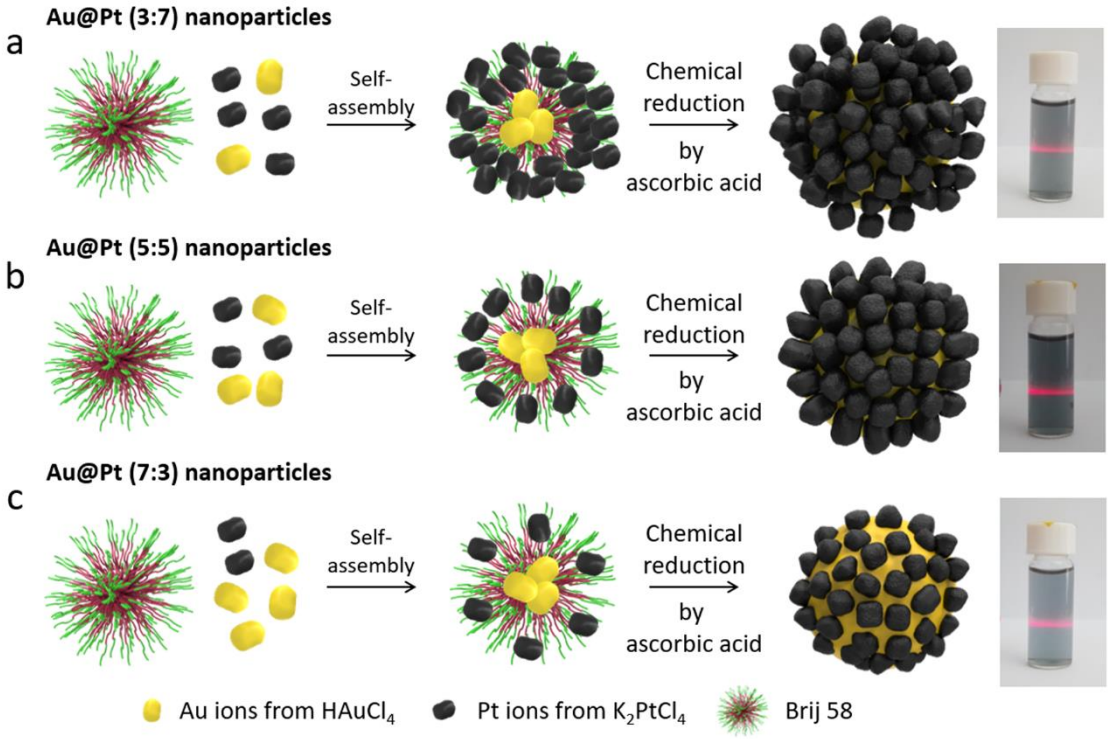

Figure 6.1. Illustrations of synthesis of Au@Pt nanoparticles with three different Au:Pt ratios (a) 3:7, (b) 5:5, and (c) 7:3 (left), and photographs of the Tyndall effect on Au@Pt suspensions in solution (right).

use of the reducing agent AA to obtain the core-shell structured Au@Pt from the two precursors (K_2PtCl_4 and $HAuCl_4$). Finally, the prepared products were washed several times with DI water and ethanol to remove the surfactant and reactants. We also

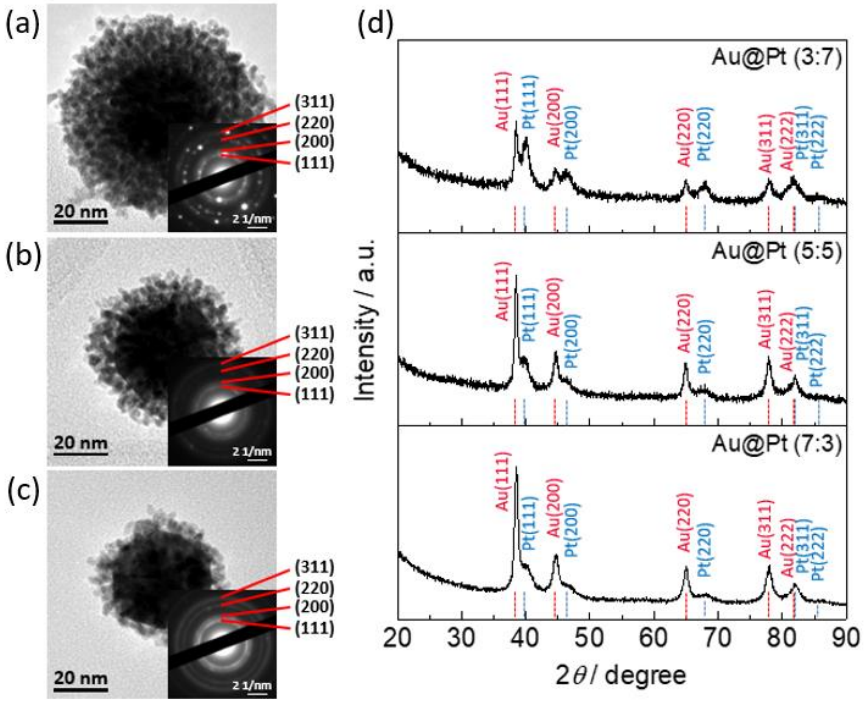

Figure 6.2. (a-c) TEM images of Au@Pt NPs with three different Au:Pt ratios (a) 3:7, (b) 5:5, and (c) 7:3, with the insets showing the corresponding SAED patterns. (d) Wide-angle XRD patterns of Au@Pt NPs with three different ratios (3:7, 5:5, 7:3).

confirmed the presence of NPs in solution by the Tyndall effect (right photographs of Figure 6.1). We argue that Pt and Au have different reduction kinetics and potentials [32], which result in the core-shell structure of the Au@Pt.

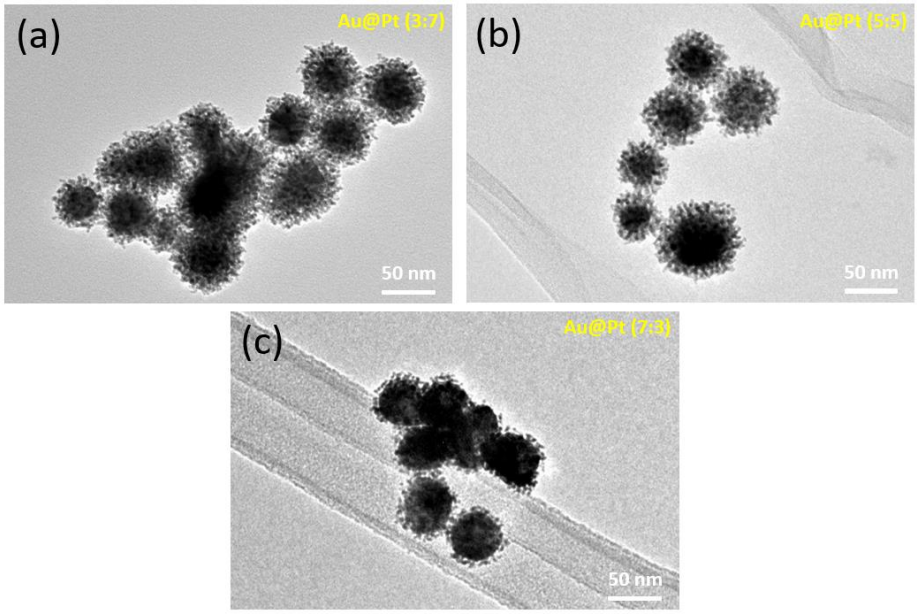

Figure 6.3. TEM images of different ration of Au@Pt NPs (a) 3:7, (b) 5:5, and (c) 7:3.

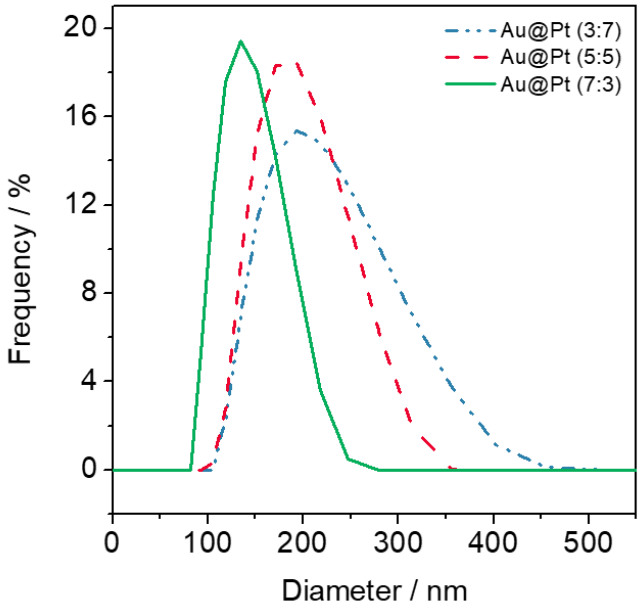

Figure 6.4. Particles size distribution analysis of Au@Pt NPs with three different Au:Pt Ratios (3:7 (blue, dash-dot-dot), 5:5 (red, dash), and 7:3 (green, solid)) by dynamic light scattering (DLS).

Different composite ratios of Au@Pt NPs were obtained at room temperature, and the formation of NPs with different sizes and shapes was confirmed using TEM (Figure 6.2 and Figure 6.3). The average diameters of the NPs obtained from different molar ratios of Au to Pt (3:7, 5:5, and 7:3) were estimated to be around 60, 52, and 47 nm, respectively, as can be seen in Figure 6.2a-c and 6.3. With increasing the Au ratio, the entire diameter gradually decreased. To further confirm the trend of size following by different Au:Pt ratios, particle size distribution of Au@Pt NPs with different Au:Pt ratios (3:7, 5:5, and 7:3) were obtained by dynamic light scattering (DLS), respectively (Figure 6.4). As the ratio of gold increased, it was confirmed once again that the size became smaller. In addition, SEM images showed that the Au@Pt NPs have the uniform size (Figure 6.5). In Figure 2a-c, we selected one particle which has the same size of Au core for comparing the thickness of Pt shells. The Au core shows negligible change, indicating that the Pt dendritic structures strongly affect the diameter of the core-shell structure. The selected area electron diffraction (SAED) patterns of the three kinds of Au@Pt NPs indicate that

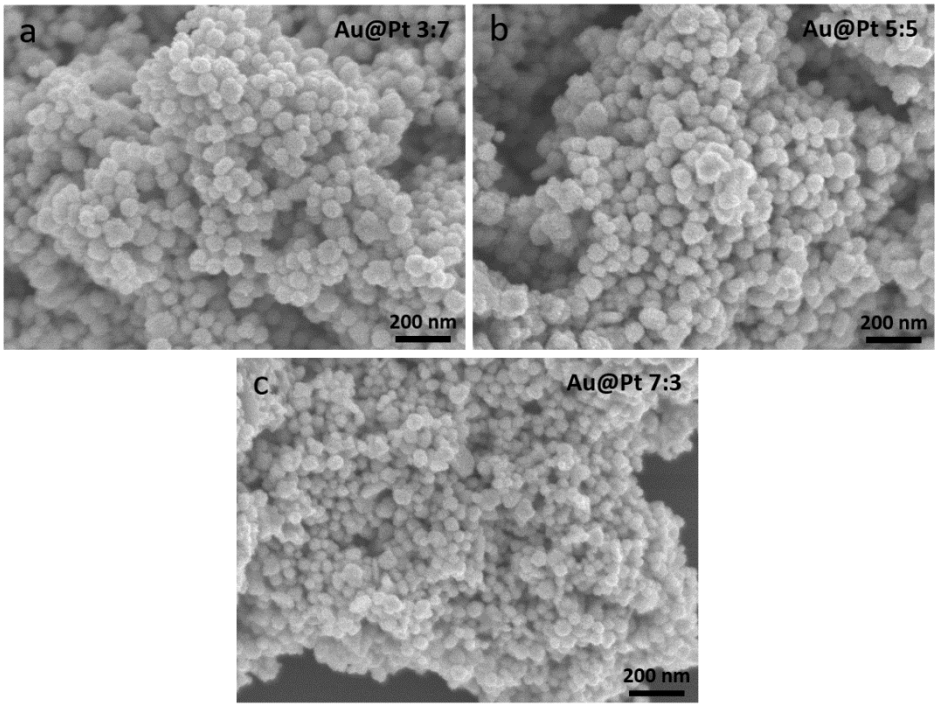

Figure 6.5. SEM images of Au@Pt NPs with three different Au:Pt ratios (a) 3:7, (b) 5:5, and (c) 7:3.

they have faced centred cubic (fcc) crystal structures (Figure 2a-c insets). Figure 2d shows the wide-angle XRD patterns for each ratio of Au@Pt NPs. The patterns for the Au@Pt NPs also indicate the fcc structure, which corresponds to several peaks from the (111), (200), (220), (311), and (222) planes. When the relative amount of Au increases, the Au peak intensity proportionally increases, which is obvious evidence that the ratios of the different types of Au@Pt NPs are different.

To further understand the distribution of Au to Pt, element mapping and line scans were performed on the Au@Pt NPs with the different molar ratios (Figure 6.4). We observed that Au is located in the centre (core) of the NPs, while Pt is located on the outer edge of the Au core (shell) in the form of dendritic arms. As the above TEM images showed, the particles ranged from 60 to 47 nm in size (Figure 6.3). In particular, the Au

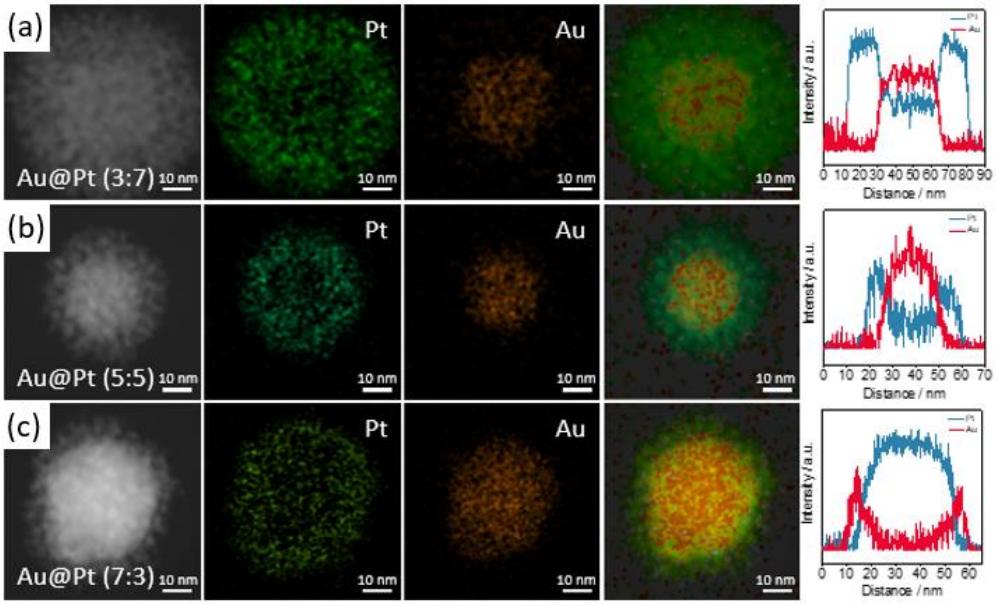

Figure 6.6. High-angle annular dark-field scanning transmission electron microscope (HAADF-STEM) images, corresponding elemental mappings, and line scans of Au@Pt NPs with different molar ratios: (a) 3:7, (b) 5:5, and (c) 7:3.

core size is estimated to be from 35 to 50 nm, and the thicknesses of the Pt shell are from 5 to 20 nm. Herein, the low intensity of the Au core in Au:Pt (3:7) is due to the greater

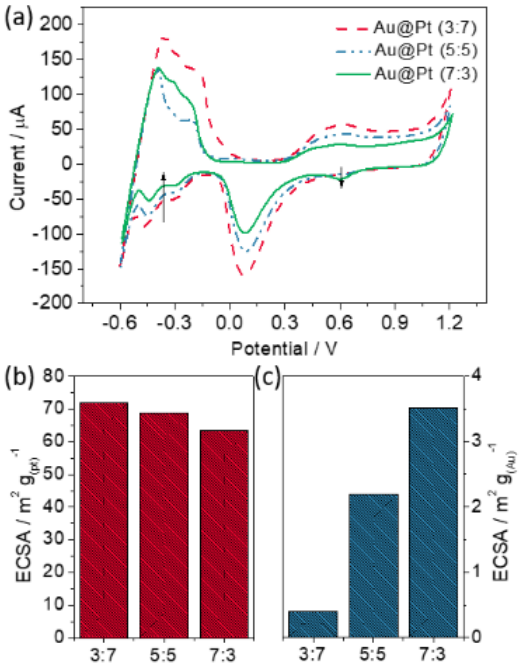

Figure 6.7. CVs and ECSAs for the three different ratios (3:7, 5:5, 7:3) of Au@Pt NPs. (a) CVs in 0.5 M H_2SO_4 (scan rate:100 mV s^{-1}), (b) ECSA from adsorption of H atoms, (c) ECSA from anodic peaks of Au.

thickness of the Pt dendritic shell. These results were also confirmed by line scanning of Au@Pt NPs. We confirmed that, as the content of Pt was decreased, the thickness of the Pt shell also was decreased.

To calculate the electrochemically active surface areas (ECSA), cyclic voltammograms (CVs) were recorded for Au@Pt (3:7, red, dashed), Au@Pt (5:5, blue, dashed), and Au@Pt (7:3, green, solid) NPs (Figure 6.5a). The CVs were recorded in 0.5 M sulfuric acid (H_2SO_4) solution from -0.6 V to +1.2 V at a scan rate of 0.1 V s^{-1}. The ECSAs determined from the H atom adsorption area are 8.92, 8.43, and 8.04 m^2 $g_{(Pt)}^{-1}$ for the NPs prepared with the three different molar ratios of Au to Pt (3:7, 5:5, and 7:3), respectively (Figure 6.5b). The ECSAs from anodic peaks of Au were 0.05, 0.11, and 0.37 m^2 $g_{(Au)}^{-1}$, respectively (Figure 6.5c). As the proportion of Au increases, the ECSA from the adsorption of H atoms decreases (Figure 6.6a), while the ECSA from anodic peaks of Au increases (Figure 6.6b). Furthermore, linear sweep voltammograms (LSVs) were recorded in 0.1M KOH (pH 13.0) and PBS (pH 7.4) solution containing 10 mM glucose, respectively (Figure 6.7). The oxidation peak currents in KOH solution (pH 13.0) for Au@Pt and Pt NPs were 30.3 and 26.77 μA, and the peak currents in PBS solution (pH 7.4) for Au@Pt and Pt NPs were 12.8 and 5.3 μA. Interestingly, AuNPs showed the

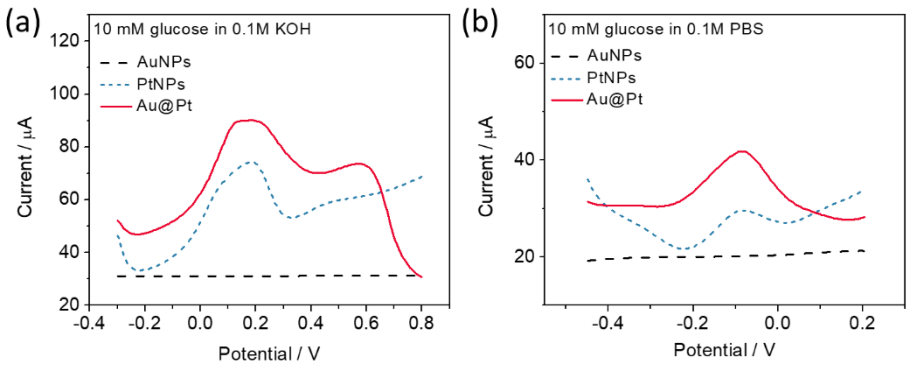

Figure 6.8. LSVs recorded for the electrodes: AuNPs/SPCE (dash line), PtNPs/AuNPs/SPCE (short dotted line), and Au@Pt/AuNPs/SPCE (solid line) in (a) 0.1 M KOH (pH 13) and (b) 0.1 M PBS (pH 7.4) containing 10 mM glucose, respectively.

very low oxidation current in the both solutions. As can be shown in Figure 6.7, our Au@Pt NPs show the highest response current for the catalytic oxidation of glucose in pH 7.4 solution compared with those of Pt and Au NPs.

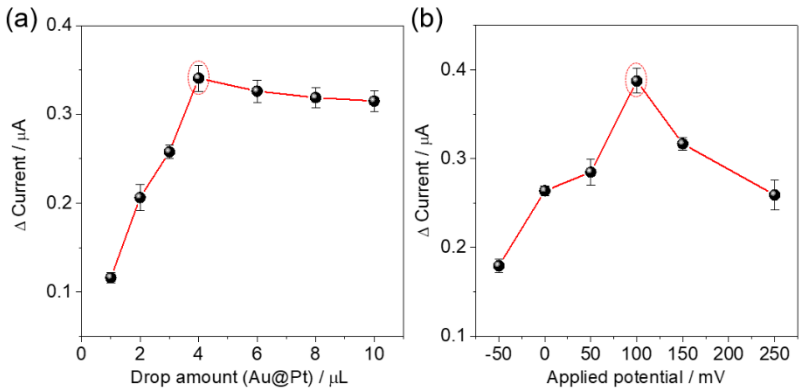

Figure 6.9. Optimization of Au@Pt NPs: (a) loading amount and (b) applied potential.

To determine the best content ratios of Au to Pt (3:7, 5:5, and 7:3), firstly, we optimized the Au@Pt drop-coating amount on the SPCE and the applied potential for electrochemical experiments (Figure 6.8). CVs were recorded in 0.1 M PBS solution containing 10 mM glucose (pH 7.4) (Figure 6.9a). During the anodic scan from - 0.8 V to + 0.4, the glucose oxidation peak was observed at - 0.09 V. The peak currents for each ratio (3:7, 5:5, and 7:3) were 3.28, 4.74, and 5.84 μA, respectively. As the content of Au increased, the current for the glucose oxidation peak also increased. In addition, the calibration plots obtained for the different glucose concentrations (from 0.1 to 100 mM)

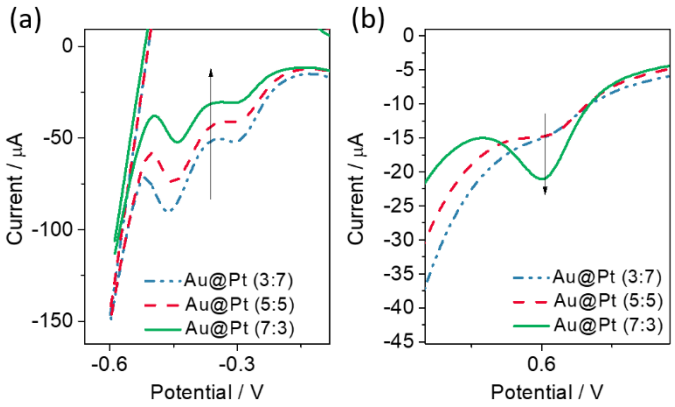

Figure 6.10. CVs of Au@Pt NPs with three different Au:Pt ratios (3:7, 5:5, 7:3): (a) adsorption of H atoms and (b) anodic peaks of Au.

indicated that the sensitivity of the Au@Pt (7:3) NPs (0.3765 μA μM 1) was 2.3 and 1.7 times higher than for the Au@Pt (3:7 and 5:5) NPs (0.2823 μA μM^{-1} and 0.1615 μA μM^{-1}), respectively (Figure 6.9b). As a result, we selected the Au@Pt (7:3) NPs for further study, because Au@Pt (7:3) was the best for the glucose oxidation reaction compared to other ratios. When the proportion of gold is higher than that of platinum, it is clear that the glucose oxidation reaction is also facilitated. The chronoamperometric (CA) response

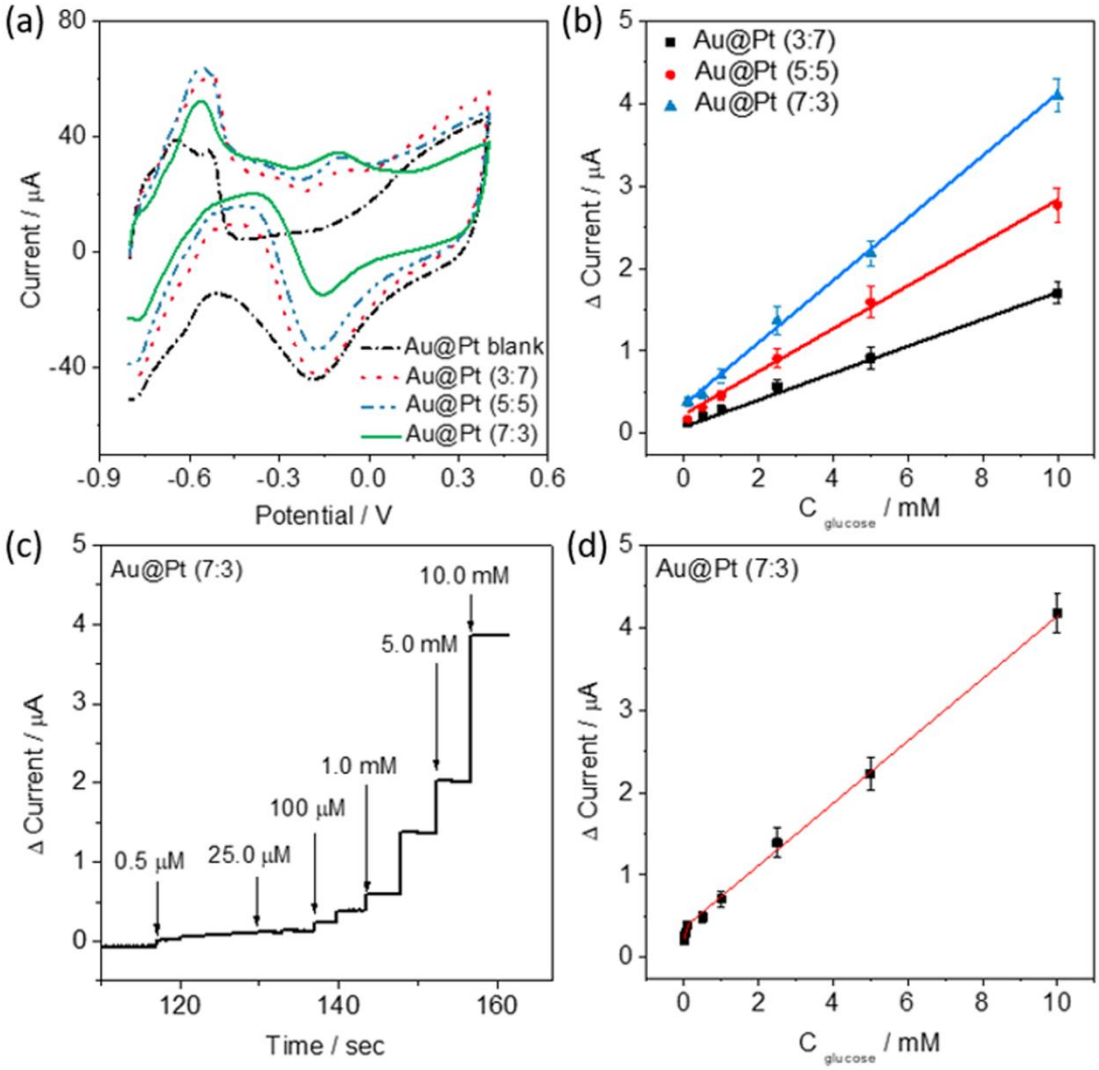

Figure 6.11. (a) CVs for Au@Pt NPs with three different Au:Pt ratios (3:7, 5:5, 7:3) recorded in 0.1 M PBS (pH 7.4) containing 10 mM glucose at a scan rate of 100 mV s^{-1}.(b) Calibration plots of modified electrodes: Au@Pt (3:7) (black line), Au@Pt (5:5) (red line), and Au@Pt (7:3) (blue line). (c) Amperometric response of Au@Pt (7:3) modified electrode to a wide range of glucose concentrations in 0.1 M PBS (pH 7.4), and (d) calibration plot of Au@Pt (7:3) modified electrode (applied potential: + 0.10 V (Ag/AgCl)).

of Au@Pt (7:3) NPs were observed in the range of glucose from 0.5 μM to 10.0 mM (Figure 6.9c). As the concentration of glucose increased, the peak current for the glucose oxidation also increased. Two dynamic ranges of the calibration plot were observed for the glucose detection, which are from 0.5 - 50.0 μM and 0.05 - 10.0 mM, with correlation coefficients of 0.9963 and 0.9788, respectively (Figure 6.9d). The detection limit (DL) of glucose was determined to be 319.8 (± 5.4) nM. Table 1 shows a comparison of our performance with the previous literature [33-36]. Therefore, Au@Pt (7:3) NPs can be highly useful as an electrode material for glucose detection.

Table 6.1. Comparison of the performance of our Au@Pt NPs with previous reports.

Materials	Methods	Detection Limit	Dynamic ranges	Reference
Core-shell structured Au@Pt	CA*	0.319 μM	0.5 - 50.0 μM and 0.05 - 10.0 mM	Our work
Nanoporous PtAu alloy	CA	~0.5 μM	Up to 5.4 mM	[33]
Mesoporous Pt-Au alloy films	CA	6.0 μM	6.0 μM - 11 mM	[34]
Bimetallic Pt-Au	CA	7.7 μM	0.01 - 7.5 mM	[35]
PtAu/C	CA	2.0 μM	1 - 10 mM	[36]

* Chronoamperometry (CA)

6.4 Conclusions

We have successfully synthesised Au@Pt nanoparticles (NPs) in different content ratios by the sonochemical method. Observations of the prepared Au@Pt NPs indicated that the Au is located in core, while the Pt is located in the outer shell. Interestingly, the thicknesses of the Pt shell regions were only changed by different content ratios. Based on XRD and TEM, these NPs display the metallic fcc structure. As the content of Pt decreased, the ECSA of Au increased, because the thickness of the Pt shell decreased.

With these samples, we demonstrated catalytic glucose oxidation using Au@Pt (3:7, 5:5, and 7:3 ratios) in neutral solution (pH 7.4). We observed that the Au@Pt (7:3) NPs revealed the best performance compared to the other ratios. The calibration curve using Au@Pt (7:3) NPs clearly shows two dynamic ranges for glucose concentrations ranging from 0.5 - 50.0 μM and 0.05 - 10.0 mM, with the detection limit of 319.8 (± 5.4) nM in neutral solution (pH 7.4). As a result, the Au@Pt (7:3) NPs can be used as the efficient glucose oxidation catalyst in neutral solution (pH 7.4), paving the way for practical application.

6.5 References

[1] B. Lim, Y. Xia, Angew. Chem. Int. Ed., 2011, **50**, 76-85.

[2] Z. Niu, N. Becknell, Y. Yu, D. Kim, C. Chen, N. Kornienko, G. A. Somorjai, P. Yang Nat. Mater., 2016, **15**, 1188-1195.

[3] S. M. Alia, K. O. Jensen, B. S. Pivovar, Y. Yan, ACS Catal., 2012, **2**, 858-863.

[4] K. Shim, J. Kim, M. Shahabuddin, Y. Yamauchi, M. S. A. Hossain, J. H. Kim, Sens. Actuators B-Chem., 2018, **255**, 2800-2808.

[5] D.-M. Kim, J.-M. Moon, W.-C. Lee, J.-H. Yoon, C. S. Choi, Y.-B. Shim, Biosens. Bioelectron., 2017, **91**, 276-283.

[6] H. He, X. Xu, H. Wu, Y. Jin, Adv. Mater., 2012, **24**, 1736-1740.

[7] J. A. Schuller, E. S. Barnard, W. Cai, Y. C. Jun, J. S. White, M. L. Brongersma, Nat. Mater., 2010, **9**, 193-205.

[8] S. Yang, X. Luo, Nanoscale, 2014, **6**, 4438-4457.

[9] K. Shim, J. Kim, Y.-U. Heo, B. Jiang, C. Li, M. Shahabuddin, K. C.-W. Wu, M. S. A. Hossain, Y. Yamauchi, J. H. Kim, Chem. Asian J., 2017, **12**, 21-26.

[10] A. Zaleska-Medynska, M. Marchelek, M. Diak, E. Grabowska, Adv. Colloid Interface Sci., 2016, **229**, 80-107.

[11] C. Galeano, J. C. Meier, M. Soorholtz, H. Bongard, C. Baldizzone, K. J. J. Mayrhofer, F. Schüth, ACS Catal., 2014, **4**, 3856-3868.

[12] Y. Song, C. Zhu, H. Li, D. Du, Y. Lin, RSC Adv., 2015, **5**, 82617-82622.

[13] J. Wu, K. Qin, D. Yuan, J. Tan, L. Qin, X. Zhang, H. Wei, ACS Appl. Mater. Interfaces, 2018, **10**, 12954-12959.

[14] L. Liu, E. Pippel, R. Scholz, U. Gösele, Nano Lett., 2009, **9**, 4352-4358.

[15] B. Lim, M. Jiang, P. H. C. Camargo, E. C. Cho, J. Tao, X. Lu, Y. Zhu, Y. Xia, Science, 2009, **324**, 1302-1305.

[16] B.-S. Choi, Y. W. Lee, S. W. Kang, J. W. Hong, J. Kim, I. Park, S. W. Han, ACS Nano, 2012, **6**, 5659-5667.

[17] K. Shim, J. Lin, M.-S. Park, M. Shahabuddin, Y. Yamauchi, M. S. A. Hossain, J. H. Kim, Scripta Materialia, 2019, **158**, 38-41.

[18] K. Shim, W.-C. Lee, M.-S. Park, M. Shahabuddin, Y. Yamauchi, M. S. A. Hossain, Y.-B. Shim, J. H. Kim, Sensors and Actuators B: Chemical, 2019, **278**, 88-96.

[19] Y. Xu, L. Chen, X. Wang, W. Yao, Q. Zhang, Nanoscale, 2015, **7**, 10559-10583.

[20] H. Y. Kim, S. Cho, Y. J. Sa, S.-M. Hwang, G.-G. Park, T. J. Shin, H. Y. Jeong, S.-D. Yim, S. H. Joo, Small, 2016, **12**, 5347-5353.

[21] G.-H. Wang, J. Hilgert, F. H. Richter, F. Wang, H.-J. Bongard, B. Spliethoff, C. Weidenthaler, F. Schüth, Nat. Mater., 2014, **13**, 293-300.

[22] Y. Huang, Y.-E Miao, S. Ji, W. W. Tjiu, T. Liu, ACS Appl. Mater. Interfaces, 2014, **6**, 12449-12456.

[23] S. H. Ahn, M. J. Klein, A. Manthiram, Adv. Energy Mater., 2017, **7**, 1601979.

[24] Y. Zeng, Z. Shao, H. Zhang, Z. Wang, S. Hong, H. Yu, B. Yi, Nano Energy, 2017, **34**, 344-355.

[25] X. Cao, N. Wang, Y. Han, C. Gao, Y. Xu, M. Li, Y. Shao, Nano Energy, 2015, **12**, 105-114.

[26] Y. Wang, M. Zhao, J. Ping, B. Chen, X. Cao, Y. Huang, C. Tan, Q. Ma, S. Wu, Y. Yu, Q. Lu, J. Chen, W. Zhao, Y. Ying, H. Zhang, Adv. Mater., 2016, **28**, 4149-4155.

[27] M. Rashid, T.-S. Jun, Y. Jung, Y. S. Kim, Sens. Actuators B-Chem., 2015, **208**, 7-13.

[28] S. J. Cho, H.-B. Noh, M.-S. Won, C.-H. Cho, K. B. Kim, Y.-B. Shim, Biosens. Bioelectron., 2018, **99**, 471-478.

[29] C. Huang, Y. Wu, J. Chen, Z. Han, J. Wang, H. Pan, M. Du, Electroanalysis, 2012, **24**, 1416-1423.

[30] D. Liu, Q. Guo, X. Zhang, H. Hou, T. You, J. Colloid Interface Sci., 2015, **450**, 168-173.

[31] C. Sumathi, C. V. Raju, P. Muthukumaran, J. Wilson, G. Ravi, J. Mater. Chem. B, 2016, **4**, 2561-2569.

[32] H. Ataee-Esfahani, L. Wang, Y. Nemoto, Y. Yamauchi, Chem. Mater., 2010, **22**, 6310-6318.

[33] J. Wang, H. Gao, F. Sun, C. Xu, Sens. Actuators B-Chem., 2014, **191**, 612-618.

[34] C. Li, H. Wang, Y. Yamauchi, Chem. Eur. J., 2013, **19**, 2242-2246.

[35] S. Nantaphol, T. Watanabe, N. Nomura, W. Siangproh, O. Chailapakul, Y. Einaga, Biosens. Bioelectron., 2017, **98**, 76-82.

[36] B. Singh, F. Laffir, T. McCormac, E. Dempsey, Sens. Actuators B-Chem., 2010, **150**, 80-92.

7. Au decorated core-shell structured Au@Pt for the glucose oxidation reaction

7.1 Introduction

Many kinds of catalytic materials have contributed to advanced technologies in many industrial and medical fields, which have received much attention due to their importance for human life [1]. Of these, metals and metal oxides (e.g. Pt, Au, Zn, Cu, Ni, CuO, TiO_2, and NiO_2) are especially crucial to catalyse heterogeneous electrocatalytic reactions for various redox compounds, where they have been used to promote the electrochemical reactions related to energy conversion devices and electrochemical sensors [2,3]. Pt and Au nanoparticles (NPs) in particular have been more widely studied as electrocatalysts for fuel cells [4] and for the oxidation of some biologically important organic molecules, such as glucose, ascorbic acid, and dopamine [5-9]. They have potential applicability as electrochemical sensor materials as well. Among the organic molecules, glucose is one of the most important target species, because it is closely related to human life and diseases, especially diabetes mellitus.

Diabetes mellitus is one of the foremost human diseases, since around 400 million people worldwide have diabetes related diseases, such as heart disease, kidney failure, and blindness [10-13]. Hence, the precise monitoring of blood glucose and its management are clinically important. In particular, it is essential to monitor the patient's glucose level in a timely manner using a robust portable sensor device. To detect glucose, various techniques were reported, such as chemiluminescence [14], electrochemiluminescence [15], electrochemical sensors [16]. Among them, electrochemical sensor devices are currently the best choice. They include enzymatic and

non-enzymatic types, and the enzymatic method has been the most widely used since it was first reported in 1962 [17]. Their accuracy is somewhat constrained, however, because the enzyme activity is dependent on temperature, humidity, and interference. For this reason, the non-enzymatic method has attracted considerable attention in recent years because of its low cost, rapid response, and exceptional sensitivity [18,19]. The sensing electrodes based on these materials, however, still have drawbacks such as poor stability, easy loss of activity, and surface poisoning from the adsorbed intermediates, especially at neutral pH. To overcome these disadvantages, it is most important to explore or synthesize alternative new sensor probe materials.

Glucose sensors using NPs have also been reported recently [20-23]. Many studies of sensing materials have demonstrated that the synergistic effects of bimetal or metal composites with other materials [24-28] can lead to improved sensing performance. Nonetheless, the glucose sensors using these materials are slowed down in practice because they mostly operate at basic pH values (limiting usage for in vivo and in vitro analysis). As a result, glucose detection at physiological pH is one of goals for the development of non-enzymatic sensors as well as the synthesis of a superior electrocatalytic material. Among the most efficient materials for this purpose are nanoporous metal particles, since nanoarchitectured porous materials have the advantages of unique shapes and properties, including large pore volume, high surface area, and well-controlled pores [28]. There are several methods that can be used to obtain porous materials, such as soft-templating and hard-templating [28]. Among the various porous materials, nanoporous Pt has aroused interest for various sensing applications because of its catalytic characteristic and huge number of pores.

Au is widely used as electrode materials for glucose sensors [29,30]. These still have some limitations, however, due to passivation by oxidation products or the reaction with chloride ions in neutral solutions, resulting in a poor response to glucose oxidation. One of possible ways to reduce this is to synthesize bimetal NPs combining synergetic properties. Hence, some studies have been reported on bimetallic alloys or composites revealing synergistic effects [31,32], which can achieve improved sensing performance. The bimetallic NPs feature fast electrochemical oxidation and a unique synergistic contribution, which enhance conductivity and accelerate electron transfer. Thus, we expected an increased catalytically active area through the formation of a new morphology of nanoporous Au-Pt bimetallic NPs, in which abundant nano-channels are formed by the Pt shell layers on the Au cores. Additional Au deposition inside the nano-channels of Pt shells can further raise expectations of much improved catalytic activity, resulting in enhanced sensitivity towards glucose detection even in a chloride containing sample solution. Therefore, we studied Au nanoparticle-doped Pt nano-channels formed on AuNPs.

In the present work, as a proof-of-concept, we have synthesized Au@Pt core-shell NPs with different ratios of the constituents by previously reported methods [33]. In addition, small amounts of Au particles were deposited onto the surface of Au@Pt core-shell NPs. To characterize the Au@Pt/Au bimetallic NPs, transmission electron microscopy (TEM) and X-ray diffraction (XRD) were employed. The sensor performance of the obtained Au@Pt/Au modified electrode was examined by cyclic voltammetry (CV) and amperometry. We also conducted optimization of the analytical parameters for glucose detection, the interference effects of foreign species, and real sample analysis.

7.2 Experimental

Reagents and materials: Potassium tetrachloroplatinate(II) (K_2PtCl_4, 98%), gold(III) chloride trihydrate ($HAuCl_4 \cdot 3H_2O$, ≥ 99.9% trace metals basis), polyethylene glycol hexadecyl ether (Brij 58®, $HO(CH_2CH_2O)_{20}C_{16}H_{33}$), D-(+)-glucose, uric acid (UA), acetaminophen (AP), dopamine (DA), ascorbic acid (AA), sodium chloride, and Nafion® (NF), were purchased from Sigma-Aldrich Co. (USA). A 0.1 M phosphate buffer solution (PBS) was prepared using 0.1 M sodium dihydrogen phosphate and 0.1 M disodium hydrogen phosphate (Sigma-Aldrich Co. USA), and the 0.1M PBS saline (PBS_{sal}) solution was prepared by adding 0.1 M NaCl. All aqueous solutions were prepared in doubly distilled water, which was obtained from a Milli-Q water-purifying system (18 MΩ cm).

Preparation of core-shell Au@Pt NPs: K_2PtCl_4 (20 mM) and $HAuCl_4$ (20mM) were prepared as stock solutions. Three different ratios (3:7, 5:5, 7:3) of Au to Pt content were prepared for a final volume of 5 ml for the mixed solution. The solution was mixed with Brij 58® (0.05 g) in a vial, and 5.0 mL of AA solution (0.1 M) was added and mixed in. We used the optimized Brij and AA concentrations reported in previous works [33,34]. This solution was reacted at room temperature for 1 hour with ultrasonication (220-240 V, 50-60 Hz). The precipitates were collected by centrifugation and washed several times with deionized (DI) water and ethanol to remove the surfactant and excess reactants.

Preparation of Au@Pt/Au NPs: 4 µL of the above-prepared Au@Pt NPs solution (1 mg mL^{-1}) was dropped onto an AuNPs modified screen-printed carbon electrode (SPCE), and it was dried at 40 ℃. The Au@Pt NPs modified electrode was dipped in the Au plating solution containing citric acid, ethylenediamine tetraacetic acid (EDTA), and $KAu(CN)_2$. Au was incorporated into the porous Pt channels of the Au@Pt electrode using a potential

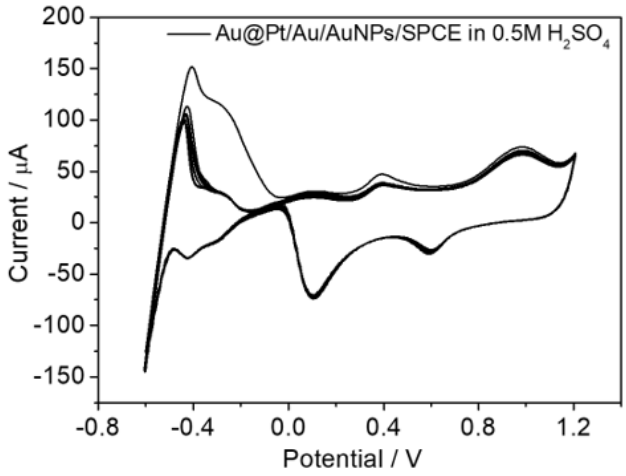

Figure 7.1. CVs recorded for Au@Pt/Au NPs modified AuNPs/SPCE in 0.5 M H_2SO_4 solution.

step method. The potential of - 1.0 V was applied over 10 s. For the pre-activation, cyclic voltammograms (CVs) were recorded for the modified electrode in the range of - 0.6 V to + 1.2 V (vs. Ag/AgCl) at the scan rate of 0.1 V s^{-1} in a 0.5 M sulfuric acid (H_2SO_4) solution. (Figure 7.1).

Analytical procedure: The analysis of glucose using the proposed sensor probe was performed in 0.1 M PBS and PBS_{sal} (pH 7.4) solutions and whole blood samples (five volunteers). The quantitative analysis of glucose in 0.1 M PBS and PBS_{sal} (pH 7.4) solutions and whole blood samples was based on the oxidation current response of glucose. A chronoamperometric experiment was carried out at applied potential of + 0.10 V and + 0.35 V (vs. Ag/AgCl) with various glucose concentrations (0.5 μM - 10.0 mM) in 0.1 M PBS and PBS_{sal} (pH 7.4) solutions. For human whole blood samples, the blood was diluted five times with a 0.1 M PBS_{sal} (pH 7.4) solution to minimize the matrix effects. The amperometric responses were then recorded under the optimized experimental conditions.

Instruments: The screen-printed carbon electrodes (SPCEs) were used carbon, Ag/AgCl, and carbon as the working, reference, and counter electrodes, respectively. A solid-state

Ag/AgCl reference electrode was prepared according to a previous report [35]. The electrodes were printed on a polystyrene-based film with carbon and silver inks (Jujo Chemical, Japan) employing a screen printer (Bando Industrial, Korea). Amperograms and cyclic voltammograms (CVs) were recorded using a potentiostat/galvanostat, a Kosentech Model PT-1 and an EG & G PAR Model PAR 273A, respectively. The morphology and structure of the Au@Pt and Au@Pt/Au NPs were observed using transmission electron microscopy (TEM; H-7600 (HITACHI) and JEOL-2100, Japan), and energy-filtering TEM (EFTEM; Carl Zeiss, microscope operated at 120 kV) for high-resolution studies. The atomic ratios of the porous structured NPs and elemental mapping were evaluated by energy dispersive X-ray spectroscopy (EDX). Wide-angle powder XRD patterns were obtained with a GBC MMA XRD at a scan rate of 2° min^{-1}. A quartz crystal microbalance (QCM) experiment was conducted using a SEIKO EG&G model QCA 917 and a PAR Model 263A potentiostat/galvanostat. The QCM experiment was conducted using an Au-coated working electrode (area: 0.196 cm^2; 9 MHz; AT-cut quartz crystal).

7.3 Results and discussion

As shown in Scheme 7.1, Au@Pt/Au NPs were prepared in two steps using the sonochemical and electrodeposition methods. At the first step, core-shell Au@Pt NPs were synthesized using the sonochemical method. Ascorbic acid was used as a reducing agent to obtain bimetal NPs from the two precursors, K_2PtCl_4 and $HAuCl_4$, which have different reduction potentials. Since the reduction potential of $AuCl_4^-$ (E^o = + 1.0 V) is higher than that of $PtCl_4^{2-}$ (E^o = + 0.73 V), the nucleation of Au ions is faster and easier than that of Pt ions. Due to this, the reduction of Au ions preferentially forms Au cores as

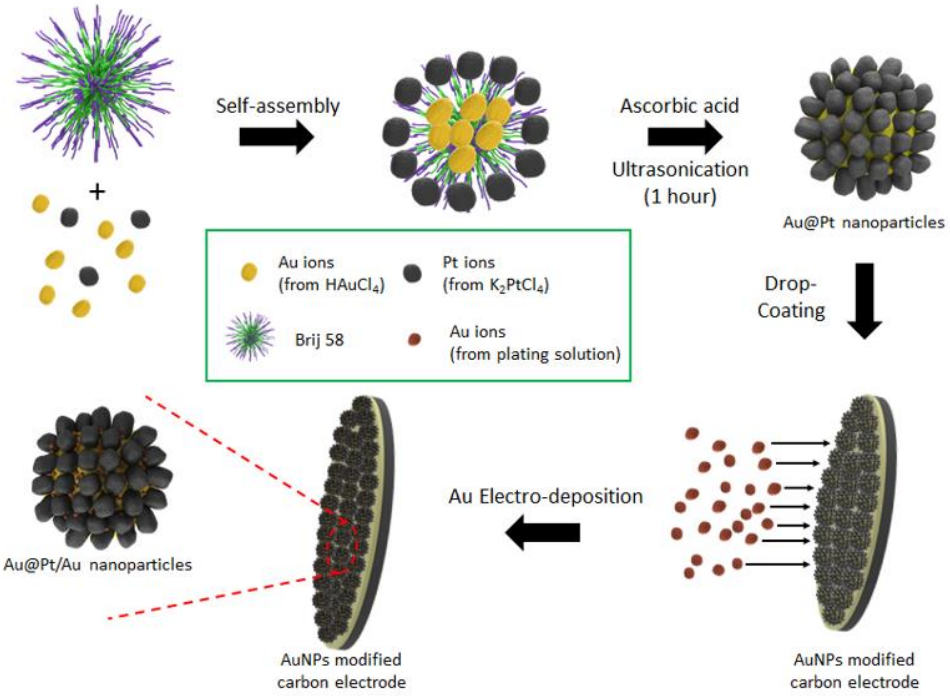

Shceme 7.1. Schematic illustration of the synthesis of Au@Pt/Au NPs.

seeds in a short time, and then, Pt NPs grow onto the Au core seeds. Brij plays an important role as a structure-directing agent for the formation of the nanomaterials with AA [33,34]. In the second step, additional AuNPs were incorporated into the porous Pt shells of the Au@Pt NPs using the potential step method. Here, both Au@Pt and Au@Pt/Au NPs were characterized in terms of their nanostructures and catalytic activity towards glucose oxidation.

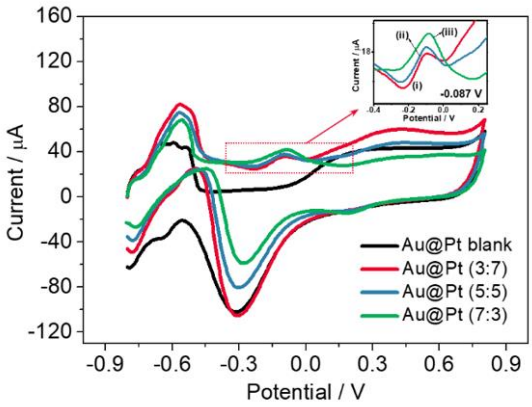

Figure 7.2. CVs recorded for bimetallic Au@Pt nanoparticle modified electrode in 0.1 M PBS (pH 7.4) solution containing 10 mM glucose, with Au:Pt ratios of (i) 3:7, (ii) 5:5, and (iii) 7:3.

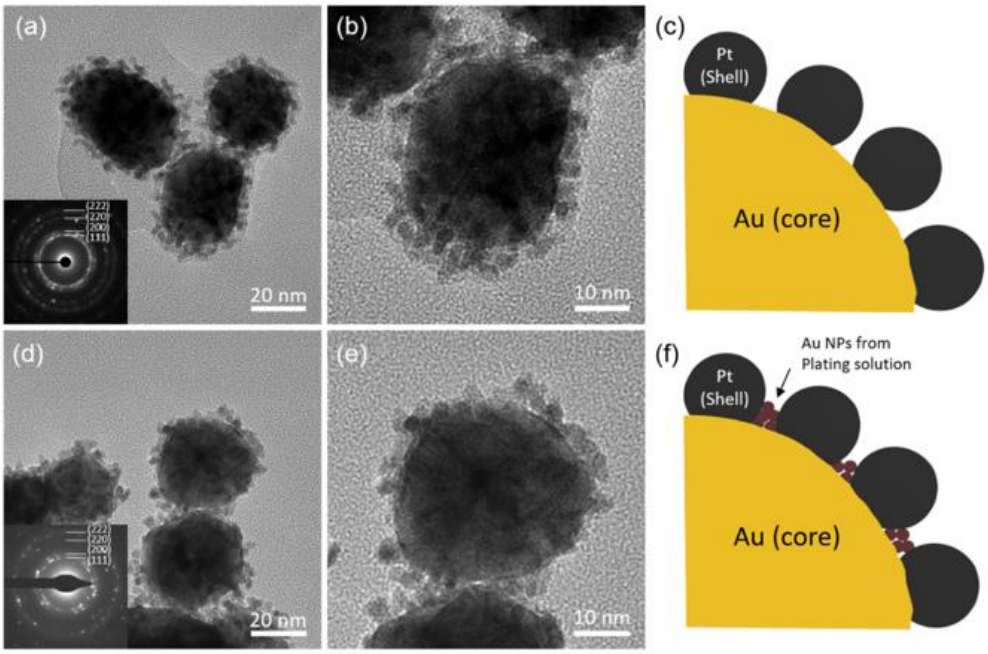

Figure 7.3. Morphologies of Au@Pt and Au@Pt/Au NPs: (a),(b) TEM images of Au@Pt (inset in (a): corresponding SAED pattern); (c) schematic illustration of Au@Pt NPs; (d),(e) TEM images of Au@Pt/Au (inset in (d): corresponding SAED pattern); (f) schematic illustration of Au@Pt/Au NPs.

At first, to determine the optimum content ratio of Au to Pt, the oxidation peak current of glucose was observed by CV in a 0.1 M PBS (pH 7.4) solution containing 10 mM glucose (pH 7.4). Figure 7.2 shows the CVs recorded for glucose oxidation according to the content ratio of Au to Pt in Au@Pt. During the anodic scan from - 0.8 to + 0.8 V, the glucose oxidation peak appeared at - 0.09 V. The peak currents for each Au to Pt ratio (3:7, 5:5, 7:3) were 3.24, 4.12, and 5.33 μA, respectively. As the content of Au increased, the glucose oxidation peaks current also increased. Accordingly, we selected the ratio of Au to Pt of 7:3 as the best performer and used it for the subsequent experiments.

To further investigate the characteristics of the particles, the shape, size, and crystalline structure of Au@Pt and Au@Pt/Au NPs were studied by TEM, as can be seen in Figure 7.3. The growth of a dendritic porous Pt layer on Au core was confirmed by the TEM images. The Pt nanoparticle layer consisted of 2-4 nm particles. From the TEM images of Au@Pt NPs, it is clear that the Au core particles are surrounded by the dendritic

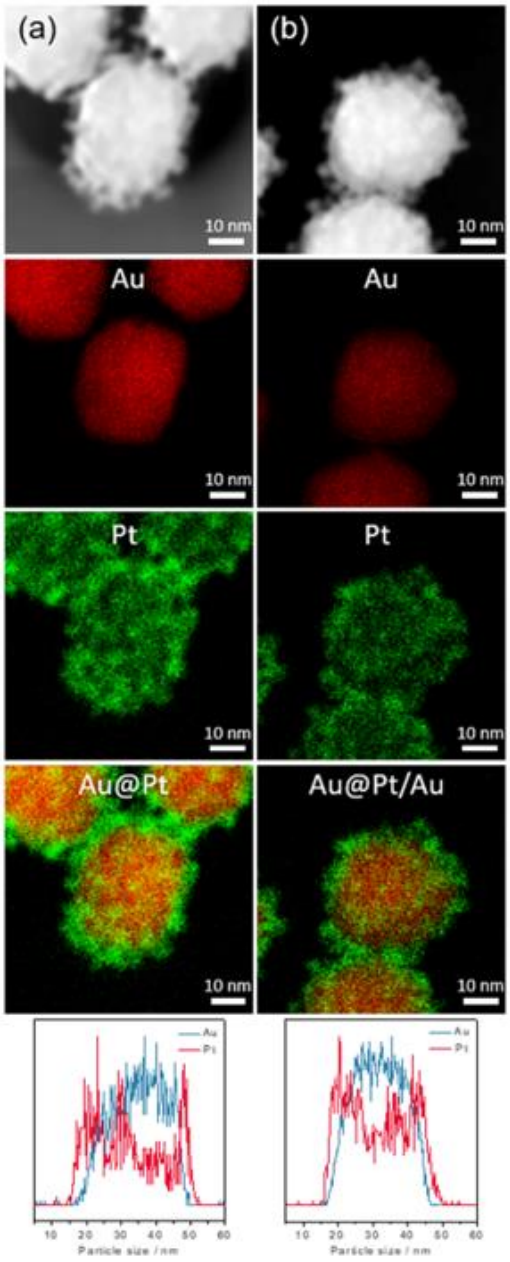

Figure 7.4. (a) High-angle annular dark-field scanning transmission electron microscope (HAADF-STEM) image, corresponding elemental mapping, and line scans of Au@Pt NPs, (b) HAADF-STEM image, elemental mapping, and line scans of Au@Pt/Au NPs.

Pt shells, which is evidence of core-shell NPs. The selected area electron diffraction (SAED) patterns of Au@Pt and Au@Pt/Au NPs confirmed the face-centred-cubic (fcc) crystal structure of metals, with the concentric rings arising from the (111), (200), (220), and (222) planes (insets of Figure 7.3a and d). The diameters of the obtained Au@Pt (Figure 7.3a and b) and Au@Pt/Au NPs (Figure 7.3d and e) were in the range from 35 to

60 nm. There was no big change in the particle size after Au incorporation, indicating the formation of very tiny Au layers on the Au core (Figure 7.3c and f). For better understanding, elemental mapping and line scanning were performed on the Au@Pt and Au@Pt/Au NPs (Figure 7.4). The elemental mapping of the Au@Pt NPs indicated that most of the Au content was concentrated in the particle centre, whereas Pt was located on the outer edge of the Au particle. This is also supported by the line scans of Au@Pt NPs

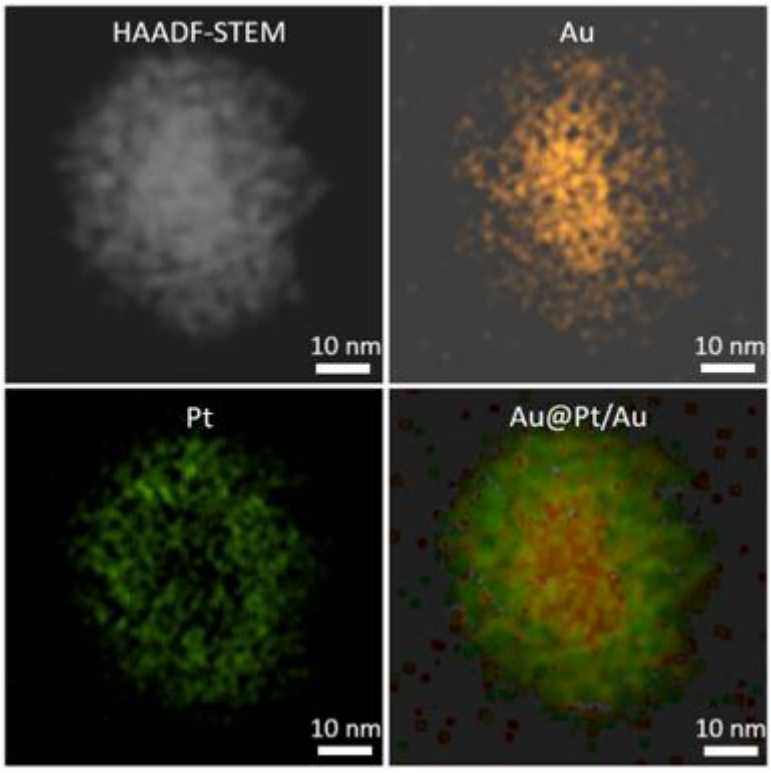

Figure 7.5. High-angle annular dark-field scanning transmission electron microscope (HAADF-STEM) image with corresponding elemental mapping of Au@Pt/Au NPs.

(Figure 7.4a). Figure 7.4b shows the elemental mapping and line scans of Au@Pt/Au NPs. The elemental mapping results for Au@Pt/Au NPs indicated that the Au elemental distribution had grown compared to the Au@Pt result. Complementary mapping images of Au deposited onto the Au@Pt NPs were also performed. As can be seen in Figures 7.4 and Figure 7.5, the shell thickness of Pt arms is almost the same for the two samples. After additional Au is deposited, however, the signal of Au element is observed from the

outer shell. This data provides evidence that additional Au deposition was successfully achieved inside the Pt shell region. The crystalline structures and degrees of crystallinity of Au@Pt and Au@Pt/Au NPs were further investigated by wide-angle XRD measurements (Figure 7.6). For reference, Pt NPs were also measured. The pattern of the Pt NPs shows several peaks from the (111), (200), (220), (311), and (222) planes, which are indexed to face-centred cubic (fcc) Pt. In contrast, the patterns of the Au@Pt and Au@Pt/Au NPs indicate the presence of both Au and Pt crystals with fcc structures. After additional Au deposition, the Au peak intensities relative to the Pt peak intensities are slightly stronger.

To determine the electrochemically active surface areas (ECSAs), CVs were obtained for Pt (dashed line), Au@Pt (dotted line), and Au@Pt/Au (solid line) NPs on AuNPs treated on screen-printed carbon electrode (SPCE) (Pt/AuNPs/SPCE, Au@Pt/AuNPs/SPCE, and Au@Pt/Au/AuNPs/SPCE). In this case, the CVs were recorded in 0.5 M sulfuric acid (H_2SO_4) solution from -0.6 V to +1.2 V at a scan rate of 0.1 V s^{-1} (Figure 7.7a). A pair of redox peaks representing the adsorption of H atoms was

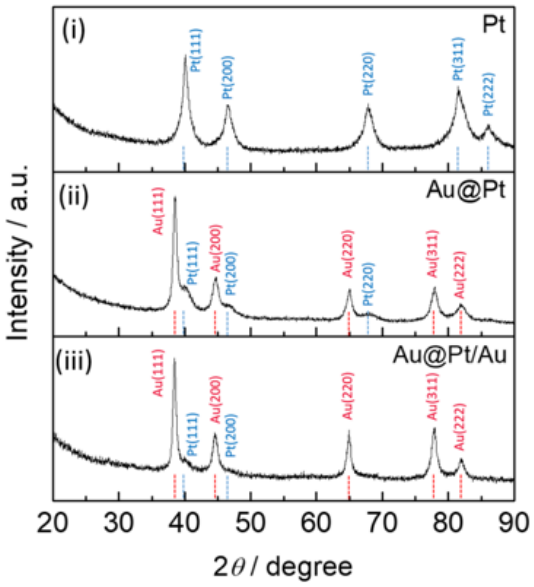

Figure 7.6. Wide-angle XRD spectra of the (i) Pt, (ii) Au@Pt, and (iii) Au@Pt/Au NPs.

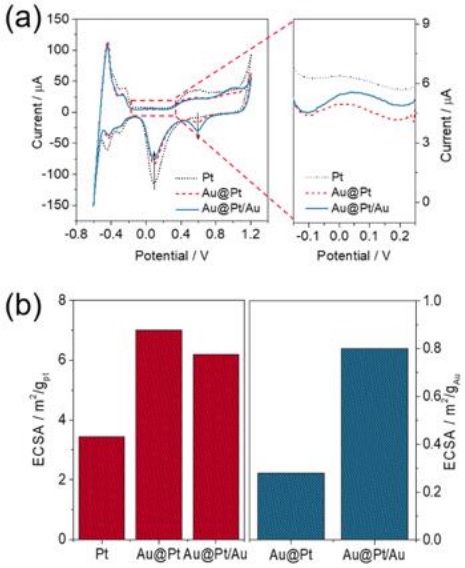

Figure 7.7. (A) CVs of the Pt (dotted line), Au@Pt (dashed line), and Au@Pt/Au NPs (solid line), and (B) ECSAs of Au@Pt and Au@Pt/Au in 0.5 M H_2SO_4 (scan rate:100 mV s^{-1}).

observed between - 0.6 V and - 0.2 V. Otherwise, the anodic peaks of Au were observed at + 0.06 V and + 0.98 V, respectively, which correspond to the formation of $Au(OH)_3$ and Au_2O_3 from Au. Pt was oxidized to PtO_2 at + 0.44 V during the anodic scan. In the reverse cathodic scan, the reduction peaks of Au_2O_3 and PtO_2 formed during the anodic scan were observed at + 0.59 V and + 0.09 V, respectively. To calculate the ECSA of Au@Pt/Au, quartz crystal microbalance (QCM) analysis was conducted to determine the amount of AuNPs incorporated on the Au@Pt NPs-modified electrode over 10 s based on the frequency change (Δf), as shown in Figure 7.8. During incorporation of AuNPs on the Au@Pt, the frequency gradually decreased. In this case, the overall Δf was 37.0 Hz, which corresponded to a mass change (Δm) of 20.2 ng according to a previously reported equation [36]. The ECSAs of the Pt, Au@Pt, and Au@Pt/Au NPs were compared, as shown in Figure 7.7b. The Au@Pt NPs deposited on the electrode are very attractive for glucose oxidation. For better sensor performance, additional AuNPs were deposited on spaces between the outer Pt arms to further increase the density of catalytic sites (Au@Pt/Au). The ECSA in the H atom-adsorption area of Pt is 3.44 m^2 $g_{(Pt)}^{-1}$, while the

values for Au@Pt and Au@Pt/Au are 7.01 and 6.19 m^2 $g_{(pt)}^{-1}$, respectively. The ECSAs of Au@Pt and Au@Pt/Au are larger than for Pt, and the results for the Au@Pt and Au@Pt/Au NPs give higher hydrogen adsorption/desorption currents compared to the Pt. Therefore, the formation of the heterogeneous structure provides a large active surface area. The ECSAs of Au in Au@Pt and Au@Pt/Au NPs are 0.28 and 0.8 m^2 $g_{(Au)}^{-1}$, respectively. This result reveals that the active surface area of Au is increased by 2.85 times via a small amount of Au deposition. This means that Au ions were successfully deposited on spaces between the outer Pt arms. It was expected that the sensor performance would be improved.

In addition, to confirm the electrochemical surface charges of each modified layer, the CVs were recorded in a 4 mM potassium ferricyanide(III) ($K_3[Fe(CN)_6]$) solution

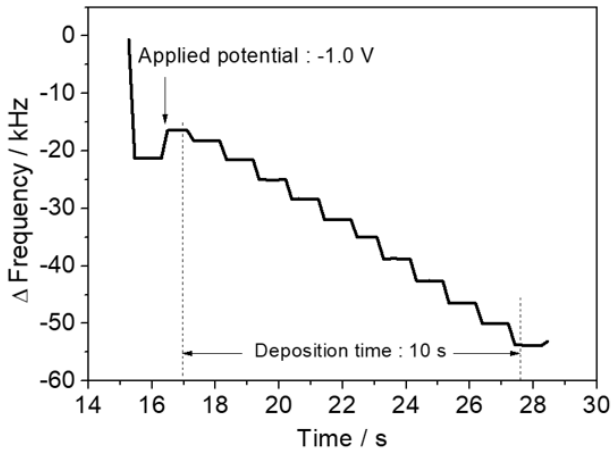

Figure 7.8. Frequency changes during the electrodeposition of Au solution on an Au@Pt modified electrode.

between - 0.5 V and + 0.6 V (Figure 7.9a) and in a 4 mM hexaammineruthenium(III) chloride ($Ru(NH_3)_6Cl_3$) solution between + 0.1 and - 0.7 V (Figure 7.9b). In both cases, the CVs were recorded for bare SPCE, and for Au@Pt/Au NPs, Au@Pt/Au/AuNPs, and Nafion/Au@Pt/Au/AuNPs layers on SPCE at a scan rate 0.1 V s^{-1}. The redox current of the Au@Pt modified electrode (red dotted line) increased in both ferricyanide and

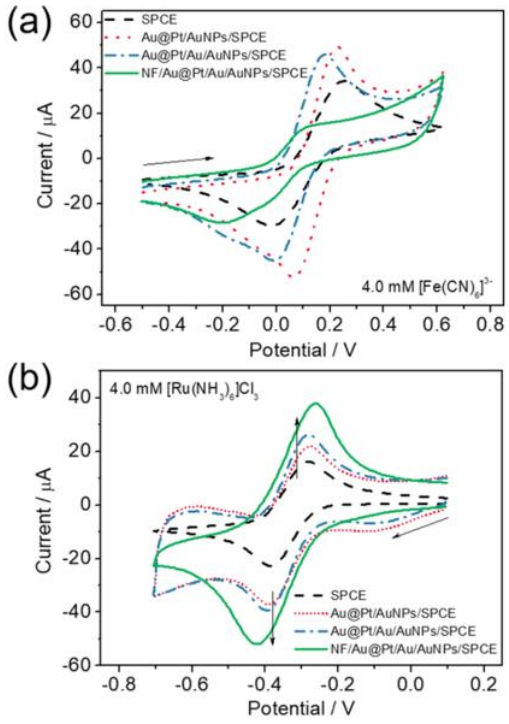

Figure 7.9. CVs obtained in solutions containing (a) 4.0 mM $[Fe(CN)_6]^{3-}$ and (b) 4.0 mM $[Ru(NH_3)_6]Cl_3$ using bare SPCE (black dashed line), Au@Pt/AuNPs/ SPCE (red dotted line), Au@Pt/Au/AuNPs/SPCE (blue dash-dotted line), and Nafion/Au@Pt/Au/AuNPs/SPCE (green solid line).

ruthenium solutions compared to the bare layer. Although the current values for the Au@Pt electrode increased compared to the bare SPCE, this was due to the increase in active sites on electrode surfaces. This increase in current values is not related to the reactions of the negative and/or positive charges because the Pt layer is highly porous. The CV shows that the redox peak current of Au@Pt/Au (blue dash-dotted line) slightly decreases in ferricyanide solution, while the redox peak current slightly increases in the solution containing positively charged ruthenium ions. This means that Au@Pt/Au has more negative charges compared to Au@Pt. This phenomenon became more obvious when 0.5 % Nafion® film was used as the protective layer, because the polymer film has negative charges.

To evaluate the electrochemical properties of the proposed sensor, various control experiments were carried out. At first, CVs were recorded for (a)

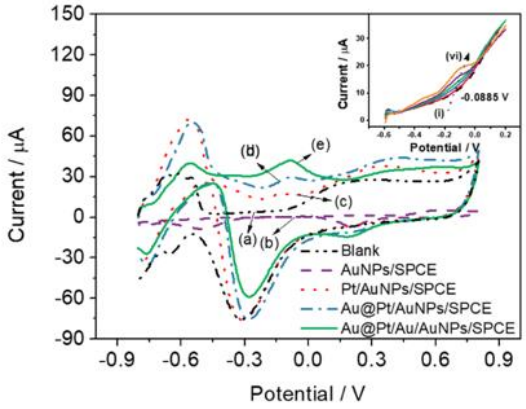

Figure 7.10. CVs recoded for (a) Au@Pt/Au/AuNPs/SPCE (dash dotted dotted line) (blank), (b) AuNPs/SPCE (dash line), (c) Pt/AuNPs/SPCE (dotted line), (d) Au@Pt/AuNPs/SPCE (dash-dotted line), and (e) Au@Pt/Au/AuNPs/SPCE (solid line), where (a) without and (b-e) with 10 mM glucose in 0.1 M PBS (pH 7.4) at a scan rate of 100 mV s^{-1}. Linear sweep voltammograms (LSVs) recorded for Au@Pt/Au/AuNP/SPCE in 0.1 M PBS (pH 7.4) containing 0.1 - 10.0 mM glucose.

Au@Pt/Au/AuNPs/SPCE (dash dotted dotted line) (Blank), (b) AuNPs/SPCE (dash line) (c) Pt/AuNPs/SPCE (dotted line), (d) Au@Pt/AuNPs/SPCE (dash-dotted line), and (e) Au@Pt/Au/AuNPs/SPCE (solid line) in 0.1 M PBS (pH 7.4) containing (a) without and (b-e) with 10 mM glucose from - 0.8 V to + 0.8 V, as shown in Figure 7.10. The CV curves showed a glucose oxidation peak at - 0.09 V. For the CV of AuNPs/SPCE, the signal is negligible with respect to the glucose oxidation. The purpose of using AuNPs modified SPCE is to enhance the electrical conductivity of the carbon electrode. Glucose oxidation currents of all the materials (Pt, Au@Pt, and Au@Pt/Au) were measured as ΔI: 2.13 µA, ΔI: 5.30 µA, and ΔI: 13.66 µA, respectively. The highest response for glucose oxidation was observed for the Au@Pt/Au NPs modified electrode, because AuNPs were incorporated into the nano-channels between the Pt particle layer and the Au core, which enhanced the active surface area. The inset in Figure 7.10 shows the glucose oxidation peak for Au@Pt/Au recorded in 0.1 M PBS (pH 7.4) solution containing various concentrations of glucose (0.1 - 10.0 mM). As the glucose concentration (0.1 - 10.0 mM) increases, the glucose oxidation current increases at - 0.09 V. Furthermore, to demonstrate

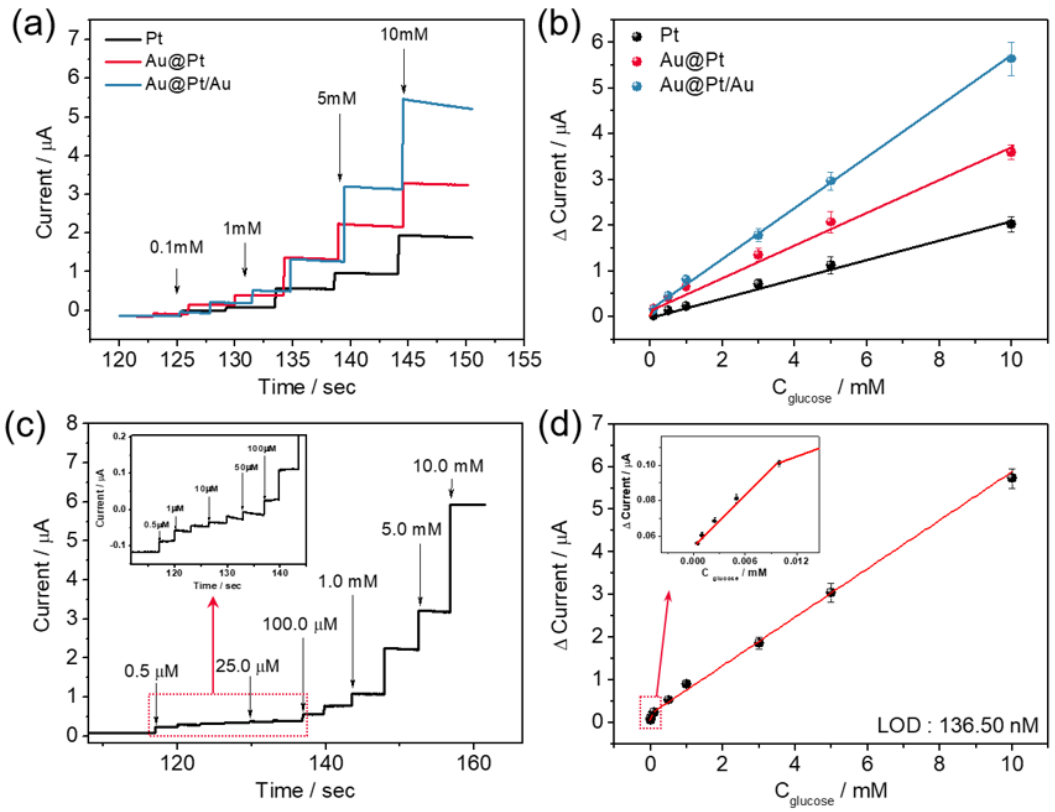

Figure 7.11. (a) Amperometric responses to successive additions of glucose in 0.1 M PBS (pH 7.4) and (b) calibration plots of different kinds of modified electrodes: Pt (black line), Au@Pt (red line), and Au@Pt/Au (blue line). (c) Amperometric response to a wide range of glucose concentrations in 0.1 M PBS (pH 7.4), and (d) corresponding calibration plot of Au@Pt/Au modified electrode (applied potential: + 0.10 V (Ag/AgCl)).

the electrode performance of each material, the chronoamperometric responses of the Pt (black line), Au@Pt (red line), and Au@Pt/Au (blue line) modified electrodes were recorded in a 0.1 M PBS (pH 7.4) solution containing glucose (Figure 7.11a). There was a linear relationship between the glucose concentration (from 0.1 to 100 mM) and the response current (the potential applied at + 0.1 V). In addition, the calibration plots showed that the sensitivity of the Au@Pt and Au@Pt/Au modified electrodes (slope = 0.3654 and 0.5755 µA mM^{-1}) (red and blue) was 1.6 and 2.7 times higher, respectively, compared to the Pt modified electrode (slope = 0.2205 µA mM^{-1}) (black) (Figure 7.11b). This result indicates that the glucose oxidation on the Au@Pt/Au electrode was the best in 0.1 M PBS (pH 7.4) solution. Figure 7.11c shows the amperometric response of the

Au@Pt/Au modified electrode depending on the glucose concentration. The glucose oxidation current increased (applied potential at + 0.1 V) as the concentration of glucose (from 0.5 µM to 10.0 mM) increased. The calibration plot with two slopes displays the dynamic ranges of 0.5 - 10.0 µM and 0.01 - 10.0 mM of glucose with respective correlation coefficients of 0.99 (Figure 7.11d). The linear regression equations for the peak currents in these ranges are ΔI_p (µA) = 4.79066 (± 0.20627) + 0.05423 (± 0.00085) [C] (mM) and ΔI_p (µA) = 0.6081 (± 0.01766) + 0.1101 (± 0.0039) [C] (mM), respectively. The detection limit (DL) of glucose was based on five measurements for the standard deviation of the blank noise (95% confidence level, signal to noise ratio, k = 3). The DL was assessed by linear regression of the calibration curve applying the following equation DL= 3 σ/m where σ is the standard deviation of the intercept and m is the slope and was determined to be 136.5 (± 8.4) nM.

Au-based non-enzymatic glucose sensors have a major problem, however, with decreasing surface activity in solutions with neutral pH and in the presence of chloride ions. The chloride ions react with the gold surface, which greatly decreases the Au active sites. As a result, the glucose response is significantly decreased [37,38]. To avoid this phenomenon, the bimetallic core-shell structure and a Nafion layer were selected to prevent passivation of Au core. The selectivity and sensitivity of the proposed method was due to the synergistic catalytic effect of Au core and Pt shell. In addition, Au core was employed as highly active catalytic material toward glucose oxidation whereas Pt shell was used to produce nano-channel to decrease the interference effect by various molecules specially, chloride ions. The electrodeposited AuNPs were penetrated into the nano-channel of Pt shell, which increased the active surface of Au core, ultimately enhanced the sensitivity of the sensor. Glucose responses were monitored in 0.1 M PBS

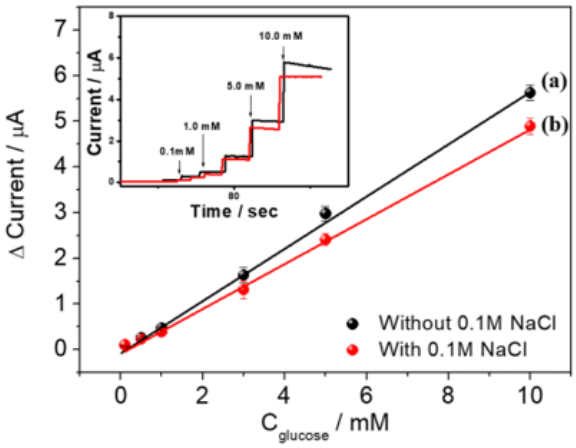

Figure 7.12. Comparative calibration plots showing the effect of chloride ions on the Nafion/Au@Pt/Au/AuNPs/SPCE sensor, while the inset shows the amperometric response.

and 0.1 M PBS_{sal} (pH 7.4) solutions, respectively (Figure 7.12). In addition, the Nafion layer was intended to protect the surface and avoid the interference effect from foreign species which may have similar oxidation potentials, such as ascorbic acid, acetaminophen, uric acid, and dopamine. To confirm the condition of the surface, SEM images were collected of the electrode surface before and after Nafion coating (Figure 7.13). The image after the Nafion coating layer was applied reveals a murky state (Figure 7.13c, d), while the surface before the Nafion coating shows a clear image (Figure 7.13a,

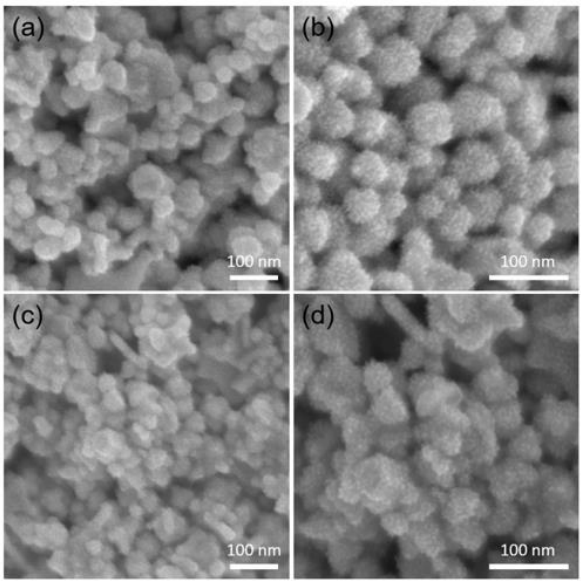

Figure 7.13. Surface of Au@Pt/Au modified electrodes: (a),(b) before Nafion coating and (c),(d) after Nafion coating.

b). This indicates that the Nafion layer was successfully coated on the Au@Pt/Au electrode surface.

In another control experiment, chronoamperometry was performed to investigate the analytical performance of the proposed method. Amperograms were recorded in the 0.1 M PBS_{sal} (pH 7.4) solution, and the applied potential was positively shifted from + 0.10 V to + 0.35 V, due to the increase in chloride anion concentration, which was responsible for a shift in the reference electrode potential. Thus, the applied potential of + 0.35 V was used. As a result, each modified electrode maintained its sensitivity towards glucose in 0.1 M PBS_{sal} compared to 0.1 M PBS (pH 7.4) solution: AuNPs/SPCE (no response), PtNPs/AuNPs/SPCE (59%), Au@Pt/AuNPs/SPCE (67%), Au@Pt/Au/AuNPs/SPCE (73%), and Nafion/Au@Pt/Au/AuNPs/SPCE (87%), respectively. Therefore, further experiments used the Nafion/Au@Pt/Au modified electrode in the 0.1 M PBS_{sal} (pH 7.4) solution.

The experimental parameters for glucose analysis using the Nafion coated electrodes (Nafion/Au@Pt/Au/AuNPs/SPCE) were optimized in terms of the amount of drop-coated Au@Pt, the applied potential, the temperature, and the pH (Figure 7.14). The effect of the amount of drop-coated Au@Pt on the response, which is an important factor in determining the electrode surface thickness, was investigated from 1.0 to 10.0 µL (Figure 7.14a). The response current increased as the amount of drop-coated Au@Pt increased from 1.0 to 4.0 µL, and a steady response was obtained over 4.0 µL Au@Pt. Therefore, 4.0 µL Au@Pt was used for subsequent experiments. The current response for glucose oxidation on Nafion/Au@Pt/Au was studied according to the applied potential in the range from + 0.15 to + 0.45 V (Figure 7.14b). As the glucose oxidation potential increased from + 0.15 V, the response current increased, and then the maximum response was

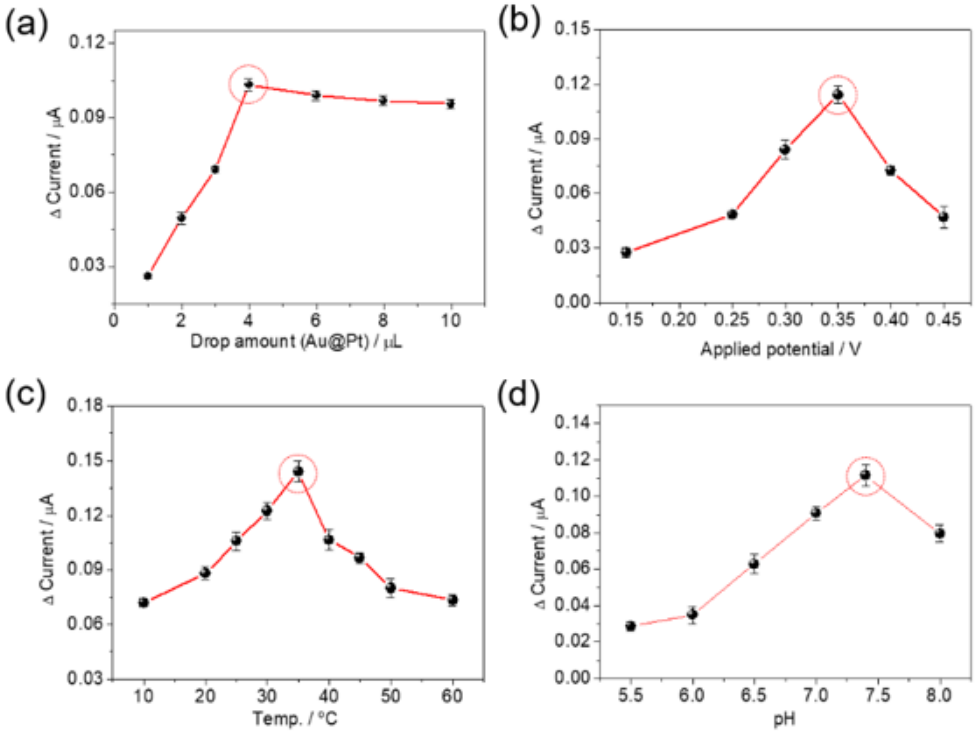

Figure 7.14. Optimization of the experimental parameters: the effects of (a) amount of drop-coated Au@Pt solution, (b) applied potential, (c) temperature, and (d) pH, using a 0.1 M PBS_{sal} (pH 7.4) solution containing 0.1 mM glucose to test the effects on the response peak current of Nafion/Au@Pt/Au/AuNPs/SPCE from the chronoamperometric experiments.

observed at + 0.35 V, which facilitated glucose oxidation. When the applied potential was increased to over + 0.40 V, however, the response current was somewhat affected by overlapping with the Au oxidation peak itself. Hence, + 0.35 V was chosen as the optimized applied potential. Temperature was controlled between 10 - 60 ℃, and the signal was found to be at a maximum at 35 ℃, and it then decreased over 40 ℃ due to the instability of the sensor surface over 40 ℃ (Figure 7.14c). Although the maximum response was observed at 35 ℃, we selected 25 ℃ as the measurement temperature, because real samples are usually measured at room temperature. The effect of pH on the current response was investigated between pH 5.5 and 8.0 (Figure 7.14d), where the response gradually increased as the pH increased from 5.5 to 7.4. The maximum response was obtained at pH 7.4, which is the physiological pH of blood. Hence, 4.0 μL electrode

material, + 0.35 V, 25 ℃, and pH 7.4 were chosen as the optimized measurement conditions. All optimizing experiments were conducted in a 0.1 M PBS_{sal} (pH 7.4) solution containing 0.1 mM glucose.

Under the optimized experimental conditions, the amperometric response to the glucose concentration was recorded using the Nafion/Au@Pt/Au modified electrode in the 0.1 M PBS_{sal} (pH 7.4) solution. The glucose oxidation current increased (applied potential at + 0.35 V) as the concentration of glucose (from 0.5 µM to 10.0 mM) increased (Figure 7.15a). Two dynamic ranges of the calibration plot were observed from 0.5.-10.0 µM and from 0.01 to 10.0 mM, with respective correlation coefficients of 0.99. The linear regression equations are ΔI_p (µA) = 8.27816 (± 0.28788) + 0.01649 (± 0.00101) [C] (mM)

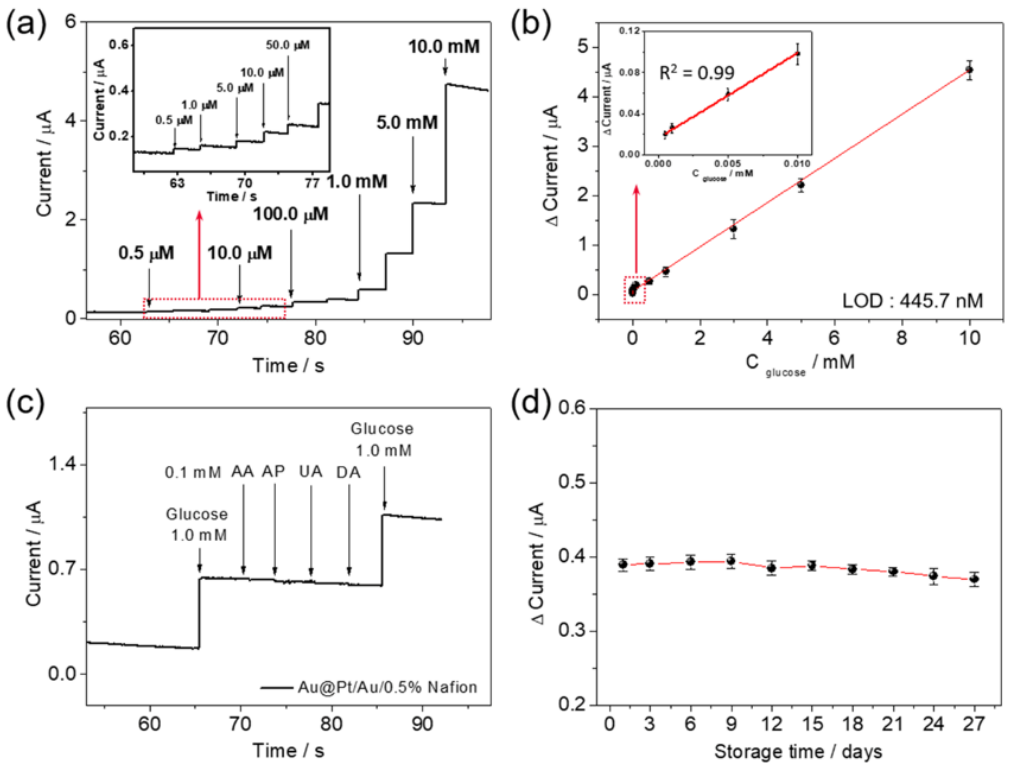

Figure 7.15. (a) Amperometric response to a wide range of glucose concentrations in 0.1 M PBS_{sal} (pH 7.4) and (b) corresponding calibration plot of Nafion/Au@Pt/Au modified electrode (applied potential: + 0.35 V (Ag/AgCl)). (c) Amperometric response for the interference effects of other bio-compounds on the sensor probe. (d) 27-day stability test, where the electrode was stored at room temperature in the dry state when not in use; test conditions: 0.1 M PBS_{sal} (pH 7.4) containing 1.0 mM glucose.

and ΔI_p (μA) = 0.43452 (± 0.01525) + 0.0986 (± 0.00746) [C] (mM), respectively. The detection limit (DL) of glucose was determined to be 445.7 (± 10.3) nM (Figure 7.15b) in PBS_{sal}. Table 7.1 shows a comparison of our performance with other AuPt samples in the previous literature [31,39,40]. Comparted to other electrode materials, our materials

Table 7.1. Comparison of the performances of our Au decorated Au@Pt NPs and of AuPt samples reported in other previous works.

Materials	Potential (V)	Sensitivity (μA mM^{-1} cm^{-2})	Methods	Detection Limit	Dynamic ranges	Solution	Real sample	Reference
Au decorated Au@Pt NPs	0.35	240 and 13.82	CA	0.45 μM	0.5 - 10.0 μM and 0.01 - 10.0 mM	PBS saline (pH 7.4)	Human whole blood	Our works
Pt–Au nanocorals	0.4	2.1	CA	28 μM	Up to 22 mM	PBS (pH 7)	N/A	[31]
PtAu/C	0.35	4.7	CA	2.0 μM	0 – 10 mM	PBS (pH 7.4)	N/A	[39]
platinum–gold alloy	0.3	10.71	CA	10 μM	Up to 24.44 mM	PBS saline (pH 7.4)	N/A	[40]

have more sensitivity and detection limit. In addition, our electrode confirmed that real sample experiment data obtained using human whole blood. Interestingly, our sensor probe displayed two dynamic ranges. This is most likely due to the different kinetic processes of glucose oxidation at low and high concentrations, with the former due to adsorptive modes, while the latter is by a diffusion controlled process [41,42]. Figure 7.15c shows the interference effects of ascorbic acid (AA, 0.1 mM), acetaminophen (AP, 0.1 mM), uric acid (UA 0.1 mM), and dopamine (DA, 0.1 mM) on the glucose (1.0 mM) oxidation current when using the Nafion/Au@Pt/Au modified electrode. The interference effect of each species was 2.4 % for AA, 2.6 % for AP, 2.7 % for UA, and 2.9 % for DA.

Figure 7.15d shows the long term stability result obtained for the response current according to the storage time in PBS_{sal} (pH 7.4) solution. After 27 days of measurement, it was maintained at 94.3% compared to the result for the first day, and therefore, it can be used for a long time.

Table 7.2. Comparison of the results obtained in the determination of the glucose concentration of whole blood samples by the proposed sensor and a comparable sensor system.

Samples	Glucose concentration (mM)			
	Proposed method	Mean (SD)	Commercial Sensor	Mean (SD)
No. 1	7.55	6.92 (±0.71)	7.27	6.70 (±0.56)
	7.05		6.66	
	6.16		6.16	
No. 2	5.83	5.81 (±0.39)	5.61	5.70 (±0.37)
	6.18		6.11	
	5.41		5.38	
No. 3	5.76	5.49 (±0.30)	5.99	5.43 (±0.58)
	5.16		4.88	
	5.55		5.16	
No. 4	6.33	5.93 (±0.62)	5.99	5.82 (±0.29)
	6.25		5.99	
	5.22		5.49	
No. 5	5.22	5.28 (±0.36)	5.33	5.40 (±0.18)
	5.07		5.27	
	5.56		5.60	

*Commercial Sensor (One Touch ultra™, Lifescan Inc.) SD: standard deviation.

To investigate the reliability of the sensor probe, it was applied to detect glucose levels in finger pricked human whole blood samples obtained from five volunteers (n = 5). At first, 10 μL of capillary blood was collected and diluted 5 times with 0.1 M PBS_{sal} (pH 7.4) solution and loaded onto the Nafion/Au@Pt/Au probe. In this case, the result yielded a regression equation of ΔI_p (μA) = 8.27816 (± 0.28788) + 0.01649 (± 0.00101) and ΔI_p (μA) = 0.43452 (± 0.01525) + 0.0986 (± 0.00746) [mM] with a correlation coefficient of

0.99 using five different sensors. Using the above regression equation, the glucose concentrations in the human blood sample were determined. The sensor performance was compared with a commercial glucose meter (One Touch ultra™, Lifescan Inc.). The proposed sensor showed good agreement with the commercial glucose meter as summarized in Table 7.2. The experimental results were evaluated using a paired t-test, where the calculated t_{cal} value of 0.32 was less than the critical t_{cri} value of 1.94 at a 95% confidence level. This demonstrates that the proposed sensor is reliable for the detection of glucose in finger-pricked human whole blood.

7.4 Conclusions

We synthesized core-shell Au@Pt NPs using the sonochemical method. Additional Au content was incorporated inside nano-channels of the dendritic porous Pt shell by using a potential step method. We successfully synthesized AuPt bimetallic shells in core-shell structured NPs and demonstrated the enhanced catalytic performance of these materials towards glucose oxidation. The Au@Pt/Au NPs with more abundant active sites showed improved sensitivity, stability, and selectivity towards glucose detection even at neutral pH due to the synergistic effects of combining Au and Pt. The sensor yielded a calibration plot in two dynamic ranges between 0.5 - 10.0 µM and 0.01 - 10.0 mM of glucose with respective correlation coefficients of 0.99. The detection limit (DL) of glucose in PBS_{sal} (pH 7.4) solution was determined to be 445.7 (±10.3) nM. Our electrode displays comparable results to a commercially available glucose meter. Thus, this study promises great potential for non-enzymatic glucose sensors.

7.5 References

[1] J. O'M. Bockris, S. U. M. Khan, Surface Electrochemistry, Plenum Press, New York, 1993.

[2] J. Jiang, Y. Li, J. Liu, X. Huang, C. Yuan, X. W. Lou, Adv. Mater., 2012, **24**, 5166-5180.

[3] M. H. Naveen, N. G. Gurudatt, Y.-B. Shim, Appl. Mater. Today, 2017, **9**, 419-433.

[4] A. Habrioux, E. Sibert, K. Servat, W. Vogel, K. B. Kokoh, N. Alonso-Vante, J. Phys. Chem. B, 2007, **111**, 10329-10333.

[5] J.-M. Moon, N. Thapliyal, K. K. Hussain, R. N. Goyal, Y.-B. Shim, Biosens. Bioelectron., 2018, **102**, 540-552.

[6] K.-J. Chen, W.-N. Su, C.-J. Pan, S.-Y. Cheng, J. Rick, S.-H. Wang, C.-C. Liu, C.-C. Chang, Y.-W. Yang, C.-H. Wang, B.-J. Hwang, J. Mater. Chem. B, 2013, **1**, 5925-5932.

[7] Y. Huang, Y.-E Miao, S. Ji, W. W. Tjiu, T. Liu, ACS Appl. Mater. Interfaces, 2014, **6**, 12449-12456.

[8] J. Jiang, X. Du, Nanoscale, 2014, **6**, 11303-11309.

[9] C.-L. Sun, H.-H. Lee, J.-M. Yang, C.-C. Wu, Biosens. Bioelectron, 2011, **26**, 3450-3455.

[10] Emerging Risk Factors Collaboration, Lancet, 2010, **375**, 2215-2222.

[11] M. Brownlee, Nature, 2001, **414,** 813-820.

[12] P. Zimmet, K. G. M. M. Alberti, J. Shaw, Nature, 2001, **414**, 782-787.

[13] D. R. Whiting, L. Guariguata, C. Weil, J. Shaw, Diabetes Res. Clin. Pract., 2011, **94**, 311-321.

[14] F. Luo, Y. Lin, L. Zheng, X. Lin, Y. Chi, ACS Appl. Mater. Interfaces, 2015, **7**, 11322-11329.

[15] C. Zhou, Y. Chen, X. You, Y. Dong, Y. Chi, ChemElectroChem, 2017, **4**, 1783-1789.

[16] D.-M. Kim, J.-M. Moon, W.-C. Lee, J.-H. Yoon, C. S. Choi, Y.-B. Shim, Biosens. Bioelectron., 2017, **91**, 276-283.

[17] L. C. Clark, C. Lyons, Ann. N. Y. Acad. Sci., 1962, **102**, 29-45.

[18] H. Zhu, L. Li, W. Zhou, Z. P. Shao, X. J. Chen, J. Mater. Chem. B., 2016, **4**, 7333-7349.

[19] K. Tian, M. Prestgard, A. Tiwari, Mater. Sci. Eng. C, 2014, **41**, 100-118.

[20] M. Baghayeri, A. Amiri, S. Farhadi, Sens. Actuators B-Chem., 2016, **225**, 354-362.

[21] Y. Tang, Q. Liu, Z. Jiang, X. Yang, M. Wei, M. Zhang, Sens. Actuators B-Chem., 2017, **251**, 1096-1103.

[22] S. Yang, G. Li, G. Wang, J. Zhao, X. Gao, L. Qu, Sens. Actuators B-Chem., 2015, **221**, 172-178.

[23] H Li, C.-Y. Guo, C.-L. Xu, Biosens. Bioelectron., 2015, **63**, 339-346.

[24] H.-L. Jiang, Q. Xu., J. Mater. Chem., 2011, **21**, 13705-13725.

[25] V. Malgras, Q. Ji, Y. Kamachi, T. Mori, F.-K. Shieh, K. C.-W. Wu, K. Ariga, Y. Yamauchi, Bull. Chem. Soc. Jpn., 2015, **88**, 1171-1200.

[26] H.-B. Noh, K.-S. Lee, P. Chandra, M.-S. Won, Y.-B. Shim, Electrochim. Acta, 2012, **61**, 36-43.

[27] S. J. Cho, H.-B. Noh, M.-S. Won, C.-H. Cho, K. B. Kim, Y.-B. Shim, Biosens. Bioelectron., 2018, **99**, 471-478.

[28] V. Malgras, H. Ataee-Esfahani, H. Wang, B. Jiang, C. Li, K. C.-W. Wu, J. H. Kim, Y. Yamauchi, Adv. Mater., 2016, **28**, 993-1010.

[29] Y. Xia, W. Huang, J. F. Zheng, Z. J. Niu and Z. L. Li, Biosens. Bioelectron., 2011, **26**, 3555–3561.

[30] R. A. Soomro, O. P. Akyuz, R. Ozturk, Z. H. Ibupoto, Sens. Actuators B-Chem., 2012, **233**, 230-236.

[31] Y. Liu, Y. Ding, Y. Zhang, Y. Lei, Sens. Actuators B-Chem., 2012, **171-172**, 954-961.

[32] D.-M. Kim, S. J. Cho, C.-H. Cho, K. B. Kim, M.-Y. Kim, Y.-B. Shim, Biosens. Bioelectron., 2016, **79**, 165-172.

[33] H. Ataee-Esfahani, L. Wang, Y. Nemoto, Y. Yamauchi, Chem. Mater., 2010, **22**, 6310-6318.

[34] K. Shim, J. Kim, Y.-U. Heo, B. Jiang, C. Li, M. Shahabuddin, K. C.-W. Wu, M. S. A. Hossain, Y. Yamauchi, J. H. Kim, Chem. Asian J., 2017, **12**, 21-26.

[35] K. Shim, J. Kim, M. Shahabuddin, Y. Yamauchi, M. S. A. Hossain, J. H. Kim, Sens. Actuator B-Chem., 2018, **225**, 2800-2808.

[36] T.-Y. Lee, Y.-B. Shim, Anal. Chem., 2001, **73**, 5629-5632.

[37] M. Pasta, F. L. Mantia, Y. Cui, Electrochim. Acta, 2010, **55**, 5561-5568.

[38] H. Jeong, J. Kim, Electrochim. Acta, 2012, **80**, 383-389.

[39] B. Singh, F. Laffir, T. McCormac, E. Dempsey, Sens. Actuators B-Chem., 2010, **150**, 80-92.

[40] J. Ryu, K. Kim, H.-S. Kim, H. T. Hahn, D. Lashmore, Biosens. Bioelectron., 2010, **26**, 602-607.

[41] H. Zhu, A. Sigdel, S. Zhang, D. Su, Z. Xi, Q. Li, S. Sun, Angew. Chem. Int. Ed., 2014, **53**, 12716-12720.

[42] M. H. Naveen, N. G. Gurudatt, H.-B. Noh, Y.-B. Shim, Adv. Funct. Mater., 2016, **26**, 1590-1601.

\

8. Tunable porosity in bimetallic core-shell structured Palladium-Platinum nanoparticles for electrocatalysts

8.1 Introduction

Noble metal nanoparticles (NPs) have attracted much attention in various fields, such as catalysts, sensors, biomedical applications, etc. [1-4]. In recent years, they have been reported many studies on bi- and tri-metallic nanoarchitectures [5-7]. In particular, palladium (Pd) based NPs are highly attractive as an alternative to platinum (Pt) NPs in terms of cost-effectiveness [8,9]. By combining them with carbons and other metals, the electrocatalytic properties of the Pd NPs can be further maximized [10,11].

Porous metals have been developed by various soft-template methods including lyotropic liquid crystals [12,13]. In general, structure-directing agents with low- and high-molecular-weight amphiphilic molecules can be used for preparing porous noble-metal-based NPs [14]. Amphiphilic surfactants and block copolymers (i.e., Brij 58® (Brij 58), Pluronic® F-127 (F-127), and Pluronic® P-123 (P-123)) have been mostly utilized to prepare nanoporous metals. [14,15]. Brij 58 has hydrophobic alkyl chain and hydrophilic PEO block, while F-127 is composed of poly(ethylene oxide)-poly(propylene oxide)-poly(ethylene oxide) (PEO-PPO-PEO), where the PEO is hydrophilic and the PPO consists of hydrophobic blocks. In the case of F-127, the hydrophilic units of the amphiphilic molecules accommodate the metal atoms during the formation of the porous structured NPs.

Porous noble metals have widely used as electrode for detecting glucose [16], phenolic compounds [17], and others biological important organics [18]. Recently,

bisphenol A (BPA, 2,2-bis(4-hydroxyphenyl) propane) is known to be produced by the polycarbonate plastics and epoxy resin, especially from various products (i.e. food containers and drink packaging) [8,17]. Unfortunately, the BPA can lead to some diseases including cancers and birth defects in our daily lives. Of the various methods for detecting BPA, electrochemical detection methods have been widely employed due to their advantages, such as, cost effective instruments, short analysis time, simplicity, and great sensitivity.

With research background, the main target of the present work is to discuss the effect of structure-directing agents on the resulting porous architectures. Here we prepared two types of porous Pd@Pt NPs with different surfactants (Brij 58 and F-127) using a sonochemical method under the same conditions except structure-directing agents. To confirm the electrochemically active surface area (ECSA), composition, and morphology, transmission electron microscopy (TEM), wide-angle powder X-ray diffraction (XRD), and cyclic voltammetry (CV) were carried out for the two different Pd@Pt NPs samples. Finally, the BPA sensor performances were compared and evaluated toward practical applications.

8.2 Experimental

With regard to reagents andmaterials, potassium tetrachloroplatinate (II) (K_2PtCl_4), sodium tetrachloropalladate(II) (Na_2PdCl_4), chloroplatinic acid hexahydrate (H_2PtCl_6), Pluronic® F-127, polyethylene glycol hexadecyl ether (Brij 58® , $HO(CH_2CH_2O)_{20}C_{16}H_{33}$), hydrochloric acid (HCl), bisphenol A (BPA, 2,2-bis(4-hydroxyphenyl) propane), and L-ascorbic acid (AA) were obtained from Sigma-Aldrich Co. USA. A 0.1 M phosphate

buffer solution (PBS) was prepared using 0.1 M disodium hydrogen phosphate and 0.1 M sodium dihydrogen phosphate (Sigma-Aldrich Co. USA).

For synthesis of porous bimetallic Pd@Pt NPs, 0.6 ml of Na_2PdCl_4 (20 mM), 1.2 ml of K_2PtCl_4 (20 mM), 1.8 ml of H_2PtCl_6 (20 mM), and 60 μl of HCl (6 M) were thoroughly mixed in two vials. Brij 58® (60 mg) and Pluronic® F-127 (60 mg) was then added into the reaction vials, respectively. Each surfactant was completely dissolved, and 3.0 ml AA solution (0.1M) was added. Then, the mixed vials were sonicated in a water bath for 4 h at 40 ℃. The final products were collected by centrifugation at 12,000 rpm for 10 min and were washed with ethanol and water.

In order to prepare Pd@Pt NPs electrode for bisphenol A detection, two kinds of porous Pd@Pt NPs (4 μg) with different Brij 58 and F-127 surfactants were dropped on screen-printed carbon electrodes, respectively [17]. As-prepared electrodes were activated by potential cycling from − 0.6 to + 1.2 V in 0.5M sulfuric acid (scan rate: 0.1 V s^{-1}, cycles: 30). Cyclic voltammograms (CVs) were recorded using a potentiostat/galvanostat (Ivium, Netherlands). The morphology and structure of the Pd@Pt NPs (prepared with Brij 58 and F-127) were observed using transmission electron microscopy (TEM; H-7600, HITACHI, Japan). Wide-angle powder XRD patterns were obtained by on a GBC MMA XRD (scan rate of 2° min^{-1}).

8.3 Results and discussion

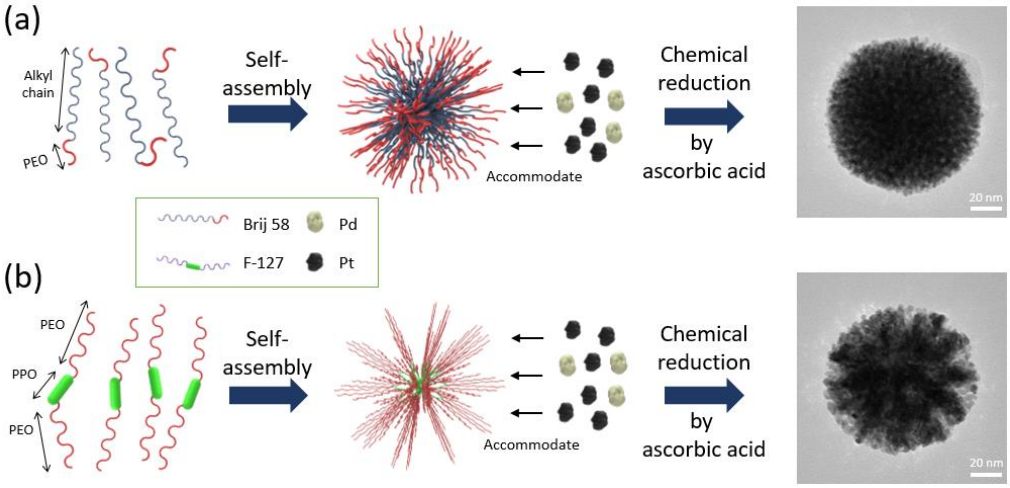

Figure 8.1. Illustrations of the synthesis of porous bimetallic Pd@Pt nanoparticles using two different surfactants: (a) Brij 58 (polyethylene glycol hexadecyl ether) and (b) F-127 (poly(ethyleneoxide)-poly(propylene oxide)-poly(ethylene oxide)).

To synthesise the two different kinds of porous Pd@Pt NPs, Na_2PdCl_4, H_2PtCl_6, and K_2PtCl_4, with either Brij 58 or F-127, were reacted using the sonochemical method in aqueous solution (Figure 8.1). The chemical formulae of the used surfactants are shown in Figure 8.2. The Pd (20 mM) and Pt (20mM) precursors and the HCl (6M) solution were thoroughly mixed, and then Brij 58 or F-127 was added into each reaction solution. In this step, the surfactants formed self-assembled micelles, where the hydrophilic heads were exposed to the aqueous face and the hydrophobic tails faced the micelle centre. Ascorbic acid (AA) was added as a reducing agent to each prepared solution under

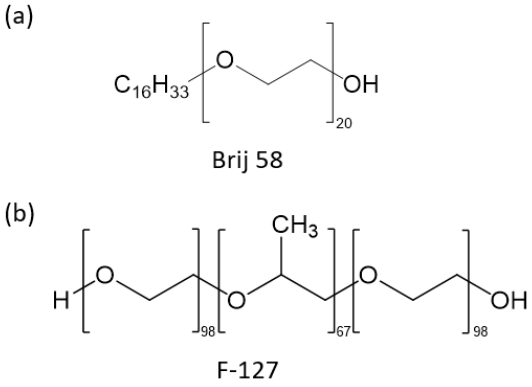

Figure 8.2. The actual chemical formulae of two different surfactants ((a) Brij 58 and (b) F-127).

ultrasonication [19]. The final products were collected, followed by washing with deionized (DI) water and ethanol to thoroughly remove the remaining reactants and surfactant. Before synthesising the final products, we initially examined the effect of the ratio of two different Pt precursors (K_2PtCl_4 and H_2PtCl_6), to which the final particle size can be attributed.

More interestingly, the standard reduction potential of Pd ($PdCl_4 \rightarrow Pd$: $E^0 = + 0.59$ V) is lower than for Pt ($[PtCl_6]^{2-} \rightarrow [PtCl_4]^{2-}$: $E^0 = + 0.68$ V and $[PtCl_4]^{2-} \rightarrow Pt$: $E^0 = + 0.76$ V). In the general process, it is thus expected that the reduction of Pt species is easier than for Pd species, resulting in the Pt@Pd structure. Our bimetallic NPs did not follow the general process, however. This is probably because our reduction kinetics related to the nuclei and the coordination effects are strongly governed by the specific experimental condition [20,21]. As results, we obtained the core-shell Pd@Pt structure in this study.

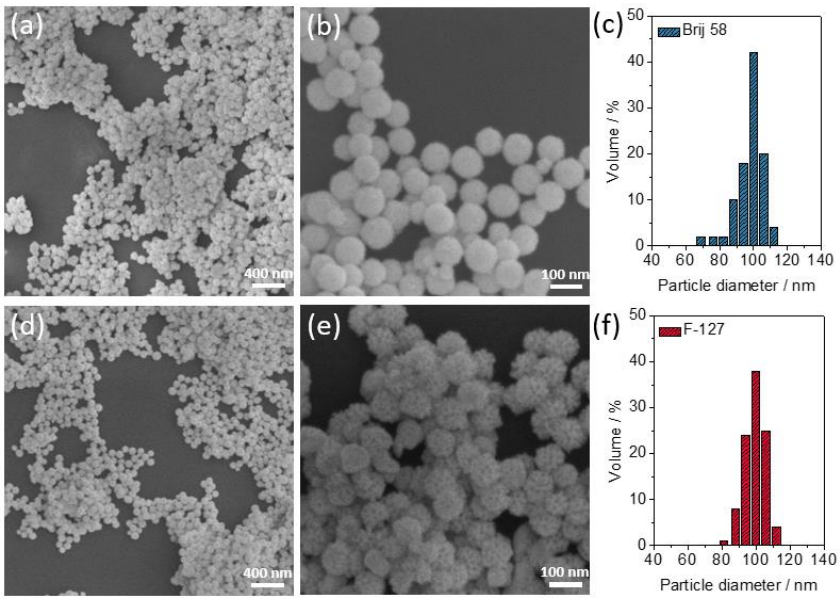

Figure 8.3. (a), (b) SEM images of Pd@Pt NPs prepared using Brij 58 (c), The particle size distributions of Pd@Pt NPs prepared using Brij 58 (d), (e) SEM images of Pd@Pt NPs prepared using F-127 (f) The particle size distributions of Pd@Pt NPs prepared using F-127.

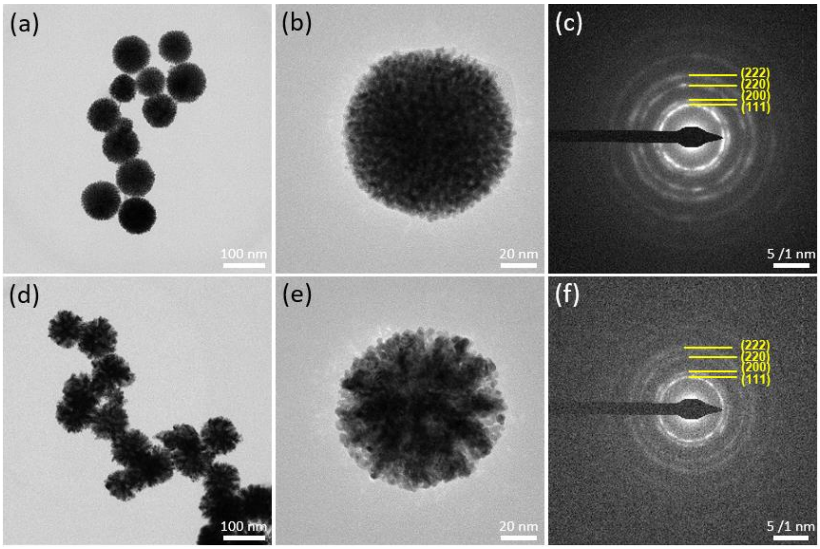

Figure 8.4. (a,b) TEM images of Pd@Pt NPs prepared using Brij 58 and (c) the corresponding SAED pattern. (d,e) TEM images of Pd@Pt NPs prepared using F-127 and (f) the corresponding SAED pattern.

The shape and size of Pd@Pt NPs were characterized by SEM and TEM, as can be seen in Figure 8.3 and 8.4. The average diameter of two different Pd@Pt NPs was estimated to be around 100 nm (Figure 8.3a, b and d, e). It is to be noted that Pd@Pt NPs prepared with F-127 have a relatively narrow size distribution. As can be seen in Figure 8.4, themorphology of Pd@Pt NPs prepared with Brij 58 is denser than for the Pd@Pt NPs prepared using F-127. The selected area diffraction (SAED) patterns of both Pd@Pt NPs samples indicate a face-centred cubic (fcc) crystal structure with concentric rings from the (111), (200), (220), and (222) planes, respectively (Figure 8.4c and f). Figure 8.5 shows the XRD patterns of the Pd@Pt NPs prepared using Brij 58 and F-127, where the patterns also indicate the *fcc* structure. To further confirm the structures of the Pd@Pt NPs samples, element mappings were performed on the two kinds of Pd@Pt NPs that were synthesised using the different surfactants, Brij 58 (Figure 8.6a) and F-127 (Figure 8.6b). As can be seen in Figure 8.6, the Pd (red) mainly exists in the core of the NPs, while the Pt (green) is located on the outer shell. This can be supported by the line scan element mapping (Figure 8.6). As a result, the Pd@Pt NPs prepared using Brij 58 are

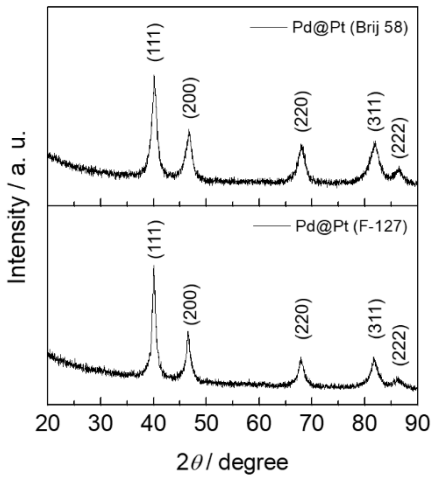

Figure 8.5. Wide-angle XRD patterns of porous bimetallic Pd@Pt NPs prepared using two different surfactants (Brij 58 and F-127).

much denser than Pd@Pt NPs prepared using F-127. We thus expected that the Pd@Pt NPs prepared with F-127 would have a relatively large ECSA compared to Pd@Pt NPs prepared using Brij 58. Hence, we evaluated the ECSA values of the Pd@Pt NPs prepared with the two different surfactants, respectively.

For this purpose, CVs were recorded for Pd@Pt NPs prepared using the different surfactants, Brij 58 (red dotted line) and F-127 (blue solid line), in 0.5 M sulfuric acid

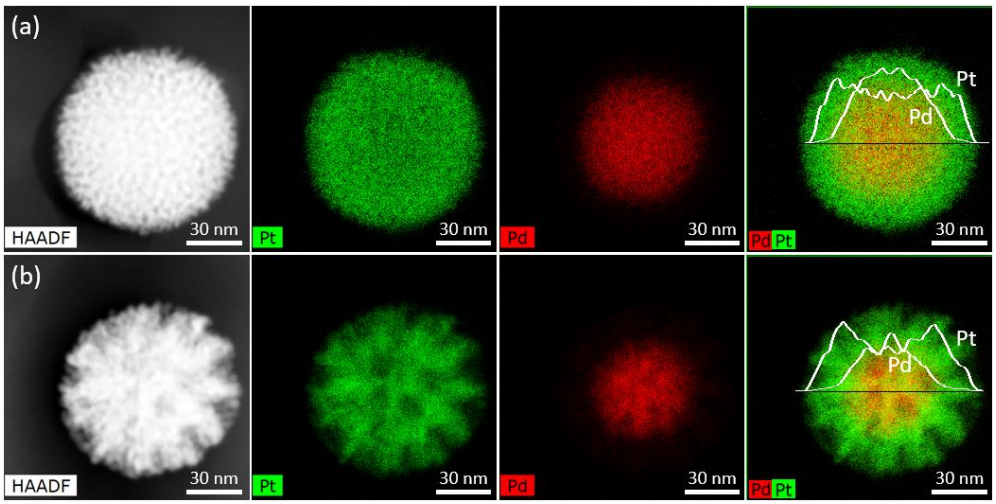

Figure 8.6. High-angle annular dark-field scanning transmission electron microscope (HAADF-STEM) images and elemental mappings, with line scans (insets on far right panels), of porous bimetallic Pd@Pt nanoparticles prepared using two different surfactants: (a) Brij 58 and (b) F-127.

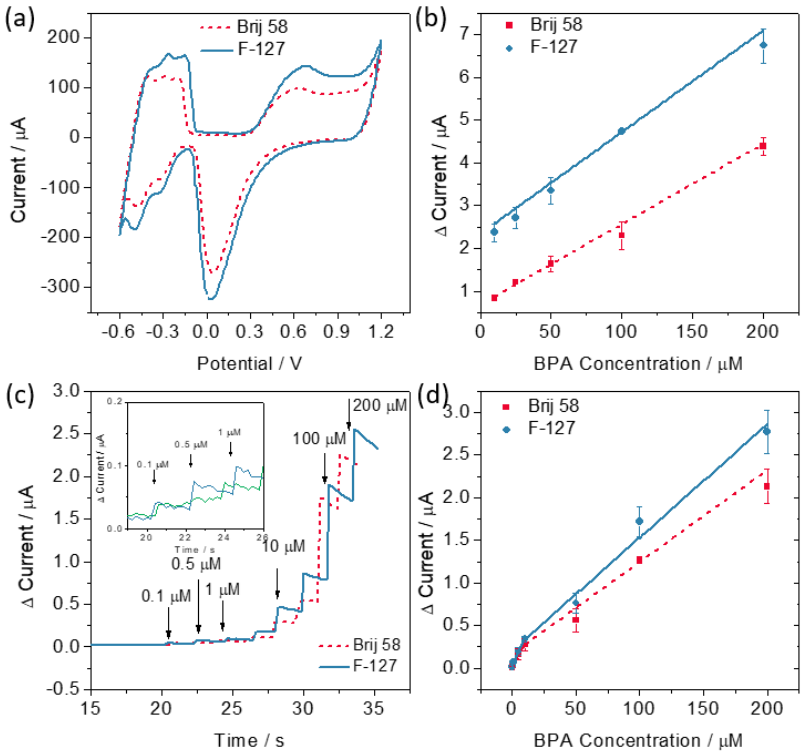

Figure 8.7. (a) Electrochemical active surface area(ECSA) of Pd@Pt NPs prepared using F-127 (blue solid) and Brij 58 (red dot) in 0.5M H_2SO_4 (scan rate: 0.05 V s^{-1}). (b) Bisphenol A detection calibration curves from CV (Pd@Pt NPs prepared using F-127 (blue solid) and Brij 58 (red dot)), (c)Amperometric response of Pd@PtNPs prepared using F-127 (blue solid) and Brij 58 (red dot) with different concentrations of BPA. (d) Calibration curves from the amperometric of Pd@Pt NPs prepared using F-127 (blue solid) and Brij 58 (red dot) responses over two dynamic ranges of BPA concentration.

(H_2SO_4) solution from − 0.6 V to + 1.2 V (scan rate: 0.05 V s^{-1}) (Figure 8.7a). The ECSAs from the H atom adsorption region are 11.26 and 16.37m^2 $g_{(Pt)}^{-1}$ for the NPs prepared using Brij 58 and F-127, respectively (Figure 8.8). The ECSA for the F-127 Pd@Pt NPs is larger than for those prepared using Brij 58. This indicates that electrochemically active sites could be tuned by surfactants having different chain lengths and structures.

To further confirm the effect of electrochemically active sites, as prepared electrodes using two different Pd@Pt NPs were tested for the electrochemical detection of bisphenol A, respectively. CVs were recorded in 10 to 200 μM by scanning the potential from 0.0 to 0.6 V (scan rate: 0.05 V s^{-1}) in 0.1 M BPA solution (Figure 8.9). The oxidation peak

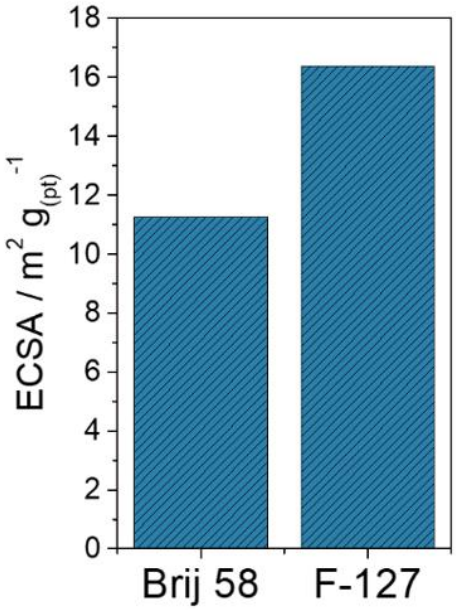

Figure 8.8. ECSA values for the Pd@Pt prepared using Brij 58 and F-127.

was confirmed at around + 0.32 V during the scanning. The calibration plots from CVs graphs indicated that the sensitivity of Pd@Pt prepared using F-127 is better than Pd@Pt prepared using Brij 58 (Figure 8.7b). To further check detection of low concentrations, we have employed Chronoamperometric (CA). The CA were determined continuously addition of various concentrations of bisphenol A in a 0.1 M PBS solution (Figure 8.7c). The applied potential of 0.45 V was applied to get amperograms. Two dynamic ranges from 0.1 to 5 µM and from 5 to 200 µM obtained for bisphenol A detection using Pd@Pt

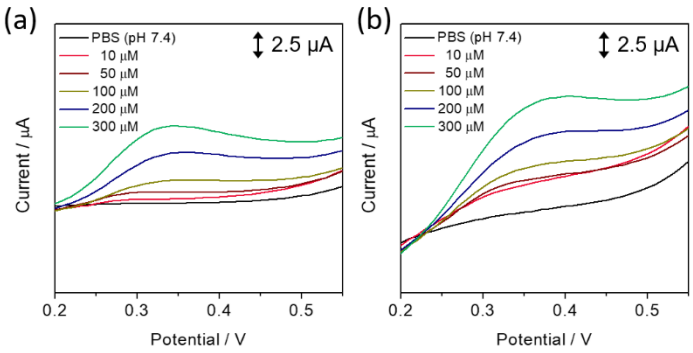

Figure 8.9. Detection of various concentrations (10, 50, 100, and 200 µM) of bisphenol A (a) using Pd@Pt prepared with Brij 58 electrodes, (b) Pd@Pt prepared with F-127 electrodes.

NPs prepared with F-127 and Brij 58 (Figure 8.7d). In addition, it was confirmed that the sensitivity of Pd@Pt NPs prepared using F-127 (0.1 to 5 μM: 0.03458 μA μM^{-1} and 5 to 200 μM: 0.01328 μA μM^{-1}) is better than using Brij 58 (0.1 to 5 μM: 0.02714 μA μM^{-1} and 5 to 200 μM: 0.01078 μA μM^{-1}) even in a low concentration. The detection limits of Bisphenol A were 44.85 (± 0.77) nM and 83.78 (± 0.43) nM, respectively. Further comparison studies of our BPA detection are shown in Table 8.1 with previous literatures [8, 22-25].

Table 8.1. Comparison studies of our BPA detection with previous literatures.

Materials	Linear range	Detection limit	Method	References
Pd@Pt NPs prepared using F-127	0.1 to 5 μM and 5 to 200 μM	0.045 μM	CA	This work
MWCNT/AuNP	0.01 to 0.7 μM	0.004 μM	DPV	[22]
Nanoporous gold	0.1 to 50 μM	0.012 μM	DPV	[23]
Na-doped WO_3 nanorods	0.08 to 22.5 μM	0.028 μM	DPV	[24]
AuNPs/SGNF	0.08 to 250 μM	0.035 μM	LSV	[25]
Pd/N-C	0.1 to 5 μM and 5 to 200 μM	0.029 μM	CA	[8]

* MWCNT (multi-walled carbon nanotube), SGNF (Stacked graphene nanofibers), and N-C (N-doped carbon nanofiber)

8.4 Conclusions

In summary, the surfactant as structure-directing agent plays a key role in the synthesis of porous metal structures. In F-127 with PEO-PPO-PEO blocks, the hydrophilic PEO accommodates the metal precursor. The role of the hydrophobic PPO

core is to create the large pores, resulting in more porosity and a looser structure. Using Pd@Pt NPs with F-127 induce more catalytic sites, results in better sensitivity for bisphenol A detection.

8.5 References

[1] C.-H. Cui, S.-H. Yu, Acc. Chem. Res., 2013, **46**, 1427-1437.

[2] R. R. Arvizo, S. Bhattacharyya, R. A. Kudgus, K. Giri, R. Bhattacharya, P. Mukherjee, Chem. Soc. Rev., 2012, **41**, 2943-2970.

[3] C. Zhu, D. Du, A. Eychmüller, Y. Lin, Chem. Rev., 2015, **115**, 8896-8943.

[4] J. Vieaud, J. Gao, J. Cane, M. Stchakovsky, A. E. Naciri, K. Ariga, R. Oda, E. Pouget, Y. Battie, J. Phys, Chem. C, 2018, **122**, 11973-11984.

[5] H. Shirai, M. T. Nguyen, D. Čempel, H. Tsukamoto, T. Tokunaga, Y.-C. Liao, T. Yonezawa, Bull. Chem. Soc. Jpn., 2017, **90**, 279-285.

[6] H. Ataee-Esfahani, L. Wang, Y. Nemoto, Y. Yamauchi, Chem. Mater., 2010, **22**, 6310-6318.

[7] L. Wang, Y. Yamauchi, Chem. Mater., 2011, **23**, 2457-2465.

[8] K. Shim, Z.-L. Wang, T. H. Mou, Y. Bando, A. A. Alshehri, J. Kim, M. S. A. Hossain, Y. Yamauchi, J. H. Kim, ChemPlusChem, 2018, **83**, 401-406.

[9] H. Zhang, M. Jin, Y. Xiong, B. Lim, Y. Xia, Acc. Chem. Res., 2013, **46**, 1783-1794.

[10] A. Zaleska-Medynska, M. Marchelek, M. Diak, E. Grabowska, Adv. Colloid Interface Sci., 2016, **229**, 80-107.

[11] G. S. Attard, J. M. Corker, C. G. Göltner, S. Henke, R. H. Templer, Angew. Chem. Int. Ed., 1997, **36**, 1315-1317.

[12] G. S. Attard, P. N. Bartlett, N. R. Coleman, J. M. Elliott, J. R. Owen, J. H. Wang, Science, 1997, **278**, 838-840.

[13] V. Malgras, H. Ataee-Esfahani, H. Wang, B. Jiang, C. Li, K. C.-W. Wu, J.H. Kim, Y. Yamauchi, Adv. Mater., 2016, **28**, 993-1010.

[14] B. Jiang, C. Li, V. Malgras, M. Imura, S. Tominaka, Y. Yamauchi, Chem. Sci., 2016, **7**, 1575-1581.

[15] B. Jiang, C. Li, M. Imura, J. Tang, Y. Yamauchi, Adv. Sci., 2015, **2**, 1500112.

[16] A. S. Nugraha, C. Li, J. Bo, M. Iqbal, S. M. Alshehri, T. Ahamad, V. Malgras, Y. Yamauchi, T. Asahi, ChemElectroChem, 2017, **4**, 2571-2576.

[17] K. Shim, J. Kim, M. Shahabuddin, Y. Yamauchi, M. S. A. Hossain, J. H. Kim, Sensors Actuators B Chem., 2018, **255**, 2800-2808.

[18] L.-X. Chen, J.-N. Zheng, A.-J.Wang, L.-J.Wu, J.-R. Chen, J.-J. Feng, Analyst, 2015, **140**, 3183-3192.

[19] K. Shim, J. Kim, Y.-U. Heo, B. Jiang, C. Li, M. Shahabuddin, K. C.-W. Wu, M.S.A. Hossain, Y. Yamauchi, J. H. Kim, Chem. Asian. J., 2017, **12**, 21-26.

[20] L. Wang, Y. Yamauchi, J. Am. Chem. Soc., 2013, **135**, 16762-16765.

[21] L. Wang, Y. Nemoto, Y. Yamauchi, J. Am. Chem. Soc., 2011, **133**, 9674-9677.

[22] N. B. Messaoud, M. E. Ghica, C. Dridi, M. B. Ali, C. M.A. Brett, Sens. Actuators B: Chem., 2017, **235**, 513-522.

[23] X. Yan, C. Zhou, Y. Yan, Y. Zhu, Electroanalysis, 2015, **27**, 2718-2724.

[24] Y. Zhou, L. Yang, S. Li, Y. Dang, Sens. Actuators B: Chem., 2017, **245**, 238-246.

[25] X. Niu, W. Yang, G. Wang, J. Ren, H. Guo, J. Gao, Electrochim. Acta, 2013, **98**, 167-175.

9. Facile synthesis of palladium-nanoparticle-embedded N-doped carbon fibers for electrochemical sensing

9.1 Introduction

Noble metals have received much attention in many catalyst applications owing to their high catalytic activities [1]. Of these materials, platinum (Pt) is used in various applications because of its high activity, but it comes at a high cost. Many researchers have been studying various approaches to solving the cost problems by modifying materials to increase their surface area, the activity and selectivity of active sites, and their stability [2]. In particular, the shape- and size-controlled synthesis of noble-metal nanomaterials has received increasing attention because of their stimulation of catalytic reactions. Another modification method is to change the material. Palladium (Pd) can be used instead of platinum because its catalytic activity can be improved by modifying the material. In addition, Pd-based materials are about five times cheaper than Pt-based materials [3].

Palladium NPs are used widely in applications such as fuel cells, the oxidation of formic acid, and gas sensors [4]. The materials are modified by various methods, and the catalytic activity is highly dependent on the size and morphology of the Pd nanostructures [4,5]. These play a critical role in the performance over a wide range of applications. Pd NPs that are used for composites enhance unique catalytic properties. Therefore, metal/carbon hybrid catalysts such as Pt/C and Pd/C are of great interest in terms of both increasing catalytic activity as well as decreasing the cost [6]. There are diverse reports showing the enhanced electrocatalytic performances of metal/carbon hybrid materials, such as in sensors [7,8], fuel cells [9,10], and energy storage [11,12]. These catalysts are

synthesized by depositing metal nanoparticles (NPs) onto the outer surface, inner surface, or interface of the support. The shapes of the metal NPs or support materials influence their catalytic activity. In addition, a decrease in size of the metallic catalyst and an increased active area of the support materials improve their performance. As the catalyst active part of the support materials is increased, maintaining and/or improving performance, the amount of material used decreases. Metal/carbon hybrid materials such as metal/GO [13,14], metal/SWCNT [12,15], metal/MWCNT [16,17], and metal/CNFs [18,19] have already been developed.

These materials have been used for the detection of various species. Among them, the detection of bisphenol A (2,2-bis(4-hydroxyphenyl) propane) is highly important, because bisphenol A can lead to health problems such as breast cancer, prostate cancer, birth defects, infertility, precocious development in girls, diabetes, and obesity [20]. Bisphenol A is one of the raw materials used to produce plastics and resins, and can be used for food containers, drink packaging, and to coat metal products (e.g., food cans, bottle tops) [21,22]. Various methods have been used for the detection of bisphenol A such as separation analysis [23], fluorimetry [24], immunoassay [25], and electrochemical methods [26]. Of these, the electrochemical method has more advantages than other methods, such as short analysis time, simplicity, and great sensitivity. Because of this, electrochemical sensors using the direct oxidation reaction have been developed to detect bisphenol A, and this method requires electrochemically active electrode materials. The development of electrode materials is most important for good sensitivity. Herein, we have focused on reducing the amount of Pd and successfully synthesized Pd-nanoparticle-embedded N-doped carbon fibers (Pd/N-C) with a Pd content of 1.5 wt%. The Pd/N-C hybrid material contains a small amount of Pd compared with other

commercial Pd/C materials. Scanning electron microscopy (SEM), transmission electron microscopy (TEM), X-ray diffraction (XRD), and Raman spectroscopy were employed to characterize the Pd/N-C hybrid materials. Finally, we studied the application of the materials in the detection of bisphenol A.

9.2 Experimental

Chemicals and materials: Aniline ($C_6H_5NH_2$, JIS Special Grade) and nitric acid (HNO_3, JIS Special Grade) were purchased from Wako Pure Chemical Industries, Ltd. Carbon paper (CP) was provided by Toray (Japan). Sodium tetrachloropalladate(II) (Na_2PdCl_4, 98.0 %), monosodium phosphate (NaH_2PO_4), disodium phosphate (Na_2HPO_4), and bisphenol A were obtained from Sigma–Aldrich. Phosphate buffer solution (0.1 M, pH 7.4) was prepared by mixing solutions of 0.1 M NaH_2PO_4 and 0.1 M Na_2HPO_4.

Synthesis of Pd/N-C catalyst: PANI fibers were prepared through the galvanostatic method at a current density of 2 mA cm^{-2} for 2 h on a carbon paper (CP) electrode. Before use, the CP was treated at 500 ℃ in air for 1.5 h and washed with concentrated acid. The treated CP was used as the working electrode and the counter electrode, and a saturated calomel electrode (SCE) was used as the reference electrode. The electrolyte was prepared by dissolving HNO_3 (3.7 mL) in H_2O (44 mL), and then adding aniline (2.3 mL) to form a uniform solution. After electrochemical polymerization, PANI fibers were stripped from the CP and dispersed in water by ultrasonication. They were washed three times and freeze-dried for 24 h. The obtained polymer powder was then carbonized at 800 ℃ in a N_2 atmosphere for 3 hand converted into N-doped carbon. Next, the as-prepared carbon powder (40 mg) was dispersed in H_2O (40 mL) with ultrasonication for 2 h. Na_2PdCl_4 (1.67 mg) was dissolved in H_2O (40 mL). The Na_2PdCl_4 solution was then added dropwise to the carbon powder suspension. The sample was stirred for 2 h and

washed three times, then dispersed in ethanol (20 mL) and transferred into a flask linked with a hydrogen balloon. The sample was reduced by hydrogen at 30°C for 12h with stirring. Then, the Pd/N-C catalyst was obtained after washing and vacuum drying.

Instruments: A screen-printed carbon electrode (SPCE) was used for the detection of bisphenol A. The area of the exposed working electrode that contained the carbon was 0.03141 cm^2. First, colloidal AuNPs in solution [34,35] were dropped onto the SPCE and dried. Secondly, the Pd/N-C hybrid (or commercial Pd/C) materials were dropped on the Au NP-modified SPCE and dried. The reference electrode was Ag/AgCl, and the counter electrode was pure carbon [36,37]. Amperograms and cyclic voltammograms (CVs) were recorded with a potentiostat/galvanostat (Ivium, Netherland). Microstructures were examined by TEM (JEOL ARM-200F, Japan) and SEM (JEOL JSM-7500). The surface area was calculated by the BET method using the obtained adsorption isotherm (BELSORP-mini II, Microtrac BEL Corp.). Wide-angle powder XRD patterns were measured with a GBC MMA XRD at a scanning rate of 2° min^{-1}. Raman spectroscopy was obtained with a JY HR800 instrument (HORIBA, Japan). XPS experiments were performed with a VG Scientific ESCALAB 2201XL instrument.

9.3 Results and discussions

The obtained Pd/N-C hybrid materials were obtained by electropolymerization and reduction methods (Figure 9.1a). The strategy for the synthesis of Pd/N-C hybrid materials can be summarized into four simple steps. First, the polyaniline (PANI) fibers were prepared by electrochemical polymerization in acid aniline solution. They were deposited on carbon paper and then stripped and dispersed in water. After washing three times, freeze-drying technology was used to remove the water to prevent the aggregation

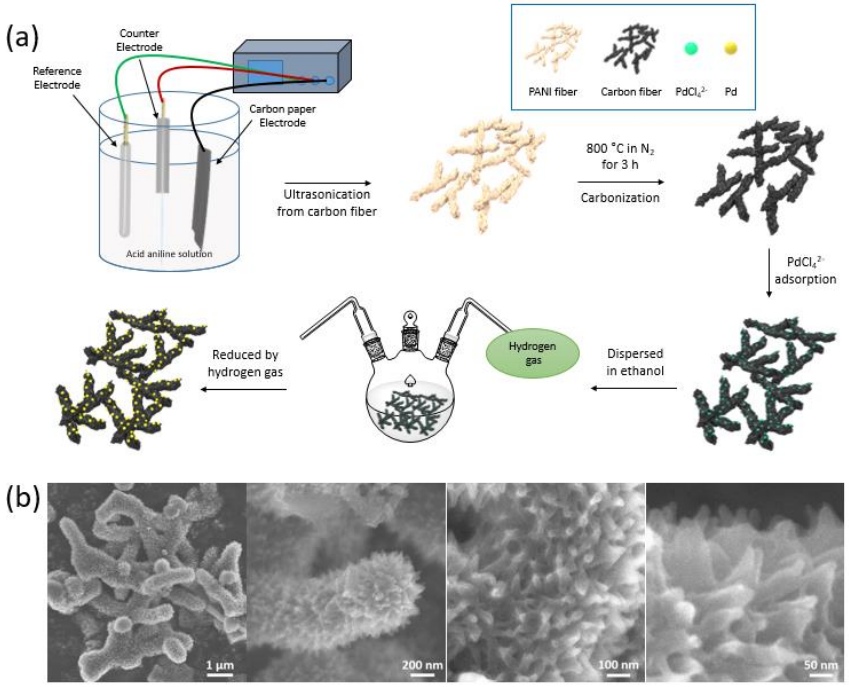

Figure 9.1. (a) Schematic illustration of the synthesis of Pd/N-C hybrid material and (b) SEM images of Pd/N-C hybrid material.

of the PANI fibers. By optimizing the type of acid, unique needle-branched nanostructures of PANI fibers were formed in HNO_3 electrolyte. Secondly, the polymer precursor was carbonized in nitrogen at 800°C for 3 h, and was thus converted into N-doped carbon fibers. Thirdly, the resulting carbon fibers were soaked in water by ultrasonic dispersion, and then the quantitative Na_2PdCl_4 solution was added dropwise

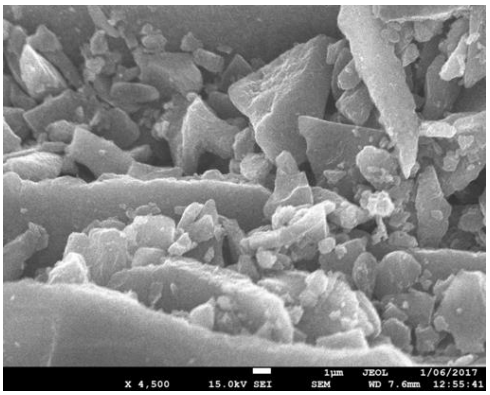

Figure 9.2. SEM image of Pd/C commercial material.

with stirring. Finally, the sample was dispersed in ethanol and reduced in a hydrogen atmosphere at 30℃ for 12 h.

The obtained Pd/N-C hybrid materials and commercial Pd/C particles were confirmed by SEM (Figure 9.1b and Figure 9.2). From these images, it can be confirmed that the Pd/N-C hybrid materials have a greater surface area than commercial Pd/C materials because of the specific shape of the Pd/N-C hybrid materials. Similarly to the shape

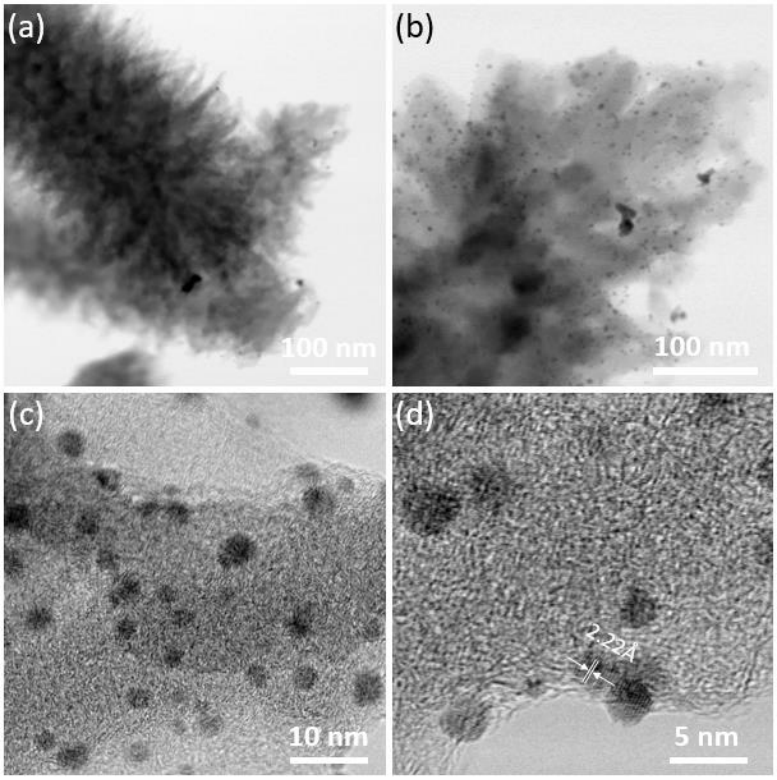

Figure 9.3. TEM images of Pd/N-C hybrid material: (a,b) low magnification, and (c,d) high magnification.

identified in the SEM images, the unique nanostructural surface on the fibers was also confirmed by TEM observation (Figure 9.3a,b). For confirmation of the presence of Pd NPs on the Pd/N-C fibers, the particles were observed directly by TEM. It was revealed that small Pd NPs are formed on the carbon fibers and are evenly distributed (Figure 9.3c,d). The Pd content was determined to be 1.5 wt% by ICP measurement. Note that the Pd content can be tuned from low to high values by varying the reactant ratios. However, for a high content (>1.5 wt%), the size of the Pd NPs will increase. By optimizing the electrochemical performances, it was found that the content of 1.5 wt% is the best value with the highest utilization efficiency of Pd. As seen in the Raman spectra

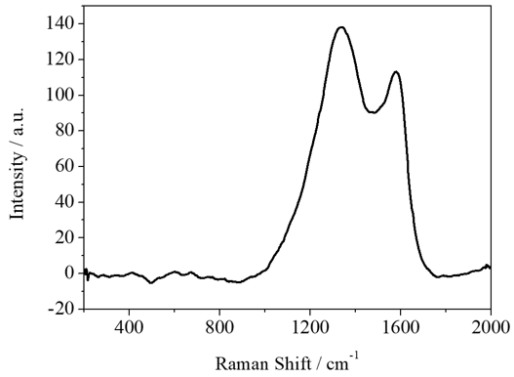

Figure 9.4. Raman spectrum of Pd/N-C hybrid material.

of the Pd/N-C hybrid material, two peaks at 1598 cm^{-1} (G band) and 1320 cm^{-1} (D band) are observed (Figure 9.4), indicating a well-developed carbon matrix. The surface area was calculated to be 31 m^2 g^{-1} by using the BET method and the obtained adsorption isotherm (Figure 9.5).

A high-resolution TEM image shows that the size of the Pd NPs is around 3nm. The NPs show lattice fringes of around 0.22 nm, which is consistent with the d-spacing for the Pd (111) plane (Figure 9.3d). These images provided direct evidence that the Pd NPs

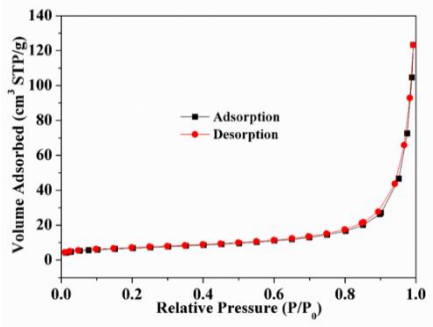

Figure 9.5. N_2 adsorption-desorption isotherm of Pd/N-C hybrid material.

are well-crystalline and faceted. The wide-angle XRD peaks record the crystalline phase of the Pd/N-C hybrid material (Figure 9.6). The peaks of the Pd NPs can be assigned to (111), (200), (220), and (311) diffraction peaks of the face-centered cubic (fcc) crystal structure. For further understanding of the Pd/N-C hybrid materials, HAADF-STEM images and elemental mapping were used, as shown in Figure 9.7. The Pd/N-C hybrid materials are composed of C, N, and Pd elements (Figure 9.7b–d). It is indicated that N and Pd are present on the carbon nanofiber. As seen in Figure 9.7d, Pd NPs are clearly and uniformly distributed on the N-doped carbon fiber. In general, porous carbons are well known as catalytic support materials. Among them, N-doped porous carbon is one of the most interesting materials owing to properties such as enhanced catalytic activity, higher conductivity, and much higher resistance for coarsening [26]. Therefore, it is

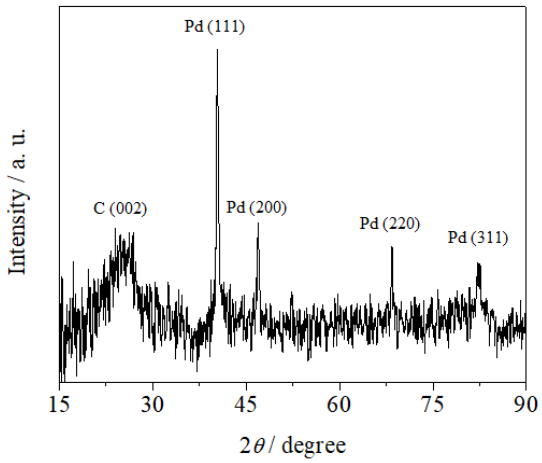

Figure 9.6. Wide-angle XRD pattern of Pd/N-C hybrid material.

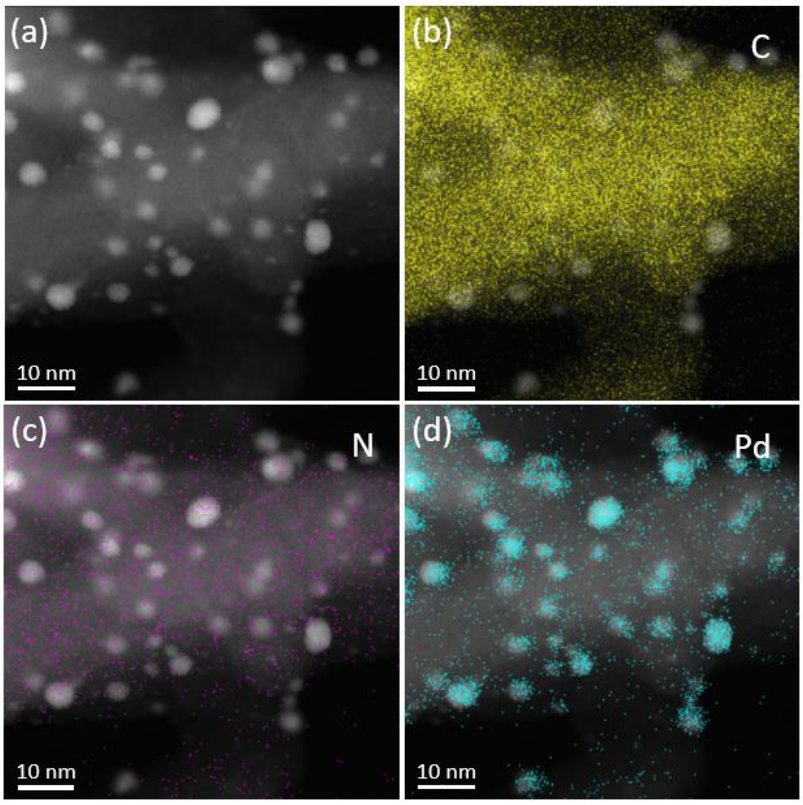

Figure 9.7. (a) HAADF-STEM image, and (b–d) elemental mapping images of Pd/N-C hybrid material.

expected that Pd/N-C hybrid materials will improve the sensitivity for the detection of bisphenol A despite the lower amount of Pd.

Detailed XPS spectra were obtained to understand the chemical element states of the Pd/N-C hybrid material further. The survey results clearly show the presence of Pd3d, C1s, N1s, and O1s from the materials (Figure 9.8a). The contents of N, Pd, and C are 5.3, 1.2, and 93.5 wt%, respectively. Although several N-doped carbons by different approaches have been reported [27-31], the N-doping is very effective for improving the electrical conductivity. Figure 9.8b–d reveals the high-resolution C1s, N1s, and Pd3d spectra of the Pd/N-C material. As seen in Figure 9.8b, the high-resolution C1s spectrum displays C-C, C-N, C-O, and C=O peaks, located at 284.8, 285.5, 286.5, and 288.8 eV, respectively. The deconvoluted N1s peak of the Pd/N-C material reveals pyridinic N, pyrrolic N, and oxidized N located at 398.20, 400.40, and 402.90 eV, respectively (Figure

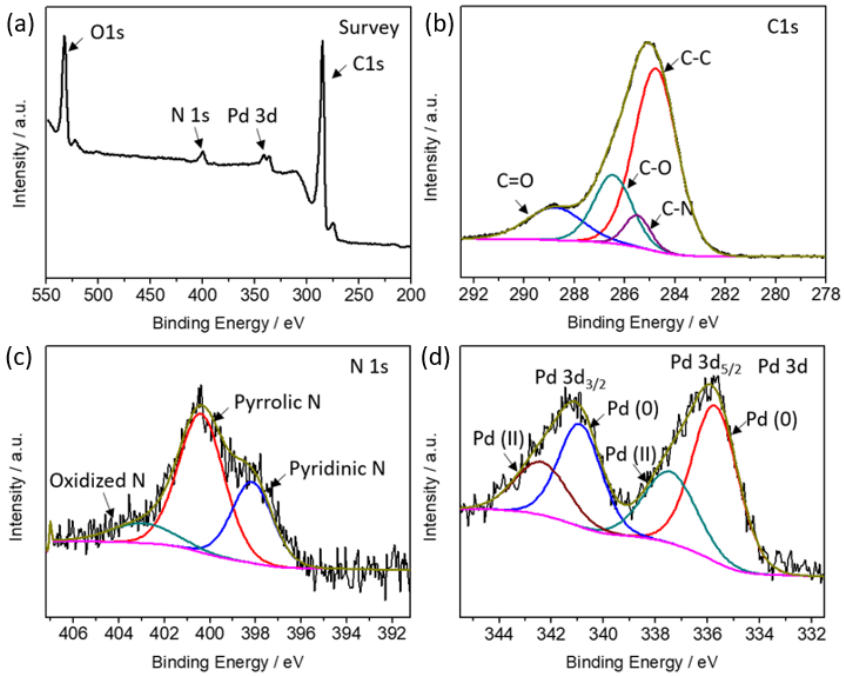

Figure 9.8. XPS spectra of Pd/N-C hybrid material ((a) survey, (b) C 1s, (c) N 1s, and (d) Pd 3d, respectively).

9.8c). The high-resolution Pd3d spectrum shows peaks appearing at 335.60 and 340.80 eV (Pd^0), and at 337.30 and 342.30 eV (Pd^{2+}) (Figure 9.8d), indicating that the surface of the Pd NPs is slightly oxidized.

The as-prepared electrode using the Pd/N-C hybrid material was tested for the electrochemical detection of bisphenol A. To realize the best performance, we checked the effect of the loading amount of the sample on the electrode. The Pd/N-C hybrid material suspension (3 μL, 1 μg μL^{-1}) was dropped on the electrode from one to four times. Then, cyclic voltammograms (CVs) were recorded using the electrodes modified with different amounts of the Pd/N-C hybrid materials (3-12 μL). The results revealed that 9 μL (three drops) was optimal (Figure 9.9). The Pd/N-C hybrid material and commercial Pd/C electrodes were activated by scanning the potential from 0.0 to 0.6 V at a scan rate of 0.1 V s^{-1} for ten cycles using cyclic voltammetry (CV). After activation, CVs were recorded in 5 to 100 mm by scanning the potential from 0.0 to 0.6 V at a scan rate of 0.05

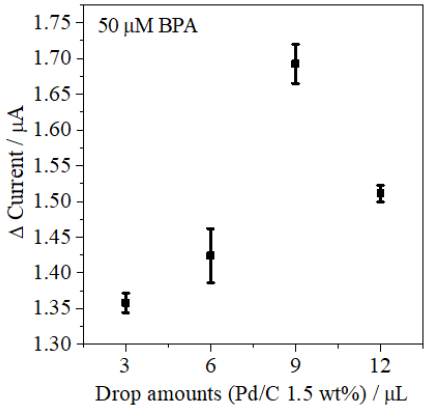

Figure 9.9. Optimization of experimental parameter.

V s^{-1}. During the scanning, the oxidation peak appeared clearly at around + 0.23 V versus Ag/AgCl (vs. sat. KCl) (Figure 9.10a). The calibration plots showed that the sensitivity of the Pd/N-C hybrid material electrode (slope = 0.0237 μA $μM^{-1}$) (black) is similar to that of the commercial Pd/C modified electrode (slope = 0.0228 μA $μM^{-1}$) (red) (Figure 9.10b). Thus, we achieved a very high efficiency using the Pd/N-C hybrid material with only 1.5 wt% Pd. This efficiency is almost the same as that of the commercial material with a much higher Pd content (10 wt% Pd), which clearly has economic implications.

Chronoamperometric (CA) response curves were obtained with successive addition of different concentrations of bisphenol A in a 0.1m PBS solution (Figure 9.10c). To attain the maximum response current for BPA using the Pd/N-C hybrid modified electrode, the experimental conditions were optimized in terms of the starting and final applied potentials (Figure 9.11). In this case, the optimized starting and final applied potentials were determined to be + 0.05 and + 0.45 V, respectively. Two dynamic ranges of the calibration plot for bisphenol A detection were determined from 0.1 to 10 μM and from 10 to 200 μM, with correlation coefficients of 0.9836 and 0.9987, respectively (Figure 9.10d). The two different linear ranges are caused by the different kinetics at different

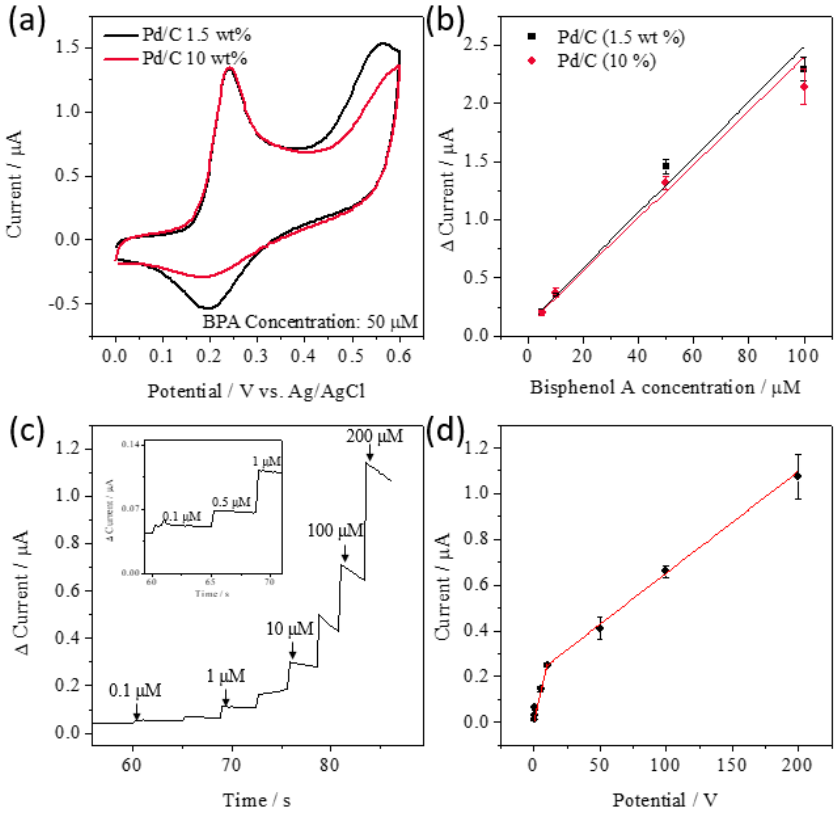

Figure 9.10. (a,b) CVs for characterization of Pd/N-C hybrid material (with 1.5 wt% Pd) and Pd/C commercial material (10 wt% Pd): (a) Detection of bisphenol A (50 µm) using Pd/N-C hybrid material and Pd/C commercial material electrodes. (b) Bisphenol A detection (5, 10, 50, and 100 µm) calibration curves. c) Amperometric response of Pd/N-C hybrid material/AuNPs/SPCE with different concentrations of BPA. d) Calibration curves from the amperometric responses over two ranges of BPA concentration.

concentrations of bisphenol A. The oxidation kinetics in the low-concentration range were dominated by the adsorption process, whereas the kinetics in the high-concentration range depended on the BPA diffusion and activation by the catalyst [32]. The detection limit (DL) of bisphenolA was determined to be 29.44 (± 0.77) nM. The threshold values

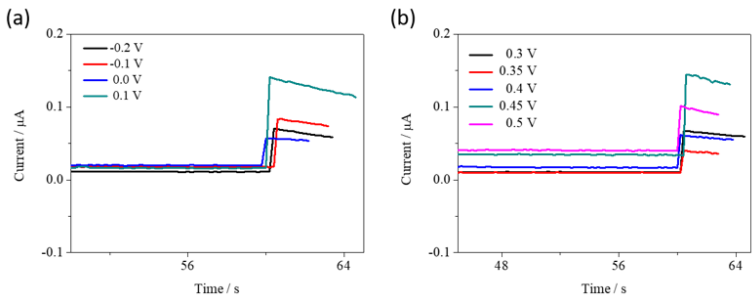

Figure 9.11. Optimization of experimental parameters of Pd/N-C hybrid material. (a) Starting applied potential and (b) final applied potential.

of bisphenol A in water samples are already regulated by the European Chemicals Bureau. The values have defined predicted no-effect concentrations (PNEC) for fresh (1.5 mg L^{-1}) and marine (0.15 mg L^{-1}) waters [33]. Further comparison of our performance with previous literature is shown in Table 9.1 [38-42]. Therefore, Pd/N-C hybrid materials can be used for electrode materials for the detection of bisphenol A.

Table 9.1. Comparison of our performance with previous literature.

Active materials	Linear range	Method	Detection limit	References
Pd/N-C	0.1-10, 10-200 μM	Amperometry	29.4 nM	This work
Pd@TiO_2-SiC	0.01-5, 5-200 μM	DPV	4.3 nM	38
3Au-1Pd alloy NPs/GN	0.01-5 μM	DPV	4 nM	39
AuPdNPs/GNs	0.05-10 μM	DPV	8 nM	40
Ag-Pd/GO	0.02-45 μM	DPV	5 nM	41
NCNF	0.1-6 μM	DPV	50 nM	42

*GN: graphene, GO: graphene oxide, NCNF: nitrogen-doped carbon nanofiber, DPV: differential pulse voltammetry.

9.4 Conclusions

We have successfully synthesized a Pd/N-C hybrid material by using electropolymerization and reduction methods. Small-sized Pd NPs were loaded successfully on the carbon fibers. The Pd NPs were distributed evenly on the carbon fibers without any aggregation. The Pd content was determined to be 1.5 wt% from ICP measurements. Interestingly, our Pd/N-C hybrid material shows very high efficiency, even though the loading amount of Pd is only 1.5 wt%, which is much lower than that of commercially available materials. The Pd/N-C hybrid modified electrode showed two dynamic ranges from 0.1 to 10 μM and from 10 to 200 μM, with a detection limit of 29.44 (± 0.77) nM.

9.5 References

[1] C. Zhu, D. Du, A. Eychmeller, Y. Lin, Chem. Rev., 2015, **115**, 8896-8943.

[2] Y. Xia, X. Yang, Acc. Chem. Res., 2017, **50**, 450-454.

[3] M. Shao, J. Power Sources, 2011, **196**, 2433-2444.

[4] A. Chen, C. Ostrom, Chem. Rev., 2015, **115**, 11999-12044.

[5] H. Zhang, M. Jin, Y. Xiong, B. Lim, Y. Xia, Acc. Chem. Res., 2013, **46**, 1783-1794.

[6] D. S. Su, S. Perathoner, G. Centi, Chem. Rev., 2013, **113**, 5782-5816.

[7] V. R. Khalap, T. Sheps, A. A. Kane, P. G. Collins, Nano Lett., 2010, **10**, 896-901.

[8] C. Rajkumar, P. Veerakumar, S.-M. Chen, B. Thirumalraj, S.-B. Liu, Nanoscale, 2017, **9**, 6486-6496.

[9] S. Chakraborty, C. R. Raj, Carbon, 2010, **48**, 3242-3249.

[10] H.-W. Liang, W. Wei, Z.-S. Wu, X. Feng, K. Mellen, J. Am. Chem. Soc., 2013, **135**, 16002-16005.

[11] Y. Lei, J. Lu, X. Luo, T. Wu, P. Du, X. Zhang, Y. Ren, J. Wen, D. J. Miller, J. T. Miller, Y.-K. Sun, J. W. Elam, K. Amine, Nano Lett., 2013, **13**, 4182-4189.

[12] V. R. Chitturi, M. Ara, W. Fawaz, K. Y. S. Ng, L. M. R. Arava, ACS Catal., 2016, **6**, 7088-7097.

[13] M. Iqbal, C. Li, B. Jiang, M. S. A. Hossain, M. T. Islam, J. Henzie, Y. Yamauchi, J. Mater. Chem. A, 2017, **5**, 21249-21256.

[14] J.-J. Lv, S.-S. Li, A.-J. Wang, L.-P. Mei, J.-J. Feng, J.-R. Chen, Z. Chen, J. Power Sources, 2014, **269**, 104-110.

[15] J.-H. Lee, W.-S. Kang, C.-K. Najeeb, B.-S. Choi, S.-W. Choi, H.-J. Lee, S.-S. Lee, J.-H. Kim, Sens. Actuators B, 2013, **188**, 169-175.

[16] V. Bambagioni, C. Bianchini, A. Marchionni, J. Filippi, F. Vizza, J. Teddy, P. Serp, M. Zhiani, J. Power Sources, 2009, **190**, 241-251.

[17] H. An, H. Cui, D. Zhou, D. Tao, B. Li, J. Zhai, Q. Li, Electrochim. Acta, 2013, **92**, 176-182.

[18] G. Hu, F. Nitze, H. R. Brazegar, T. Sharifi, A. Mikolajczuk, C.-W. Tai, A. Borodzinski, T. W,gberg, J. Power Sources, 2012, **209**, 236-242.

[19] J. Huang, D. Wang, H. Hou, T. You, Adv. Funct. Mater., 2008, **18**, 441-448.

[20] K. V. Ragavan, N. K. Rastogi, M. S. Thakur, TrAC Trends Anal. Chem., 2013, 52, 248-260.

[21] H. Yin, L. Cui, S. Ai, H. Fan, L. Zhu, Electrochim. Acta, 2010, **55**, 603-610.

[22] H. Yoshida, H. Harada, H. Nohta, M. Yamaguchi, Anal. Chim. Acta, 2003, **488**, 211-221.

[23] Z. Kuklenyik, J. Ekong, C. D. Cutchins, L. L. Needham, A. M. Calafat, Anal. Chem., 2003, **75**, 6820-6825.

[24] X. Wang, H. Zeng, L. Zhao, J.-M. Lin, Anal. Chim. Acta, 2006, **556**, 313-318.

[25] M. A. Rahman, M. J. A. Shiddiky, J.-S. Park, Y.-B. Shim, Biosens. Bioelectron., 2007, **22**, 2464-2470.

[26] X.-H. Li, M. Antonietti, Chem. Soc. Rev., 2013, **42**, 6593-6604.

[27] Y. Chen, X. Li, K. Park, L. Zhou, H. Huang, Y.-W. Mai, J. B. Goodenough, Angew. Chem. Int. Ed., **2016**, 55, 15831–15834; Angew. Chem., 2016, **128**, 16063-16066.

[28] Y. Chen, J. Dong, L. Qiu, X. Li, Q. Li, H. Wang, S. Liang, H. Yao, H. Huang, H. Gao, J.-K. Kim, F. Ding, L. Zhou, Chem, 2017, **2**, 299-310.

[29] Y. Chen, X. Li, K. Park, W. Lu, C. Wang, W. Xue, F. Yang, J. Zhou, L. Suo, T. Lin, H. Huang, Chem, 2017, **3**, 152-163.

[30] R. R. Salunkhe, C. Young, J. Tang, T. Takei, Y. Ide, N. Kobayashi, Y. Yamauchi, Chem. Commun., 2016, **52**, 4764-4767.

[31] R. R. Salunkhe, J. Tang, N. Kobayashi, J. Kim, Y. Ide, S. Tominaka, J. H. Kim, Y. Yamauchi, Chem. Sci., 2016, **7**, 5704-5713.

[32] M. H. Naveen, N. G. Gurudatt, H.-B. Noh, Y.-B. Shim, Adv. Funct. Mater., 2016, **26**, 1590-1601.

[33] G. M. Klecˇka, C. A. Staples, K. E. Clark, N. van der Hoeven, D. E. Thomas, S. G. Hentges, Environ. Sci. Technol., 2009, **43**, 6145-6150.

[34] K. Shim, J. Kim, M. Shahabuddin, Y. Yamauchi, M. S. A. Hossain, J. H. Kim, Sens. Actuators B, 2018, **255**, 2800-2808.

[35] M. J. A. Shiddiky, Y.-B. Shim, Anal. Chem., 2007, **79**, 3724-3733.

[36] N.-H. Kwon, K.-S. Lee, M.-S. Won, Y.-B. Shim, Analyst, 2007, **132**, 906-912.

[37] D.-M. Kim, S. J. Cho, C.-H. Cho, K. B. Kim, M.-Y. Kim, Y.-B. Shim, Biosens. Bioelectron., 2016, **79**, 165-172.

[38] L. Yang, H. Zhao, S. Fan, B. Li, C.-P. Li, Anal. Chim. Acta, 2014, **852**, 28-36.

[39] C. Huang, Y. Wu, J. Chen, Z. Han, J. Wang, H. Pan, M. Du, Electroanalysis, 2012, **24**, 1416-1423.

[40] B. Su, H. Shao, N. Li, X. Chen, Z. Cai, X. Chen, Talanta, 2017, **166**, 126-132.

[41] J. Li, H. Feng, J. Li, J. Jiang, Y. Feng, L. He, D. Qian, Electrochim. Acta, 2015, **176**, 827-835.

[42] J. Sun, Y. Liu, S. Lv, Z. Huang, L. Cui, T. Wu, Electroanalysis, 2016, **28**, 439-444.

10. Conclusions and outlook

10.1 Conclusions

In this thesis, I have discussed noble metal materials that can be used for sensors based on the direct oxidation method. These materials have some drawbacks, however. The purpose of this work is to minimize these shortcomings and to improve their electrochemical performance *via* changing morphologies and compositions. The general conclusion of this research work is divided into parts for each subproject carried out. This doctoral work describes the synthesis of porous noble metal based nanoparticles (NPs) including Pt, Au@Pt, Au@Pt/Au, Pd@Pt, and Pd/N-doped carbon nanofibers. These electrode materials were doped onto screen printed carbon electrodes and applied for bisphenol A (BPA) and glucose detection. In addition, these electrocatalysts were analyzed to determine their physical and electrochemical properties and sensing performance using various methods.

To synthesize dendritic platinum nanoparticles (DPNs), the soft-template method was employed. Interestingly, these materials had a narrow particle size distribution (around 23 nm) and large surface area (47 m^2 g^{-1}). HRTEM and XRD studies confirmed that the obtained DPNs displayed *fcc* crystal structures. In addition, the HAADF-STEM study indicated that the DPNs had {111} facets. To apply them to bio-applications, it was necessary to confirm the cytotoxicity of the DPNs using HEK-293 cells. DPNs are very likely to be helpful in a variety of fields, especially in bio-applications and in the electrocatalyst field because of their large surface area and pore volume.

DPNs have been used as electrode materials for bisphenol A (BPA) detection due to their large surface area and high catalytic activity. In this study, BPA detection was

satisfactory using DPNs, but it was applied to BPA detection using PEI-PC layers coated on DPN electrodes, which can prevent interference from other species and enhance sensitivity. These electrodes displayed two dynamic ranges from 0.01 to 1 μM and from 1.0 to 300 μM with the detection limit of 6.63 nM. In addition, the electrodes were evaluated for the BPA determination in tap water using a recovery study toward practical applications.

Porous Au@Pt NPs were synthesized via the sonochemical method in different molar ratios (Au:Pt: 3:7, 5:5, and 7:3). A TEM study indicated that Au was located in the core, while Pt was located on the core (as a shell). In addition, as the amount of Pt increased, the thickness of Pt shell also increased. Due to this reason, it was confirmed that the different sizes of the NPs depending on the amount of Pt. The electrochemically active surface area (ECSA) for the sample with the 3:7 molar ratios (Au:Pt) of Au area was higher than for the others (5:5 and 7:3). With these electrode materials, glucose oxidation was detected. The Au@Pt (7:3) modified electrodes revealed the best performance compared to other modified electrodes. The Au@Pt (7:3) modified electrodes featured two dynamic ranges for glucose oxidation, ranging from 0.5 – 50 μM and 0.05 – 10.0 mM with the detection limit of 319.8 nM in 0.1 M phosphate buffer solution (PBS).

Au@Pt NPs were prepared by the sonochemical method. After the synthesis of Au@Pt NPs, Au was incorporated in nanochannels on the Pt shell by electrodeposition. The electrochemically active surface area (ECSA) of the Au@Pt/Au modified electrode was increased compared to before the Au deposition. To avoid interference effects, Nafion layers were coated onto the Au@Pt/Au modified electrode. Using this electrode, glucose oxidation was determined in 0.1 M phosphate buffered saline (PBS_{sal}) (pH 7.4). The electrode indicated two dynamic ranges for glucose (0.5 – 10.0 μM and 0.01 – 10.0

mM) with the detection limit of 445.7 nM. To investigate the reliability of the sensor probe, it was applied to detect glucose levels in blood samples. It was demonstrated that the proposed electrode is reliable for the detection of glucose in human whole blood.

Porous bimetallic Pd@Pt NPs prepared using two different surfactants (Brij® 58 (Brij 58) and Pluronic® F-127 (F-127)) were synthesized to compare the effects of different surfactants. TEM and ECSA studies were employed to compare Pd@Pt NPs prepared using F-127 and Brij 58. A TEM study indicated that Brij 58 resulted in denser material than F-127. In addition, the ECSA of Pd@Pt NPs with F-127 was higher than with Brij 58. It was revealed that F-127 had more electrochemically active sites, which resulted in better sensitivity towards bisphenol A detection.

A Pd/N-doped carbon nanofiber (Pd/N-C) hybrid have synthesized via electropolymerization and reduction methods for BPA detection. 1.5 wt % of small sized Pd NPs was loaded on the carbon nanofibers. The Pd/N-C hybrid showed similar sensitivity compared to commercial Pd/C, even though the Pd loading amount was only 1.5 wt % for bisphenol A detection. The hybrid electrode demonstrated two dynamic ranges from 0.1 to 10 μM and 10 to 200 μM with the detection limit of 29.44 nM.

10.2 Outlooks

In this thesis, the synthesis of electrode materials and their application as glucose and bisphenol A sensors have been described. The structure and physical properties of the synthesized materials were thoroughly studied, and the sensor performance was studied. Although noble metal-based materials have been studied extensively, there are still problems (i.e. sensitivity and cost problem) to be solved. In order to solve these problems,

it is necessary to change the morphology and composition of the materials or develop alternative materials from noble metals. The research strategy presented in this paper may be of considerable interest to other researchers.

Appendix A: List of Publications

1. **Kyubin Shim**, Jeonghun Kim, Yoon-Uk Heo, Bo Jiang, Cuiling Li, Mohammed Shahabuddin, Kevin C.-W. Wu, Md. Shahriar A. Hossain, Yusuke Yamauchi, Jung Ho Kim, "Synthesis and cytotoxicity of dendritic platinum nanoparticles with HEK-293 cells", *Chemistry – An Asian Journal*, 2017, **12**, 21-26.
2. **Kyubin Shim**, Jeonghun Kim, Mohammed Shahabuddin, Yusuke Yamauchi, Md. Shahriar A. Hossain, Jung Ho Kim, "Efficient wide range electrochemical bisphenol-A sensor by self-supported dendritic platinum nanoparticles on screen-printed carbon electrode", *Sensors and Actuators B: Chemical*, 2018, **255**, 2800-2808.
3. **Kyubin Shim**, Zhong-Li Wang, Tasnima Haque Mou, Yoshio Bando, Abdulmohsen Ali Alshehri, Jeonghun Kim, Md. Shahriar A. Hossain, Yusuke Yamauchi, Jung Ho Kim, "Facile synthesis of palladium-nanoparticle-embedded N-doped carbon fibers for electrochemical sensing", *ChemPlusChem*, 2018, **83**, 401-406.
4. **Kyubin Shim**, Jianjian Lin, Min-Sik Park, Mohammed Shahabuddin, Yusuke Yamauchi, Md Shahriar A. Hossain, Jung Ho Kim, "Tunable porosity in bimetallic core-shell structured palladium-platinum nanoparticles for electrocatalysts", *Scripta Materialia*, 2019, **158**, 38-41.
5. **Kyubin Shim**, Won-Chul Lee, Min-Sik Park, Mohammed Shahabuddin, Yusuke Yamauchi, Md Shahriar A. Hossain, Yoon-Bo Shim, Jung Ho Kim, "Au decorated core-shell structured Au@Pt for the glucose oxidation reaction", *Sensors and Actuators B: Chemical*, 2019, **278**, 88-96.
6. **Kyubin Shim**, Won-Chul Lee, Yoon-Uk Heo, Mohammed Shahabuddin, Min-

Sik Park, Md Shahriar A. Hossain, Jung Ho Kim, "Rationally designed bimetallic Au@Pt nanoparticles for glucose oxidation", *Scientific Reports*, accepted.

7. Lin Jing, **Kyubin Shim**, Cui Ying Toe, Tim Fang, Chuan Zhao, Rose Amal, Ke-Ning Sun, Jung Ho Kim, and Yun Hau Ng, "Electrospun Polyacrylonitrile−Ionic Liquid Nanofibers for Superior PM2.5 Capture Capacity", *ACS Applied Materials & Interfaces*, 2016, **8**, 7030-7036.
8. Bishnu Prasad Bastakoti, Yunqi Li, Sudhina Guragain, Saad M. Alshehri, Muhammad J.A. Shiddiky, Zongwen Liu, **Kyubin Shim**, Jung Ho Kim, Md Shahriar A Hossain, Victor Malgras, Yusuke Yamauchi, "Formation of mesopores inside platinum nanospheres by using double hydrophilic block copolymers", *Materials Letters*, 2016, **182**, 190-193.
9. Dabum Kim, Jeonghun Kim, Youngsang Ko, **Kyubin Shim**, Jung Ho Kim, Jungmok You, "A facile approach for constructing conductive polymer patterns for application in electrochromic devices and flexible microelectrodes", *ACS Applied Materials & Interfaces*, 2016, **8**, 33175-33182.
10. Malenahalli Halappa Naveen, **Kyubin Shim**, Md. Shahriar A. Hossain, Jung Ho Kim, Yoon-Bo Shim, "Template free preparation of heteroatoms doped carbon spheres with trace Fe for efficient oxygen reduction reaction and supercapacitor" *Advanced Energy Materials*, 2017, **7**, 1602002.
11. Sang A Han, Jaewoo Lee, **Kyubin Shim**, Jianjian Lin, Mohammed Shahabuddin, Jong-Won Lee, Sang-Woo Kim, Min-Sik Park, Jung Ho Kim, "Strategically Designed zeolitic imidazolate frameworks for controlling the degree of graphitization", *Bulletin of the Chemical Society of Japan.*, 2018, **91**, 1474-1480.

Appendix B: Conferences

1. Kyubin Shim and Jung Ho Kim, *"Au@Pt/Au nanoparticles derived advanced glucose sensor"*, 17th International Conference on Electroanalysis (ESEAC 2018), June 3-7, 2018, Rodos, Greece.